TÉCNICO LISBOA

UNIVERSIDADE DE LISBOA
INSTITUTO SUPERIOR TÉCNICO

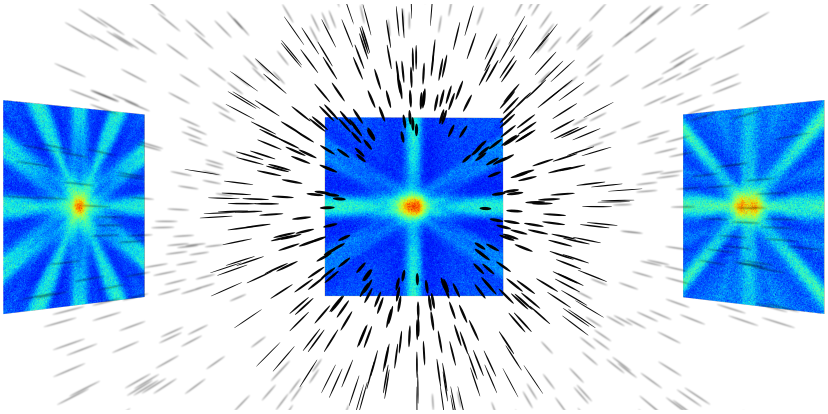

Emission Channeling Lattice Location Studies in Semiconductors using Highly Pixellated Timepix Detectors

Eric David Bosne

Supervisor: Doctor Ulrich Wahl

Co-Supervisor: Doctor João Guilherme Martins Correia

Thesis approved in public session to obtain the PhD Degree in Technological Physics Engineering

Jury final classification: Pass with Distinction

2020

TÉCNICO LISBOA

UNIVERSIDADE DE LISBOA
INSTITUTO SUPERIOR TÉCNICO

Emission Channeling Lattice Location Studies in Semiconductors using Highly Pixellated Timepix Detectors

Eric David Bosne

Supervisor: Doctor Ulrich Wahl

Co-Supervisor: Doctor João Guilherme Martins Correia

Thesis approved in public session to obtain the PhD Degree in Technological Physics Engineering

Jury final classification: Pass with Distinction

Jury

Chairperson:
Doctor Pedro Miguel Félix Brogueira, Instituto Superior Técnico, Universidade de Lisboa
Members of the Committee:
Doctor João Pedro Esteves de Araújo, Faculdade de Ciências da Universidade do Porto
Doctor Ulrich Wahl, Instituto Superior Técnico, Universidade de Lisboa
Doctor Katharina Lorenz, Instituto Superior Técnico, Universidade de Lisboa
Doctor Lino Miguel da Costa Pereira, Faculty of Science, KU Leuven, Bélgica

Funding Institutions:
Portuguese Foundation for Science and Technology (SFRH/BD/95865/2013, CERN/FIS-PAR/0005/2017, UID/Multi/04349/2019)
FWO Vlaanderen and the KU Leuven
European Commission through the Horizon 2020 program (grant number 654002 ENSAR2)

2020

Acknowledgments

This work would have never been possible without all the people that supported me during this process. To them, I wish to express my deepest gratitude.

I would like to start by recognizing the invaluable assistance of my supervisor, Dr. Ulrich Wahl, whose deep scientific insight helped me learn when to redirect my focus and keep bounds in my research while at the same time staying open to new ideas. I also want to thank him for always trying to make the most of each interaction and never falling short of passing valuable knowledge.

I would like to pay my special regards to my co-supervisor, Dr. Guilherme Correia, for the immense coordination efforts needed to keep our geographically disperse collaboration working together in good spirits and for the guidance given on the hands-on work in transportation, storage and maintenance of all the laboratory equipment. What's more, I would like to thank him for the constant availability to help and to all the support given during my time at CERN.

I would like to thank the *Fundação para a Ciência e Tecnologia* (FCT), for the financial support of my PhD (SFRH/BD/95865/2013). I also acknowledge the ISOLDE collaboration for providing radioactive beams and laboratory facilities. Not forgetting, the Medipix collaboration for providing the detectors used in this thesis and for always being present and ready to help through this thesis.

I am indebted to the Medipix collaboration members and would like to thank, Dr. Lucas Tlustos, Dr. Michael Campbell and Dr. Xavier Llopart for all the help given while at CERN. From the collaboration I would also like to thank Dr. John Idarraga for coding MAFalda, and my friend Oliver Keller for the interesting discussions in the latest detector and readout technologies.

I also want to thank my CERN colleagues, Angelo Costa, Abel Fenta and Tania Mendonça, for the friendship and for making the work at ISOLDE so much more interesting. I could not have done it without you.

I wish to thank my friend and colleague at the IST PhD program lectures, Tahereh Niknejad, for the collaborative work done in the class projects which made learning much easier.

To my all my friends in Geneva and in Lisbon for helping me make so much of this time.

To my family for the unconditional support and understanding.

Abstract

The implantation of dopant impurities in semiconductor crystals and the understanding of their lattice site location behaviour in the manufacturing process is essential for the control of their electrical, magnetic and optical properties. The development and improvement of the detection systems used in lattice location experimental techniques with charged particles, specifically Rutherford Backscattering Spectrometry with Channeling (RBS/C) and Emission Channeling (EC), has been seen as a fundamental step in the enhancement of the quantitative capacities of these techniques. In this thesis, a highly pixelated timepix-quad detector developed by the Medipix collaboration based at CERN was studied with the aim of testing its performances, envisaging a replacement detector for the previously used pad detector. The new detector was mounted in a custom-built vacuum chamber and annexed to the existing EC experimental setup. The timepix detector causes a large increase in details of measured channeling patterns due to its array of 512×512 pixels with $55 \times 55\,\mu m^2$ area each, much finer than the one of the pad detector composed of 22×22 pixels with $1.3 \times 1.3\,mm^2$ area. The impact of the new detector on the lattice location results was studied regarding the reduction of the statistical uncertainties and the dispersion of results between axes measured, together with the practical aspects of its use. This purpose required the development of a new fitting software, PyFDD, that can use a chi-square or a maximum likelihood parameter optimization and has proven essential for fitting patterns with a low number of counts per pixel, and for accurately calculating the resulting uncertainties. Additionally, the background of beta and gamma radiation was also investigated as a source of uncertainty. The new analysis software allowed the comparison of the new timepix with the pad detector in the measurement of the isotopes ^{43}K, ^{24}Na, and ^{27}Mg implanted into gallium nitride, GaN. These tests have shown that the results from both detectors agree in the obtained relative lattice site fraction. However, some differences were observed in the absolute fractions which are mostly thought to be caused by the lack of accuracy of the gamma

background on EC measurements.

Keywords

Emission channeling; Position sensitive detectors; Timepix; Experimental modeling; Parameter estimation;

Resumo

A implantação de impurezas dopantes em cristais semicondutores é um passo essencial no fabrico de dispositivos, em particular para o controlo das suas propriedades elétricas, óticas e magnéticas. A magnitude e qualidade destas alterações depende, no entanto, das posições na rede cristalina que são ocupadas por estes átomos, uma vez finalizado o processo de fabrico. São, por isso, necessárias técnicas experimentais de localização de impurezas capazes de estudar a diversidade de materiais cristalinos e impurezas existentes em novos dispositivos propostos pelas comunidades internacionais científicas e tecnológicas.

O desenvolvimento e a melhoria dos sistemas de deteção de partículas utilizados pelas técnicas de localização de impurezas em redes cristalinas à base de canalização de partículas carregadas, em especifico *Rutherford Backscattering Spectrometry with channeling* (RBS/C) e *Emission Channeling* (EC), tem sido visto como uma etapa fundamental no aperfeiçoamento das capacidades quantitativas destas técnicas. Em particular, apesar das vantagens, os detetores bidimensionais sensíveis à posição têm sido pouco utilizados com a técnica de RBS/C. Tal facto é devido às dificuldades associadas ao tratamento de dados, à necessidade de realização de pesadas simulações computacionais e ao difícil acesso a este tipo de detetores com vida operacional limitada, uma vez que se usam iões como partícula que transporta a informação. Diferentemente, detetores bidimensionais são frequentemente usados em experiências de EC, onde por serem maioritariamente expostos a radiação beta conseguem ter uma longa vida operacional, sendo também a técnica onde o desenvolvimento de novos detetores rápidos e altamente pixelizados tem sido mais aproveitado e relevante.

Um detetor *timepix-quad* desenvolvido pela colaboração *Medipix* estabelecida no CERN foi aqui estudado com o objetivo de investigar a possibilidade desta família de detetores ser utilizada em experiências de EC e o seu potencial para a melhoria dos resultados quantitativos. O detetor *timepix-quad* é um detetor pixelizado com uma rede de 512×512 píxeis de $55 \times 55\,\mu m^2$ sensíveis à energia. Esta rede de píxeis possui grande resolução em posição e consequente captura de informação muito superior aos detetores utilizados até ao momento tipo *pad*, formados por uma rede de 22×22 píxeis com $1{,}3 \times 1{,}3\,mm^2$.

O detetor *timepix* foi conectado à câmara de vácuo do aparato experimental onde se efetuam as experiências EC, utilizando para isso uma câmara adicional desenhada de forma a ser capaz de trans-

mitir os sinais de comunicação entre o detetor e o hardware de controlo *fitpix* através de um conector ar-vácuo personalizado. Embora o controlo e a leitura do detetor seja feita pelo software comercial *Pixet*, foi necessária a adaptação e desenvolvimento de software adicional para o tratamento de dados e análise dos espectros medidos. Nesta tese todos os passos seguidos neste desenvolvimento são explicados e são dadas orientações para desenvolvimentos futuros destas aplicações. Uma vez finalizado e testado o novo sistema de hardware e software de controlo e análise, este foi utilizado nas medidas de localização em rede cristalina dos isótopos ^{43}K, ^{24}Na e ^{27}Mg em nitreto de gálio, GaN.

O impacto do detetor relativamente à melhoria dos resultados foi estudado em termos da redução das incertezas estatísticas e da dispersão de resultados provenientes da medida de vários eixos cristalinos. Para este fim, foi necessário definir metodologicamente e implementar no software um processo de análise capaz de modelar detetores com diferentes densidades de píxeis e de fazer o ajuste a dados experimentais com um *bias* reduzido utilizando o método do qui-quadrado ou o método de *maximum likelihood*. A possibilidade de escolha entre estes dois tipos de ajuste revela-se fundamental devido às vantagens associadas a cada um dos métodos. Por um lado, o qui-quadrado permite uma apreciação da qualidade do ajuste realizado, no entanto nos casos em que o número de contagens por pixel é baixo este método tem erros associados, situação frequente em detetores com uma elevada densidade de píxeis como o timepix. Por outro lado, o método de *maximum likelihood* é indicado para qualquer número de contagens, mas não tem nenhum indicador para a qualidade de ajuste. Este novo processo foi implementado em python no programa de código aberto PyFDD. O novo software foi feito numa perspetiva de uso tanto em EC como em RBS/C e engloba várias ferramentas: umas, necessárias à preparação de padrões experimentais antes de proceder à sua análise; outras, capazes de simular a resposta de detetores face a uma condição experimental de canalização definida em padrões teóricos, a fim de proceder ao ajuste de padrões experimentais com uma biblioteca de simulações previamente realizadas.

Na procura de melhoria da qualidade dos resultados de EC é aqui apresentado um estudo do impacto da radiação de fundo no bias dos resultados. A radiação de fundo presente em experiências de EC é uma combinação de radiação gama proveniente dos decaimentos radioativos e de eletrões provenientes da amostra mas que no caminho até ao detetor sofreram alguma dispersão e perderam assim a informação de canalização. O estudo do impacto dos eletrões dispersos foi feito por via de simulações GEANT4 e foi visto que sendo o efeito uniforme no detetor nenhum *bias* na localização dos isótopos implantados é esperado. Por outro lado, o estudo do fundo de gamas foi feito com medidas experimentais onde é clara a existência de anisotropia capaz de criar pequenos desvios durante a análise dos resultados.

É ainda aqui mostrado o estudo do efeito da resolução angular, causada pelo tamanho dos píxeis dos detetores, na capacidade de determinar a localização de impurezas. Isto foi, em primeiro lugar,

abordado com um estudo baseado apenas em simulações e na determinação da quantidade de informação perdida em consequência da limitada resolução experimental, causada principalmente pela área de implantação de prova com um diâmetro mínimo de 1 mm. A informação existente nos padrões foi visualizada e estudada com recurso às transformadas de Fourier dos padrões simulados num espectro de intensidade de frequências espaciais. Este espectro de frequências foi então comparado com o limite de deteção calculado a partir da resolução angular do sistema experimental. Em segundo lugar, o problema foi abordado causando artificialmente a redução da resolução angular a uma medida real e verificando a estabilidade dos resultados face a este teste. Combinando estes dois resultados verificou-se que na maioria dos casos os resultados são essencialmente independentes das mudanças de resolução possíveis. Também se verificou que as medidas dos eixos $[0\,0\,0\,1]$ são as mais sensíveis à resolução angular e que isótopos com decaimentos beta de elevada energia como o ^{11}Be beneficiam de elevada resolução angular.

Das medidas de EC realizadas em GaN foram efetuadas conclusões tanto a nível da localização dos isótopos implantados como sobre a utilização dos detetores. Foi verificado que o potássio ocupa uma posição substitucional do gálio (SGa) e que esta é estável pelo menos até um recozimento a 800 °C. Também foi visto que adotando uma distribuição de posições em torno do SGa, representado na análise pelo termo de vibração da impureza u_1, existe um melhor ajuste do modelo utilizado com a medida experimental. No estudo do sódio foi observado que este elemento ocupa a posição de substitucional do gálio a 47 % e uma posição próxima do intersticial O a 53 %. Após um recozimento a 800 °C estas frações alteram-se para 76 % na posição SGa e 24 % na posição O. Por fim, a medida de magnésio verificou que este elemento, quando implantado à temperatura ambiente, ocupa as posições substitucional do gálio a 76 % e uma posição próxima do insterstitial HA com uma ocupação de 24 %. Quando implantado a 800 °C a medida realizada com o detector timepix mostrou que este elemento passa a ocupar estas mesmas posições com frações de 91 % e 9 %. Utilizando estas medidas como base de comparação entre os detetores pad e timepix foi concluído que ambos resultam em frações relativas semelhantes, no entanto, existem e discutem-se algumas diferenças no total da soma das frações e consequentemente na determinação da fração *random*, definida pelo conjunto de isótopos em posições não caracterizadas ou em sítios de baixa simetria cristalina da amostra.

Esta tese conclui-se com uma reflexão sobre como as ferramentas aqui desenvolvidas podem ser utilizadas na avaliação da contribuição de futuras melhorias da técnica, utilizando como medida a redução das incertezas nos resultados. Com isto, também identifica alguns pontos merecedores de atenção e desenvolvimento no futuro, como a necessidade de melhor caracterização e modelização do ruído de

fundo.

Palavras Chave

Canalização eletrónica de emissão; Detetores sensíveis à posição; Timepix; Modelação de experiências; Estimação de parâmetros;

Contents

Acronyms

2D	two dimensional
ADC	Analogue to Digital Converter
DBSCAN	Density-Based Spatial Clustering of Applications with Noise
DSP	Digital Signal Processor
EC	Emission Channeling
EC-SLI	Emission Channeling with Short Lived Isotopes
ECP	Electron Channeling Patterns
EBSD	Electron Backscatter Diffraction
ERDA	Elastic Recoil Detection Analysis
g.o.f.	goodness of fit
GPS	General Purpose Separator
HRS	High Resolution Separator
IC	Integrated Circuit
PDF	Probability Density Function
PIXE	Particle-Induced X-ray Emission
MC	Monte Carlo
n.d.f.	number of degrees of freedom
NORM	Naturally Occurring Radioactive Materials
NRA	Nuclear Reaction Analysis

p.d.f.	probability density function
PSD	Position Sensitive Detector
LHC	Large Hadron Collider
RBS/C	Rutherford Backscattering Spectrometry with Channeling
RILIS	Resonance Ionization Laser Ion Source
rms	root mean square
RT	Room Temperature
SD	standard deviation
ToA	Time of Arrival
ToT	Time over Threshold
IBA	Ion Beam Analysis
CIFS	Common Internet File System
GUI	Graphical User Interface
.csv	comma separated values

Nomenclature

Statistics symbols

$-LL$	Negative log likelihood.
$\boldsymbol{n}$	Set of the number of counts per bin, $\{n_1, ..., n_{N_{bins}}\}$
$\chi_{P(k)}$	Pearson chi-square with k degrees of freedom.
$\hat{\theta}$	The estimator of θ.
$\sigma^2_{\hat{\theta}}$	Variance of an estimator.
$\sigma_{\hat{\theta}}$	Standard deviation of an estimator.
θ	A parameter or set of parameters of the physical model.
θ_{obs}	The observed value of θ.
$b_{\hat{\theta}}$	Bias of an estimator.
$E(\hat{\theta})$	The expected value of the estimator $\hat{\theta}$.
$f(x)$	The p.d.f. of a random variable.
H	Hessian matrix.
k	Number of degrees of freedom of the chi-square distribution.
$L()$	The likelihood function.
N	The number of random variables in the set X.
N_{bins}	Number of bins in a histogram.
N_{cts}	Number of counts in an experiment.
n_i	Number of counts in bin i

p_i	Probability of an event occurring in bin i.
S	Domain of x that defines the space of possible values for the random variable X.
v_i	Expected number of counts in bin i.
X	A random variable or a set of random variables.
x	A possible value for the random variable X.
X_i	A single random variable belonging to the set of random variables X.

Channeling data fitting symbols

(ϑ, ω)	Horizontal and vertical angular positions with reference to the center of the detector.
χ_1	Simulated yield pattern for site #1.
$\Delta\hat{\theta}$	Systematic uncertainty of an estimator.
$p.d.f.\,(\theta)_i$	Hit location p.d.f. dependent of the parameters in θ at bin i.
E_i	Expected number of counts in bin i.
f_1	Occupancy fraction for site #1.
$N(\vartheta, \omega)$	Number of counts in the measured pattern at location (ϑ, ω).
N_R	*Random level*, defined as the expected number of counts if the sample were amorphous.
O_i	Observed number of counts in bin i.
Y	Yield pattern resultant from weighted site contributions.

1

Introduction

Semiconductor devices are widespread over a wide field of technological applications. Computing devices, sensors, displays, lasers, solar panels, these are just a few of the areas that benefit from the ongoing developments in semiconductor technology.

The large set of existing semiconductor characterization techniques have been essential tools for the constant development of related technologies. One characterization challenge faced by the more common techniques is the measurement of the lattice location of small concentrations of impurities (or specific dopants) in semiconductors. Depending of the lattice site occupied by an impurity it can give different contributions to the semiconductor Fermi level or cause alternative intermediate energy levels in the semiconductor band-gap. These lattice site related effects are therefore very relevant to the impact that impurities have on the electrical, optical and magnetic properties of a semiconductor. The ability to measure the lattice site of an impurity and learn on how to possibly control it, is therefore of great value.

One lesser known characterization technique but unique in its abilities to perform element specific lattice site location studies in semiconductors is the Emission Channeling (EC) technique.

1.1 Emission channeling for impurity lattice location

Emission Channeling (EC) is a nuclear technique that uses the emission of charged particles from the radioactive decay of isotopes implanted into single crystals, for the measurement of the lattice site location of the corresponding impurity element [1–6]. By repeating the lattice location measurements after several high temperature annealing steps, EC also provides insights on how to control the site change of dopants after implantation.

This technique is in many ways similar to Ion Beam Analysis (IBA) techniques that use ion beams to study crystals such as Rutherford Backscattering Spectrometry with Channeling (RBS/C), Particle-Induced X-ray Emission (PIXE), Elastic Recoil Detection Analysis (ERDA) and Nuclear Reaction Analysis (NRA). In fact, all of these techniques use charged particles traveling in crystals where they can experience channeling effects [7] and can be used to assess, e.g., the depth profile of the implanted species, crystal defects or lattice site location [8–10]. Some examples of element lattice site location using different IBA techniques can be seen in [11–14].

The ion channeling effect can be intuitively understood by looking at a single-crystal lattice structure along different orientations as shown in Fig. 1.1. The ordered distribution of atoms in the crystal structure creates channels of empty space where positively charged particles can travel with lower resistance / scattering. In this situation, positive ions travelling in between the atomic strings are gently steered by the atomic potentials of the host atoms to the center of the channels, with a reduced scattering yield. Contrarily as to what happens with ions, in electron channeling the negatively charged electrons are attracted to the positive nuclei of the host crystal and consequently will preferentially travel along the atomic strings, not in between them. Complementary to the channeling effect there is a blocking effect. Blocking can occur for a particle travelling in channeling directions but for starting conditions that position it in front of a high potential and that consequently blocks its passage. For example if a positive ion is positioned in front of an atomic string (or an electron directed at the space between atomic rows) it will be blocked (or dechanneled) despite travelling in a channeling direction.

A comprehensive explanation of the theory of ion channeling was published by Lindhard in the 1960s [15, 16]. This treatment simplified the description of the crystal atomic potentials by using the concept of atomic strings formed by the atoms along a specific crystal channeling axis. In his work Lindhard introduced the concept of critical angle ψ_1 which defines the angles below which an energetic ion will channel through a crystal and which can be calculated from,

$$\psi_1 = \sqrt{\frac{2Z_1 Z_2 e^2}{dE}}, \tag{1.1.1}$$

where Z_1 and Z_2 are the atomic numbers of the ion and substrate atom, e the elementary charge,

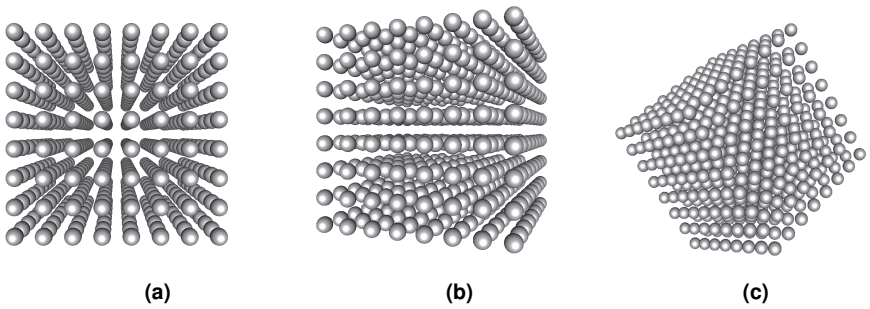

Figure 1.1: Representations of a cubic lattice viewed under three different orientations. (a) view through the $\langle 1\,0\,0 \rangle$ axis channeling perspective, (b) view through a planar $(1\,0\,0)$ channeling perspective and (c) view from a random direction.

d the distance between atoms along the channeling rows, E the ion energy. Furthermore, Lindhard established a formula for the minimum yield χ_{min}, which characterizes the channeling yield when the ion beam direction is aligned with the crystal axis, as

$$\chi_{min} \approx \pi a^2 dN\,, \tag{1.1.2}$$

where a is the Thomas-Fermi screening length and N the atomic density.

Another concept that Lindhard described in his 1965 publication [16] is the concept of reversibility. This concept states that there is equivalence between the process of having a particle (ion beam) coming from outside with a certain angle, then channel inside a crystal and hit a crystal atom and the inverse process of having that particle emitted from the (hit) atom and having it channeling towards the outside and leave the crystal under the same angle as the incoming particle. Channeling reversibility has also been verified in electron diffraction [17]. This concept is fundamental in computational simulations as inward simulations are a simpler way to construct the expected channeling yield patterns and allow to simultaneously obtain results for many different positions of the actual probed (scattering or emitting) atom.

There are fundamental differences upon simulating the particle flux density in channeling conditions for ion channeling and electron/positron channeling. At common ion beam energies of a few MeV with relatively heavy not relativistic particles the description of ion channeling has a classical mechanics approach, being quite different from electrons as they require a quantum mechanical description of their interaction with the periodic potential of the crystal. Section 2.2 goes into general concepts on the modelling processes of electron channeling but for a complete formalism describing electron channeling the references [18–21] are recommended.

In EC experiments, the source of charged particles is the decay of implanted radioactive probes

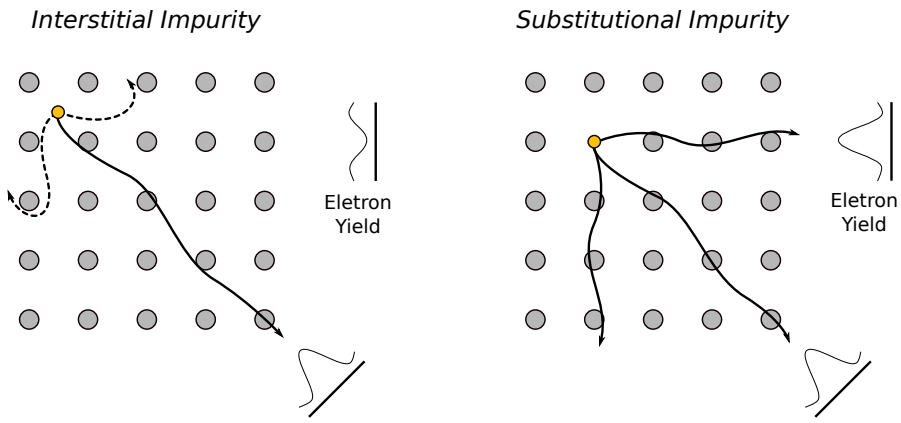

Figure 1.2: Channeling schematics for a beta emitter impurity in a cubic lattice. Depending on whether the impurity is in an interstitial site or a substitutional site channeling (solid lines) or blocking (dashed lines) will occur. The channeling effect causes a strong peak in the angular-dependent emission yield, while blocking (rather, enhanced scattering of electrons) will result in a shallower dip.

(alpha, beta+, beta-, conversion electrons) which when emitted in highly symmetric crystal directions can be channelled or blocked, in their way out of the crystal. The technique measures the lattice sites of the probes by using the fact that the emission yield of charged particles around major symmetry axes is highly dependent on the lattice site of the emitter. The angular emission yield anisotropy is nowadays measured by a two dimensional (2D) Position Sensitive Detector (PSD) at 30-60 cm away from the sample crystal that was implanted with the radioactive probe. The sample is mounted on a goniometer allowing to orient one of its principal crystalline axes directed towards the detector. The resulting particle yield angular distributions measured at a set of complementary axes are then fitted with previously done simulations. To identify the probes' lattice sites and to quantify their respective occupancy fractions, the fits rely on a large library of simulated data for each of the measured axes, specific of each particle and its energy spectrum as well as implantation conditions, that describe the expected angular emission yields for a large set of possible sites that could have been occupied by the implanted probe.

Fig. 1.2 exemplifies how the particle yield anisotropy and the combination of channeling and blocking conditions can be used to determine the lattice site location of a radioactive probe element in a typical electron EC experiment. There it can be seen how substitutional occupations of the probe element lead to the emitted electrons to experience channeling along all the crystal directions and how interstitial probe occupation lead to electron channeling or blocking effects depending on the crystal atomic axis direction that is being observed. The example in the figure also highlights the necessity of measuring several, complementary, directions to clearly identify the probes' lattice sites.

The EC process gives a strong advantage over alternative IBA methods for lattice location using ion beams due to its increased sensitivity to impurities. In fact, EC in comparison with RBS/C, the most common of the mentioned techniques, can work at impurity implantation fluences that are about four

orders of magnitude lower and is sensitive to elements lighter than the host crystal, making it an ideal method to study highly dilute systems, e.g. with implantation impurity levels well below $\sim 1 \times 10^{14}\,cm^{-2}$. On the other hand, EC with electrons has no depth resolving power.

EC can be observed with any radioactive decay producing highly energetic charged particles, i.e. alpha, beta, positron and conversion electron emitters. From these, beta emitters are the most commonly used, followed by conversion electron emitters, due to their wider availability of adequate isotopes of the desired probe element. This happens as alpha emitters are limited to heavy nuclei or very light nuclei such as ^{8}Li and ^{8}B, also there are limited positron emitters that could be used in EC as most neutron-deficient nuclei decay by electron capture.

The "Emission Channeling" group, where this work is integrated, is mainly a collaboration between the University of Lisboa, IST and the University of Leuven, IKS. The three experimental off-line and the on-line (EC-SLI) setups are located at ISOLDE (CERN) [22] where emission channeling experiments in combination with 2D PSDs are performed since 1996 [23].

1.2 Position sensitive detectors for electron emission channeling

The resulting two dimensional (2D) electron yield map from an Emission Channeling (EC) measurement done with a Position Sensitive Detector (PSD) is named as a “channeling pattern”, see Fig. 1.3. Channeling patterns are a small angular portion of the anisotropic particle yield emission that is similar to a Kikuchi pattern. Kikuchi patterns are diffraction patterns produced by the scattering of electrons in a crystal, this kind of patterns is frequently seen in electron microscopy techniques. From one pattern with enough statistics one can easily identify channeling effects from planes and axes and, with some experience, use already the visual information to get a qualitative first guess of the predominant occupied lattice site.

The introduction of 2D PSDs was a big step in the improvement and reliability of the quantification of electron EC results [23]. The simple fact that a large set of angular positions are measured simultaneously without any need for some sort of time normalization is already a great advantage as it reduces the complexity of the measurement. Additionally, an angular coverage is more time efficient than a scan, therefore reducing the required implantation fluence of isotopes which reduces the implantation damage. Another effect is that by measuring 2D channeling patterns it is rather straightforward to properly orient a sample towards the detector in a short time. By far the most significant reason for the use of PSD is that by fitting the channeling pattern with simulations the quantification process is much more precise.

When choosing a detector for electron emission channeling there are some aspects to consider. To begin with, the detector must be able to count incoming particles with sufficient position resolution. Then, a fast count-rate is also essential, in particular if it is intended to be used with short lived isotopes.

It also needs to perform stable over time, with low electronic noise, work in a vacuum and be radiation resistant. Finally it is advantageous if it has low sensitivity to background gamma and x-ray radiation and if it is energy sensitive, the last point being useful to plot 2D patterns from selected conversion electrons energies of the required probe element, eventually, allowing to strongly reduce the undesired event contributions from decay of isobaric implanted contaminants.

The detectors that were acquired in the late 1990s and early 2000s in a combination of synergies at CERN are called pad detectors [24, 25], see Fig. 1.4. The term "*pad*" is used as the sensor cells are much larger than regular pixels. While pixels are usually smaller than 100 µm, the type of pad detectors used here have $1.3 \times 1.3\,\mathrm{mm}^2$ size pads. The pad detectors use a Si sensor that can have thickness of 0.3 mm, 0.5 mm or 1.0 mm and are divided in a mesh of 22×22 pads.

In the pad detector the 484 pads are divided into four groups, one for each detector side. Each pad signal connects to one of the 128 inputs of one of the four Integrated Circuit (IC) chips located at each of the sensor sides. Each of the chip input signal lines contains a preamplifier, shaper and sample/hold circuit which are then multiplexed into a single Analogue to Digital Converter (ADC).

In the older versions of the detector, a backplane signal common to all pads is connected to a preamplifier and is used as a trigger to initiate the readout of all pads of the detector, and numerical analysis of the multiplexed readout is performed by a Digital Signal Processor (DSP). In the most recent version, the detector uses self-triggering preamplifier chips at the readout of each pad and can reach a count-rate of 3500 counts/s before the readout dead-time effect becomes noticeable, after which saturation occurs at 5000 counts/s. After being processed by the chip, the digitized signals are sent by an optical fiber from the ADC next to the detector chamber to a data acquisition computer.

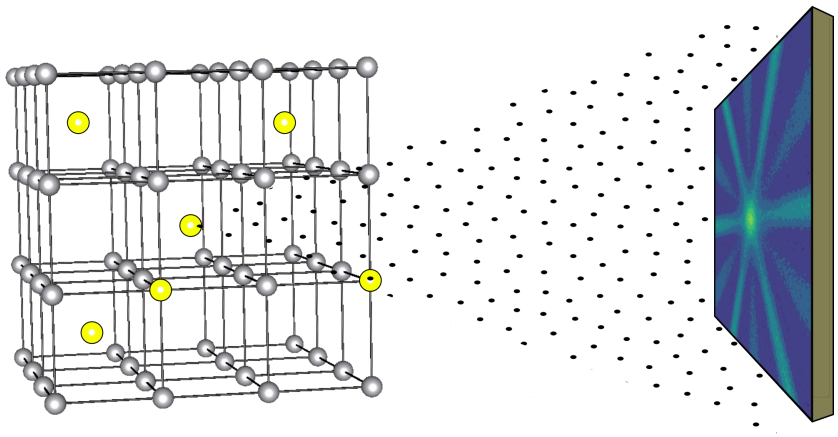

Figure 1.3: Visualization of an EC experiment using a PSD. The decay radiation of the implanted radioactive isotopes (in yellow) caries information on the lattice site location and their distribution. The anisotropic emission yield is measured by the PSD as a channeling pattern.

A detector from the Medipix collaboration

The Medipix collaboration is based at CERN and joins several universities and institutes for the development of high density pixel detectors. The collaboration started in the late 1990s with the development of the medipix1 chip [26]. This first detector with a pixel mesh of 64 $\times$ 64 pixels of 170 µm size was the starting point for what is now a more than two decade long series of developments in high energy physics, medical imaging, dosimetry, x-ray crystallography, electron microscopy and many other applications by the more than thirty collaborating teams [27, 28].

In 1999, the medipix-2 colaboration was formed [27]. From it, two types of detector chips were created, the medipix-2 [29] and the timepix [30]. Both of these chips have a high pixel density as being formed by 256 $\times$ 256 pixels of 55 $\times$ 55 µm^2 size. A variety of sensors have been developed that can be connected to the medipix chips, but the most common are made of high resistivity Si, GaAs, CdTe or CdZnTe. The connections between each of the chip pixels and the sensor on top of it are made by bump bonds. The charge collected by each pixel is amplified and digitized at the pixel level. Then, at the closure of a time shutter, the data stored in the pixels is read out into frames.

The first chip from the medipix-2 collaboration the medipix-2 (chip), was developed for use in photon counting detectors; thus, applications in x-ray imaging raised an early interest. The second chip, the timepix, has programmable pixels that can be set to different working modes. The three possible pixel mode settings are, the Time of Arrival (ToA) mode, where each pixel counts the time from the particle arrival until the shutter is closed. The counting mode, where each pixel counts the number of particles that reached the pixel. At last, the Time over Threshold (ToT) mode, which measures the time while a detected pulse is above a defined threshold, to measure the deposited energy in the pixel. This versatility captured users from many fields.

At this point, as a result from CERN synergies between our team and the Medipix collaboration a timepix detector was acquired for use in EC experiments at ISOLDE, see Fig. 1.4. This detector is a timepix-quad with a 300 µm silicon sensor. The quad detector is formed by four timepix chips arranged in a square that results in a 512 $\times$ 512 pixel mesh.

To be used in EC, timepix detectors can be set in ToT mode, if energy discrimination is useful for selecting particles, or set in counting mode, if the probability of multiple hits in each pixel during the readout time frame is significant, due to the source intensity. Because the data is periodically read in frames, instead of a continuous stream there is a trade-off decision to be made between slower or faster frames depending very much on the source intensity, in order to minimize as possible the events pileup. The problem actually is that, with such small pixels, one electron event is made of several pixels due to the multiple scattering inside the sensor and the creation of secondary electrons. Generally the count-rate achieved with the timepix is lower than with the pad for the same radiation intensity due to the larger dead-time of the timepix chip; in normal conditions a count-rate of 4000 hits/s was achieved.

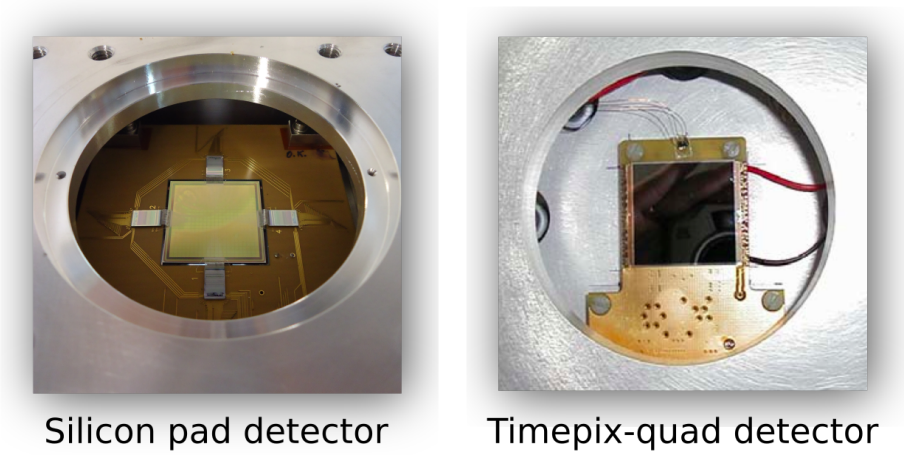

Figure 1.4: Side by side view of the pad and timepix-quad detectors in their vacuum chambers as used in the EC-SLI setup.

After the development of the medipix2 and timepix chips new challenges were addressed with the creation of the medipix-3 collaboration. From it, two new detector chips were developed, the medipix3 [31] and the timepix3 [32]. The main requirement for these new detectors was the reduction of the dead time. The medipix3 chip achieved this by having two counters per pixel that can be programmed so that one counter is being read while the other keeps counting. In addition, there is the possibility to connect the detector to super pixels of 110 µm composed of four regular pixels, in this way each super pixel can have up to eight counters which can be set with different energy thresholds each. The timepix3 chip used the knowledge gained from the medipix3 development and achieved some very interesting characteristics. Firstly, new working modes for the pixels were implemented, in one mode the ToA and ToT can be measured simultaneously, in another mode a secondary and faster clock is used to obtain a more precise ToA and the last mode measures the ToA and integral charge ToT. Secondly, the readout was improved so that in addition to the still available frame based readout there is a data driven readout mode that sends out the pixel data after every hit. With the data driven mode an impressive count-rate of 40 Mhits/s/cm^2 can be achieved.

1.3 Objectives

In 1996, two dimensional (2D) Position Sensitive Detector (PSD) were used for electron Emission Channeling (EC) experiments for the first time. The corresponding pad detectors were a spin-off that resulted from the fruitful collaboration with the groups at CERN that were developing PSDs for the purpose of detecting very short lived particles created during high energy particle collisions.

Almost exclusively used at ISOLDE, the unique factory of radioactive isotopes in the world with

enough intensity, purity and variety, EC has been since then successfully providing results on the determination of lattice sites of, e.g., Er [33], Cu [34] and Fe [35, 36] in Si, As [37], Fe [38] and Ni [39] in ZnO, transition metals in Ge [40, 41] and Mn [42] and Mg [43] in GaN.

Over the time, some improvements have been made to the technique such as implementing faster pad detectors dedicated to short lived isotopes, updates of the implantation chambers and the introduction of background corrections, obtained by Monte Carlo (MC) simulations of electron scattering from the sample and the walls of the experimental vacuum chamber.

Regarding improvements in the detection systems, there has been an early on update of detector at the online setup that increased the readout speed but besides this the currently used detectors have been the same since the establishment of the technique at ISOLDE.

Due to the ageing of the pad detectors, it has been a long term objective to update the PSD technology and to prepare the data acquisition and analysis methods for the next generation of detectors. The possibility of using medipix/timepix detectors has been explored in the past by L. Amorim during her PhD [44] (small 256 $\times$ 256 pixels - off line experiments with long lived isotopes) and by me during my masters [45] where the same type of detector was used to perform 2D analysis of Rutherford Backscattering Spectrometry with Channeling (RBS/C) patterns using He^+ beams and alpha sources. These steps have previously aggregated the required knowledge and tools, and also demonstrated the feasibility of using medipix detectors for channeling experiments.

This thesis work starts with the introduction of a timepix-quad detector dedicated to perform Emission Channeling experiments with Short Lived Isotopes at the EC-SLI setup at ISOLDE, a step forward that greatly improves the resolution of the channeling patterns measured. Then follows with the establishment of the additional tools necessary to set up a new working detection and analysis system.

In addition to the technical part of the installation and tool development there are some questions from the point of view of the technique improvement that arise. For instance, if the substantial increase in detector resolution will be able to bring more accurate lattice location results and if it could add new relevance to the results, such as the detection of low occupancy sites.

Following these initial considerations the defined objectives of this thesis are:

- **Build a working system interface for the use of the timepix detector.** Connect the detector to the Emission Channeling with Short Lived Isotopes (EC-SLI) implantation vacuum chamber. Set up the necessary computing systems for the data acquisition;
- **Develop new and adapt existing software necessary for the use of high density pixel detectors.** Some of the expected problems from the use of the timepix detector are a result of the small pixel size. For instance the scattering of electrons in the sensor and consequent activation of several pixels per hit, as well as, the impact on the chi-square fitting procedure resulting from the reduced number of counts per pixel for a pattern with similar total number of counts as a pattern

measured with the pad detector;

- **Use timepix to perform lattice location experiments in GaN.** Test the detector in different situations to evaluate the performance. Then compare the results with control data taken with the older pad detector;
- **Evaluate the effect that the angular resolution of the experimental anisotropy pattern has on the lattice location of radioactive probes by EC.** To identify a certain lattice site, the EC analysis requires, per each observation axis, libraries with hundreds of simulated patterns covering all possible substitutional, interstitial and displaced lattice sites. With the aim of establishing guidelines and optimizing future experiments based on realistic expectations, a combined, intensive and thorough analysis of these libraries needs to be done to understand whether better angular resolution in EC patterns is required for better measurements of lattice site location and respective fractions. This study must be further combined with the analysis of the uncertainties resulting from fitting experimental data with different angular resolutions.;
- **Assess whether hit cluster analysis can be used to improve the detector position resolution or reduce the gamma background.** When electrons emitted upon the radioactive decay hit the sensor, the deposited energy can be detected by several pixels of the detector due to the multiple scattering of electrons until all energy is deposited. Assess if the energy distribution of a cluster of activated pixels can be used to improve the position resolution, determining the pixel where the initial electron entered the sensor. In addition, appraise the effectiveness of using the cluster size as a method of selectively removing gamma and x-ray background events.

2

Experimental and Theoretical Methods

This chapter is about the framework of experimental and theoretical methods used in emission channeling experiments and analysis. In detail, here the production and implantation of radioactive isotopes into semiconductor single crystalline samples, the concepts behind the emission channeling simulations, the position sensitive detectors and the background for the statistical methods used in the analysis will be addressed.

As a large portion of this thesis focuses on the Position Sensitive Detectors (PSD) and analysis methods, these topics will be explained more in depth while other subjects will be concentrated to essentials and more detailed descriptions will be referenced.

2.1 Online production and implantation of radioactive isotopes at ISOLDE

Electron Emission Channeling (EC) starts with the implantation of a radioactive beta emitter into a single crystal. It is this radioactive isotope that, by emitting a beta particle, probes the lattice environment at

the location of the isotope nucleus with remarkable position sensitivity and element selectivity.

The incorporation of radioactive impurities into a single crystal by ion implantation is crucial for fully exploiting the potential of the EC technique. It allows to control the dopant concentration through the beam current, mass and nuclear charge of the implanted ion, the implantation depth profile can be calculated from the beam energy, it allows precise control of the implanted area, which is important to keep a good angular resolution, and enables the whole experimental process to be completed during the time of the nuclear decay even for short lived isotopes. Additionally this method is not foreign to the semiconductor industry as ion implantation is a common doping technique. The standard method for removing implantation damage is with high temperature annealing which is equally part of the experimental process here performed.

For this thesis the isotope production was realized at ISOLDE [22, 46], the online isotope mass separator located at CERN, Switzerland. Fig. 2.1 shows a layout of the facility and is a useful starting point for the understanding of the underlying mechanism.

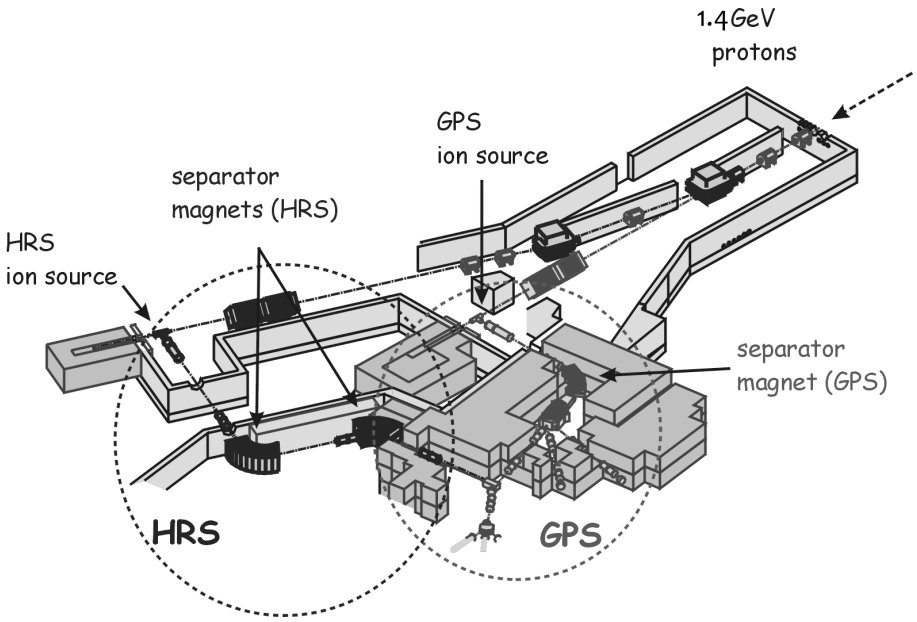

Figure 2.1: Schematic representation of the implantation facility at ISOLDE. Isotopes are produced by directing a high energy proton beam of 1.4 GeV into a target. As the proton beam induces the fragmentation and/or fission of the high mass elements existing in the target a wide variety of isotopes are created. The isotopes are then ionized and accelerated to the mass separator for later distribution to the General Purpose Separator (GPS) or the High Resolution Separator (HRS) magnets.

ISOLDE takes advantage of the high energy beams produced at CERN by receiving a proton beam from the Proton Synchrotron Booster, which is the second stage of acceleration for the Large Hadron Collider (LHC). The proton beam has an energy of 1.4 GeV and a current up to 2 µA. The beam, after its arrival to ISOLDE, is directed to one of two targets, each connected to its respective separator. They are the General Purpose Separator (GPS) or the High Resolution Separator (HRS). Inside the

targets isotope production happens as heavy elements, such as ^{238}U, present in the target material are fragmented or fissioned creating a large variety of lighter radioactive isotopes.

The target, which is heated to about 2000 °C by means of a resistive current passing through it, releases volatile isotopes which are then ionized before being accelerated. The ionization can be done by one of the following three methods: One, by surface ionization which consists of heating the metallic surfaces at the exit of the target so that electrons get detached upon collision with the surface. This method is only suitable for chemical elements with low ionization potential, mainly the alkali metals, some alkaline earths, the rare earths and a small number of others, e.g. Ga or In, and cannot discriminate between specific elements. Two, by plasma ionization which requires the isotope to pass by a plasma discharge and has the least element selectivity. Three, by laser ionization which uses a combination of lasers to selectively ionize a desired element. At ISOLDE the laser ionization is done by the Resonance Ionization Laser Ion Source (RILIS) [47–50]. Once the ions are produced, they are then accelerated up to 60 keV in a continuous beam, mass separated by a separator magnet and guided to the experimental beam line.

At the end of the beam line the Emission Channeling with Short Lived Isotopes (EC-SLI) implantation chamber is located, whose schematics are shown in Fig. 2.2. The vacuum chamber contains a sample holder, a goniometer and a beam collimator. Connected to it are two position sensitive detectors, a timepix-quad and a pad, these will be later described in section 2.3. The detectors can be positioned at two distances, the standard position, which is shown in Fig. 2.2, leaves the detectors at a distance of about 31 cm from the sample, alternatively an extension tube can be inserted between the detector and the chamber flange which increases the distance by 282 mm (see table 3.1 for a detector distances summary). This extended configuration almost doubles the angular resolution in exchange for a smaller solid angle.

The radioactive beam that comes from the separator is collimated to a diameter of 1 mm, this makes the implantation area (the beam spot) well defined. The sample is carefully attached to a sample holder that is connected to a goniometer for orientation, it also includes a thermocouple for temperature measurements and a heating circuit that can reach 900 °C. The goniometer is used to orient a chosen sample axis towards the detector. The available orientation degrees of freedom are the horizontal and vertical positions x, y and z, the rotational position around the vertical axis M_1, the rotational position around the sample's normal M_2, and the rotational position around a horizontal line perpendicular to the sample's normal M_3. For most cases, x, y, z and M_3 are set at the beginning of the experiment and then only the M_1 and M_2 are needed for adjustments and switching between axes. Because of the high temperatures reached in the chamber there is also the option to use a thermal shield made of reflective mylar foil in order to protect the detector from thermal radiation.

Inside the chamber there is also a retractable Faraday cup whose purpose is to measure the ion

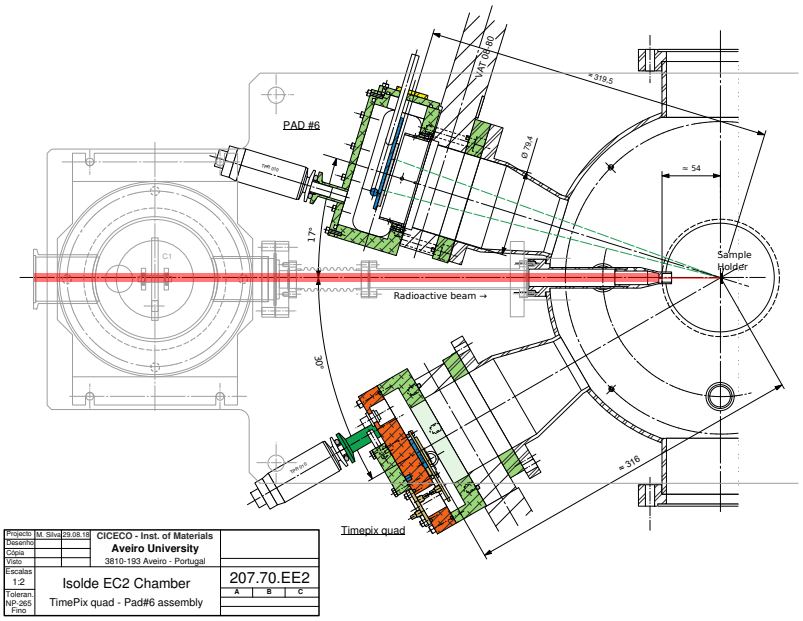

(a)

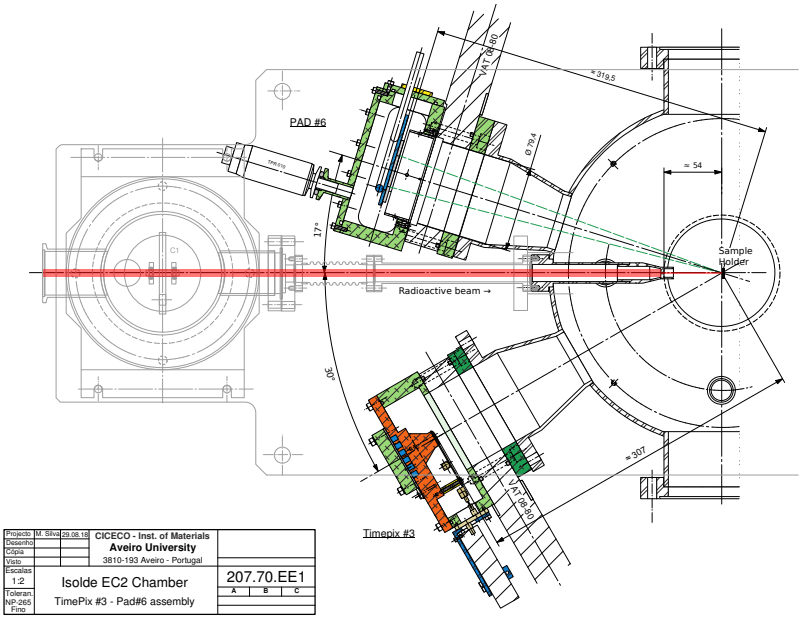

(b)

Figure 2.2: Schematics of the EC-SLI implantation and on-line measurement chamber at ISOLDE as seen from above. The radioactive beam (highlighted in red) enters the chamber from the left side, passes through a collimator and hits the sample located at the center of the online implantation chamber where the Position Sensitive Detectors are connected. The collimator has a 1 mm diameter hole that ensures that the implantation position is well defined and that a reasonable angular resolution is achieved. Both figures show the same chamber with a pad detector connected to the flange shown at the top located at an angle of 17° with the beam. Connected to the flange shown at the bottom and at an angle of –30° with the beam, figure a) shows the timepix-quad detector and figure b) shows a timepix3, each inside their respective vacuum chamber that includes water cooling, a vacuum-air feed-through connector and a vacuum valve. See section 2.3 for a description of the detectors. Not shown in the figure is a smaller implantation chamber, which is located to the left side in front of the EC-SLI setup, and is used to prepare samples for off-line measurements.

current inside the chamber prior to the sample implantation. This information is later used to calculate the implantation fluence.

Implantations into single crystals are done at an angle that avoids strong channeling conditions as it would complicate the simulation of the implantation depth. Hence implantations into off-channeling directions are comparable to implantations into amorphous materials, the implantations are usually done when the sample normal faces the pad detector, i.e. under an angle of 17°. In these conditions the implantation depth profile can be simulated by Monte Carlo (MC) methods with the SRIM software [51].

2.2 Emission channeling computational simulations

Performing Emission Channeling (EC) simulations is one of the more complex and more time consuming parts of the EC lattice location experimental process. Yet, it is essential for the quantification of lattice position and occupancy fractions. It is with simulations that the theoretical two dimensional (2D) yield patterns are produced, for precise experimental conditions (measurement temperature, implantation depth profile, etc), that are then to be fitted with the measured channeling patterns.

When simulating ion channeling the approach is nowadays exclusively to use Monte Carlo (MC) methods, but in the case of electron emission channeling even though the emitted electrons have high energies a quantum mechanics description is necessary to describe their movement in the periodic atomic potential. The general approach to performing this kind of simulations is with the use of the many-beam dynamical theory of diffraction [18–21]. Besides its use in EC simulation, the many-beam method is well known from the electron microscope community and is commonly used in the Electron Channeling Patterns (ECP) and Electron Backscatter Diffraction (EBSD) techniques [52–55].

Electron EC differs from these techniques as electrons originate from the nucleus, not from an external source, and have energies from 0 to a few MeV, much higher than the tens of keV present in an electron microscope. Due to these differences a specific software for EC was written in fortran by Hofsäss and Lindner [1] and later updated by Wahl [23].

Consideration of whether some software from the electron microscope could be used in emission channeling may be worthwhile as these communities have spent decades developing many-beam based software having both commercial and open source software. Nowadays these program packages have a lot of features that could improve EC if imported, such as easy introduction of crystal structures, modelling of crystallographic defects, detector response and noise modelling, as well as, advanced computing techniques for producing faster results. An open source package that could be useful to include in such considerations is EMsoft [56]. Although it could be possible to adapt such open source software to the needs of EC, one must also remember that this would be a costly and long project.

The simulation approach used here for producing an emission channeling pattern does not work by

simulating the path of an electron after being emitted by a nucleus at a given site, instead the simulation uses the reciprocity in electron channeling and is based on the reverse process (see section 1.1). The meaning of this is that the simulation works in time reversal, i.e., it considers the electron as a plane wave entering the crystal from which it calculates the flux density inside the unit cell as a function of depth. It is then, that the channeling yield is calculated by comparing the probability, of the incoming electron flux, of interacting with a dopant in a specific lattice site, versus, the probability of interacting with a randomly distributed dopant in the lattice cell.

A starting point in the simulations is to construct the atomic potential inside the crystal, which is done by a combination of Doyle-Turner atomic potentials for each contributing lattice atom. Since the electrons travel at a very high speed and at a small angle from the channeling axis the electron movement can be decomposed into two components. Of these, one component describes the electron behaviour parallel to the channeling axis and is described by a Klein-Gordon equation, the other component describes the electron behaviour in the 2D plane perpendicular to the channeling axis and is described by Bloch wave solutions of the Schrödinger equation in a periodic potential. The crystal potentials are defined as the projection of the Doyle-Turner atomic potentials along the channeling axis. The number of beams in the many-beam formalism is related to the number of energy states that the Bloch waves can attain. Consequently calculations of higher energy electrons need to include more beams, as these electrons can occupy higher energy states.

Another factor that enters the calculations is the root mean square (rms) thermal vibration amplitude, u_1. For the host atoms, the vibration term u_1 enters the Doyle-Turner atomic potential calculations and influences the energy levels of the Bloch wave solutions, and, more important, also the dechanneling of electrons. The host atoms respective u_1 values are obtained from the literature from X-ray or neutron diffraction experiments. Concurrently, the rms vibration u_1 of the implanted isotopes also needs to be considered during the yield calculations from the electron flux density. The dopant u_1 is usually unknown. Hence it is customary to include in the many-beam simulations a range of u_1 values that can be tested against the measurement data.

The simulation of each independent angular direction produces a 2D pattern where each point represents a normalized yield, χ. The yield, χ, is said to be normalized as it represents the expected yield in comparison to a sample where no channeling effect is present, i.e., where the flux density in the unit cell is uniform. This means that an angle with $\chi > 1$ would result in more counts than an amorphous sample and vice versa. This concept of normalized yield is therefore key to the theoretical treatment and experimental analysis of the channeling effect. For example, a direction with $\chi = 1$ is called a *random* direction and a flat uniform pattern can also be called a *random* pattern.

In practice, random patterns or, more specific, the random component of a channeling pattern can have several distinct causes. It can be due to radiation background, scattered electrons that are devoid

of channeling information, an amorphous sample or even a random distribution of emitting probes within the crystal lattice unit cell. As will be seen in section 3.3, the quantification of the random component and its decomposition of factors is an important issue in the analysis of EC results.

2.3 Data acquisition and treatment with the timepix-quad position sensitive detector

Section 1.2 has introduced the Position Sensitive Detectors (PSDs) used in Emission Channeling (EC). This section will now go into the details of how the timepix-quad detector works, how the data is collected and what kind of treatment is required to produce a two dimensional (2D) channeling pattern from it.

The timepix-quad detector is composed of 4 timepix chips connected in a square which combined have a mesh of 512 $\times$ 512 pixels each with 55 $\times$ 55 µm^2. To the 4 chips a high resistivity silicon sensor of 300 µm thickness is bump bonded to the pixel electronics. The 262 144 pixels form a regular mesh over the detector's area except at the contact points between chips where the distance between pixels has an additional 220 µm, the equivalent of four pixels, as is shown in Fig: 2.3.

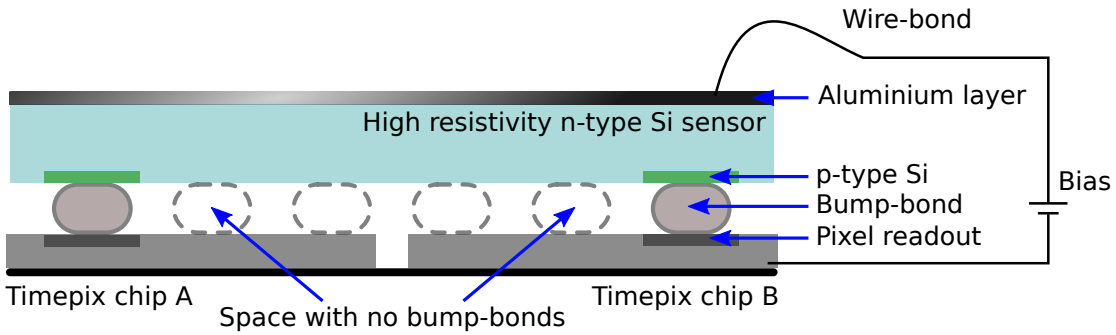

Figure 2.3: Cross section of a timepix-quad detector at the junction of two chips. The space in between chips has an equivalent size of about two pixel for each side. This geometry results in the oversized central pixels having effective size of three pixels.

When an ionizing particle reaches the sensor, the positive part of the charges (holes) created in the silicon drift to the pixel cell due to the applied bias. Figure 2.4 shows the schematics of the pixel cell. The pixel electronics are divided into an analog and a digital part. In the analog part there is a pre-amplifier and a discriminator whose function is to only trigger if the signal is above the threshold. There is also a 4-bit threshold tuner that can correct for the specific noise levels of each pixel. Also in the analog part, the test input is used to send test pulses for pixel testing. The signal is then digitized according to the pixel mode setting (Time over Threshold (ToT), Counting or Time of Arrival (ToA)) and stored into a 14-bit register.

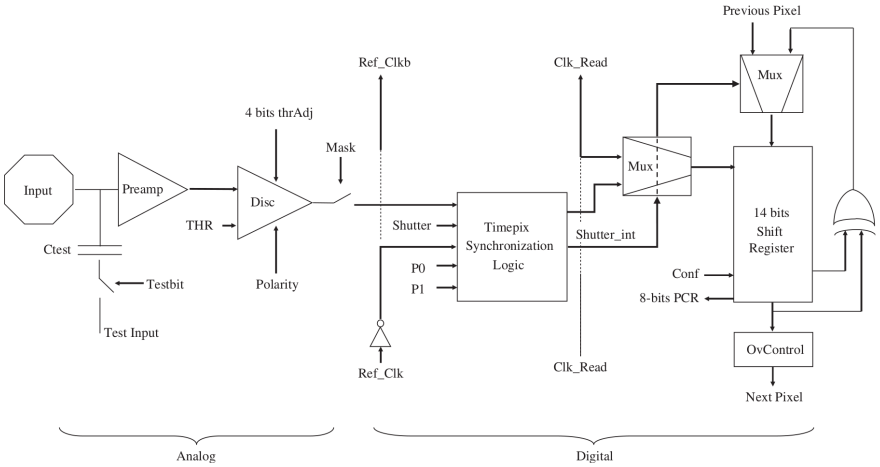

Figure 2.4: Schematics of a timepix pixel cell. Figure from Ref. [30]

The 14-bit registers of all pixels are read out serially (parallel readout is technically possible yet most of the hardware read-out options do not support it, this would reduce the read-out time by a factor of 32). Considering that a clock of 40 MHz is being used a serial readout of all the 262 144 14-bit registers takes 92 ms for the four chips. Furthermore, using a frame time of 0.1 s, which was the choice for the experiments discussed in chapter 5, this amounts to a dead-time of 48 %. This was revealed to be a significant disadvantage of the timepix-quad detector.

One important setting in the analog part of the pixel electronics is the IKrum value. This setting defines the discharge rate of the input charge and consequently has a pulse shaping effect. A lower IKrum will cause the charge to be discharged slower and result in a longer pulse. This effect can be beneficiary when measuring the Time over Threshold as an energy proxy but it can also increase the noise if the detector has a significant leakage current.

The detector's pixels can be individually tested by sending pulses of variable voltage to the test input of each pixel cell. This is especially useful to know which pixels are noisy or dead. A common test procedure is to send 100 pulses to each pixel, after which one can identify and mask all the pixels that measured more or less than the number of pulses sent. Test pulses are also a tool to make a rough but very easy and practical energy calibration of the detector. Unfortunately, this requires a special routine in the control software and an update discontinued this possibility.

After testing the pixels and setting the pixel mask, it is necessary to do a pixel equalization. This procedure will set the value of the thrAdj 4-bit in order that each of the pixels has an equivalent energy threshold. To equalize the thrAdj the control software will set it to its minimum value and incrementally increase the global threshold until the software manages to identify the noise level of each of the pixels, the process is then repeated but with thrAdj set to its maximum value. By interpolating between the two scans the thrAdj can be set to a value that ensures that the noise level is equalized over all pixels and

with relation to the global threshold. After equalization, in order to have a measurement free of noise triggers, the global threshold is increased above the noise level, at this point, none of the pixels will trigger on noise.

As seen so far, the control of the detector involves several tasks such as setting digital settings that define the pixel working modes, setting control voltage values that regulate the pulse shape, starting and stopping measurements, and, of course, reading out the data. These jobs are done by proprietary hardware and respective control software. Two widely used readout systems available are the Fitpix [57] and SPIDR [58, 59]. From the output produced by these systems it is up to the user to set up the necessary tools to treat the data and use it according to his/her needs.

In an energy measurement the output from the timepix detector is a ToT value that can be converted to energy with a calibration. The equation that relates the ToT measured by a pixel of the timepix detector and the deposited energy is the surrogate equation shown in Eq.: 2.3.1. As each pixel requires a slightly different calibration, the full quad detector energy calibration consists in finding the best values for the a, b, c, t parameters for each of the 262 144 pixels. In the absence of the possibility of using test pulses for a rough calibration or when in need for optimum energy resolution, the energy calibration of a timepix detector is done best with the use of X-ray fluorescence as described in Ref. [60]. The method consists of measuring x-ray fluorescence lines at several energies and using the distribution shape of the observed ToT values to find the best values for the surrogate function parameters.

$$E(ToT) = a \times ToT + b - \frac{c}{ToT - t} \tag{2.3.1}$$

The energy calibration depends on the chip equalisation and chosen threshold level, which in turn depend on the detector noise. It happens that the noise level can vary in time, due to damage or external electronic noise sources. The change in noise was in fact observed during the use of the timepix-quad detector. After some time, an increase in noisy pixels was observed which led to regular updates of the pixel mask, equalization and lowering of the bias voltage from an initial 80 V to 50 V. The lowest voltage is believed to be at the limit where the whole detector is still fully depleted. The exact cause for this change could not be identified.

The fact that the timepix detector has a small pixel size brings a couple of consequences to the data treatment. One effect is charge sharing, exemplified in Fig. 2.5. This happens because the charge created in the sensor, as it drifts towards the chip contacts, also takes on a lateral Gaussian shaped spread due to the random movement of the charge cloud. The smaller the bias voltage the larger this effect is. Additionally, as the charge spreads over a larger area a more significant part of the deposited charge may be lost if it stays under the trigger threshold or reaches pixels at the edge of the detector. This effect also induces a worsening of the position resolution although for the EC case this is very small compared to other factors.

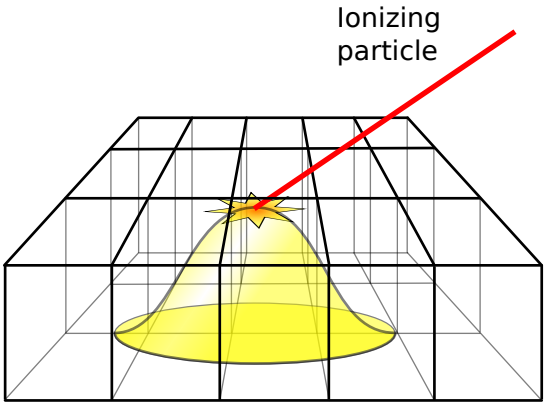

Figure 2.5: Example of charge sharing in a pixel detector. As the cloud of electron-hole pairs created by the incoming particle drifts due to the applied bias, random movement of the charges causes the cloud to spread laterally.

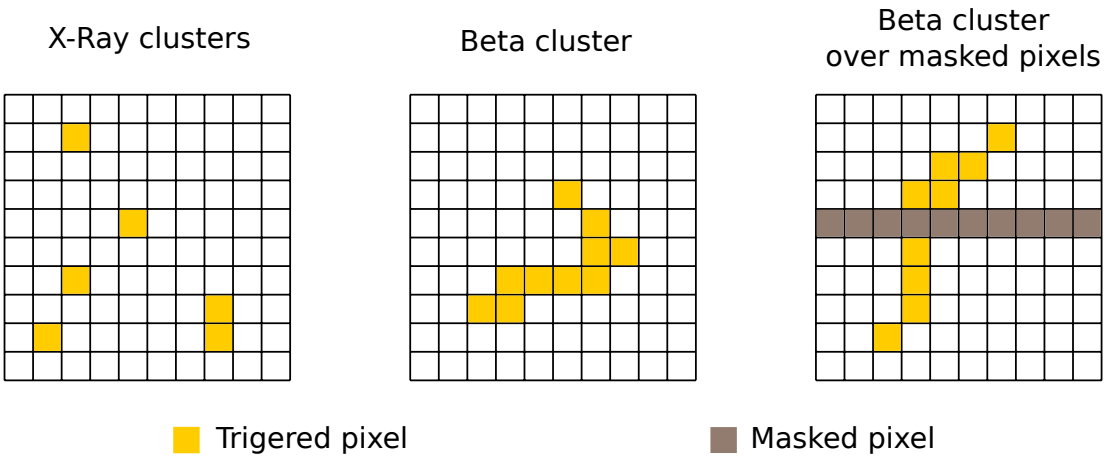

Figure 2.6: Examples of clusters expected in a timepix detector. Clusters from x-rays generally only have one or two pixels. On the other hand, clusters from beta particles can reach a lengthy sequence of pixels due to scattering and creation of secondary electrons inside the sensor. This sequence might not be continuous if energy is deposited in a masked pixel or if deposited energy stays below threshold.

Electron scattering inside the sensor is another effect noticeable due to the small pixel size. While x-rays deposit their energy in a localized space of 1-3 pixels, betas can scatter over several pixels (see examples in Fig. 2.6). This effect blurs the position at which the incoming particle reached the detector and requires a clustering algorithm so that each collection of triggered pixels belonging to the same cluster only counts as one hit.

The clustering of pixels triggered by a beta particle can be done in several ways. One rudimentary algorithm, but nonetheless effective, is to scan each triggered pixel in the frame for adjacent pixels that also triggered, add these pixels to the cluster and repeat for each new pixel. This process is then repeated until all triggered pixels in a frame are associated to a cluster. This algorithm can also be modified to mitigate situations where a cluster is divided in two, as described in Fig. 2.6, by scanning not only nearest neighbour pixels but also next-nearest neighbours.

A difficulty when doing clustering is that clusters that are close might be wrongly counted as a single one, causing pile-up. Another is to classify the triggered pixels into clusters as fast as possible. For the latter a possibility is to use an external library that is well optimized. For this, a recommendation is to use a library with the Density-Based Spatial Clustering of Applications with Noise (DBSCAN) algorithm [61], for which several implementations in various programming languages exist. The DBSCAN method searches for elements of a cluster based on the density of events, it has the advantages of being able to find any number of clusters and to allow for discontinuity in the clusters. Furthermore, it can easily be adapted for clustering of timepix3 data that also requires the inclusion of the ToA for clustering.

Once the cluster counting exercise is completed, and a 2D channeling pattern is made with the histogram of the counts, it is then time to use statistical methods for estimating the lattice location of the probe atoms from fitting the results of electron channeling simulations. For this a fitting procedure is explained in chapter 3, but first a general review of statistical inference is necessary.

2.4 Statistical analysis

Statistical inference consists of using a collection of measurements to infer some information about the data, in this specific case, it is to infer lattice site location information from channeling patterns. In this section the statistical concepts that are used in the thesis are introduced in a general way. Later, in chapter 3, these concepts are applied in the formulation of the fitting methods for Emission Channeling (EC) measurements. Most concepts here described are taken from Ref. [62] a book that I highly recommend for learning statistical tools for physicists. Other worth mentioning books on statistical data analysis for physicists are in Ref. [63, 64].

Emission channeling experiments consist in measuring and counting a two dimensional (2D) random variable, (ϑ, ω), resultant from random events that are subject to a 2D angular probability distribution at

which charged particles from radioactive decay are emitted from a single crystal. These counts are organized, by angular direction, into the bins of a 2D histogram to form a channeling pattern. From these data, information about the lattice site locations of the radioactive isotopes is inferred by fitting it with channeling simulations. This provides, as a result, an estimate of the lattice site fractions and their respective confidence range.

Because EC experiments are based on the measurement of random independent events during a given period of time the total number of counts in a channeling pattern is a Poisson variable. Additionally, the same reasoning applies to the number of counts in each bin of the histogram. Consequently, in order to stay within context, this chapter will only focus on the theoretical background needed for fitting data that follow a Poisson distribution and are organized into bins.

A good starting point into these concepts is to know that the outcome distribution of a random variable can be defined by its probability density function (p.d.f.). Consider now a random variable X whose outcome lies in a region of space represented as S. The p.d.f. of X, $f(x)$, defines the relative expectancy of the value of X being in the interval $[x, x + \mathrm{d}x]$, in the following way,

$$\text{Probability that } X \text{ is between } [x, x + \mathrm{d}x] = f(x)\ \mathrm{d}x\,. \tag{2.4.1}$$

Because X is always defined in S, the integral value of the p.d.f. $f(x)$ in the region defined by the possible outcomes is always 1. Therefore,

$$\int_S f(x) = 1\,. \tag{2.4.2}$$

In the case where X is not a single measurement but a sample of N measurements, X is treated as the joint random variable, $[X, \ldots, X_N]$ with p.d.f., $f(x) = f(x_1) \times \ldots \times f(x_N)$.

Often, in an experiment that measures a random variable, there is a theoretical model that describes the experiment but is subject to the values of a number of unknown variables. By tuning these variables, the model can be changed in order to best represent the observations, basically fitting the model to the data. In this description, it is proposed that the model defines the p.d.f. of the random variable being measured. Therefore, the measured value X follows a p.d.f., $f(x)$, that is not fully known. In order to define, $f(x)$, one needs a mathematical procedure to estimate the model parameter values from the observations.

In this process it is a good practice to define the model parameters as the desired outputs of the experiment so that posterior derivation and error propagation are avoided. This usually means that certain model parameters characterize the fundamental physics interest in the experiment. Other parameters, called nuisance parameters, are variables whose values also need to be estimated but for which there is no specific interest in terms of physics.

It is also worth mentioning that it should be the model that is fitted to the data and not the other way around. Directly scaling the data or removing background will affect the assumption that the data is a Poisson random variable and guaranteeing the validity of the results may not be trivial.

The mathematical process used to get an estimation of a model's parameter, θ, from a measured random variable is called an estimator and is represented by the variable with a hat, $\hat{\theta}$. When the estimator is applied to a random variable, $\hat{\theta}[X]$, it acts as a function of a random variable and consequently it is also a random variable itself. Concurrently, the value of the estimator for a given sample with value x, $\hat{\theta}[x]$, is a fixed value which might not be exactly the true value of θ.

Two characteristics that need to be explained about estimators are the concepts of bias and variance.

2.4.1 Bias and variance of estimators

For a good estimator, its expected value should be the true value θ, represented as $E(\hat{\theta}) = \theta$, this means that the estimator is unbiased. When this is not the case the estimator is said to be biased, meaning that the estimated value will deviate from the real one. The bias, b, is defined as,

$$b_{\hat{\theta}} = E(\hat{\theta}) - \theta \,. \tag{2.4.3}$$

When building an estimator one should choose a method that introduces the minimum possible bias. It is also important to remember that there can be other sources of bias besides the chosen estimator, these can come from the theoretical model, sampling methods or assumptions that are made during the analysis. These are referred as systematic errors.

The variance describes how distant the estimated values will be from each other if the estimator would be repeatedly applied to similar samples. It is defined as,

$$\sigma^2_{\hat{\theta}} = E[\hat{\theta}^2] - (E[\hat{\theta}])^2 \quad . \tag{2.4.4}$$

The variance, or its square root the standard deviation σ, has an important role in the reporting of the confidence intervals of an estimated value. Usually a value $\hat{\theta}[X]$ and its standard error are reported as $\theta_{obs} \pm \sigma_{\hat{\theta}}$, meaning that for repeated experiments the resulting value will be 68.3% of the time within the interval limits, as for most cases a Gaussian distribution of the results is expected. Generally, a good way for reducing the variance in a counting experiment is to increase the sample size.

A robust way of calculating the variance of an estimator is to use the Monte Carlo method to simulate repeated experiments and use the resulting distribution of the estimated values to calculate the variance by applying eq.: 2.4.4. As this method is complex to set up and computationally expensive a simpler method is to use the Cramér-Rao lower limit which will be explained in section 2.4.2.

Estimators can be of all sorts. In the simplest case, a mean estimator of a population is the mean of the sample. When the idea is to fit the data, the estimator is generally the minimization of a cost function.

2.4.2 Chi-square and likelihood estimators

Chi-square minimization and maximum likelihood are two standard data fitting methods used for building estimators of model parameters. Here the general methods of building parameter estimators will be described using each of these two methods to define a cost function and, with it, fit binned data. Later, methods for calculating the variance based on these estimators will also be introduced.

Consider a general case of a counting experiment. The experiment is designed to get several measurements of X, $\{X_1, X_2, ..., X_{N_{cts}}\}$, where the total number of measurements, N_{cts}, is a Poisson random variable. The values are then organized in a set of N_{bins} bins of interval $[x_i, x_i + \Delta x]$, with n_i being the number of counts in bin i and $\boldsymbol{n}$ the set composed of the number of counts per bin $\boldsymbol{n} = \{n_1, ..., n_{N_{bins}}\}$.

The model by which the data is fitted is given by the p.d.f., $f(x, \theta)$, where $\theta = \{\theta_1, ..., \theta_m\}$ are the parameter values to be determined. From the model p.d.f., the expected probability of a measurement of X being in the histogram bin i, represented by $p_i(\theta)$, is given by the integral,

$$p_i(\theta) = \int_{x_i}^{x_i+\Delta x} f(x, \theta)\ \mathrm{d}x\,. \tag{2.4.5}$$

Similarly, the expected number of counts in bin i, represented by $\upsilon_i(\theta)$, is,

$$\upsilon_i(\theta) = N_{cts} \int_{x_i}^{x_i+\Delta x} f(x, \theta)\ \mathrm{d}x\,. \tag{2.4.6}$$

Building a maximum likelihood estimator

The process of fitting a model to a data set by maximizing the likelihood function, finds the parameter values that maximize the probability that the distribution of the measured data is explained by the model's resulting p.d.f..

The likelihood function, calculates the joint probability of a sample distribution, equal to the measured data, occurring from the model p.d.f., $f(x, \theta)$. Considering that the probability of having n_i results in bin i is $p_i(\theta)^{n_i}$ the likelihood function for the whole sample is,

$$L(\boldsymbol{n}|\theta) = \frac{N_{cts}!}{n_1! \ldots n_{N_{bins}}!} \prod_{i=1}^{N_{bins}} p_i(\theta)^{n_i}\,. \tag{2.4.7}$$

The numerical calculations of the long product of probabilities can result in a very small number whose numerical accuracy can be hard to ensure. For this reason the products are converted into sums by instead calculating the log likelihood. Additionally, as optimization algorithms are usually constructed

to find minima, it is a common choice to use the negative log likelihood as the cost function, which is then defined as,

$$-LL(\boldsymbol{n}|\theta) = -\sum_{i}^{N_{bins}} n_i \log(p_i(\theta))\,. \tag{2.4.8}$$

Note that the additive terms that do not depend on the function values are dropped, as they would only change the $-LL$ by a constant.

An estimator that is built from the likelihood function tries to find the value of θ that minimizes the negative log likelihood, therefore,

$$\hat{\theta}_{ML} = min_{\theta}(-LL(\boldsymbol{n}|\theta))\,. \tag{2.4.9}$$

One important characteristic of the likelihood estimators is that they are unbiased, even when the number of counts per bin is small. Moreover, in the special case of having a bin with zero counts the exponential term in eq.: 2.4.7, $p_i(\theta)^{n_i}$, would be 1 and would not affect the cost function value, nor the parameter estimation. As opposed to the same situation in the case of a chi-square estimator, yet, as will be seen next, there are other advantages.

Building a chi-square estimator

Chi-square minimization fits serve the same purpose as maximum likelihood fits, yet the underlying principle is different. In this case the model parameters are optimized so that the differences between the model function and the measured data histogram are minimized.

Chi-square estimators make use of the chi-square statistic whose resulting value is a random variable that follows a chi-square distribution. The chi-square distribution is one of the most used probability distributions and has as characteristics the facts that it is fully defined by the number of degrees of freedom (n.d.f.), k, the distribution tends to a normal distribution for large k, its mean is equal to k and variance equal to $2k$. The fact that it is expected that the resulting chi-square value follows a chi-square distribution turns out to be a great advantage of the method, as it then becomes possible, based on the n.d.f., to know how likely the obtained value is. Contrarily to the maximum likelihood method this allows for an evaluation of the goodness of fit (g.o.f.).

A chi-square distribution with k degrees of freedom is the result from the sum of the squares of k independent standard normal random variables. A standard normal random variable is characterized as having a p.d.f. that follows a Gaussian distribution with mean 0 and standard deviation 1. Therefore, by shaping the experimentally measured random variables into standard normal variables it is possible to build a chi-square statistic from the data.

Considering that, for large samples, the Poisson distribution which represents the number of events in a bin n_i is approximately a normal random variable with mean equal to υ_i (the expected number of counts) and variance also equal to υ_i, the following equation will approximate the distribution of a single data point to a standard normal,

$$\frac{(n_i - \upsilon_i(\theta))^2}{\upsilon_i(\theta)} \,. \tag{2.4.10}$$

Summing over all bins, as follows,

$$\chi^2_{P(k)}(\boldsymbol{n}, \theta) = \sum_{i=i}^{N_{bins}} \frac{(n_i - \upsilon_i(\theta))^2}{\upsilon_i(\theta)} \,, \tag{2.4.11}$$

will then result in a chi-square distribution with k degrees of freedom, where $k = N_{bins}$.

An intuitive way of looking at the chi-square fit method is to consider that for each data point, the fraction's numerator is a measure of the distance between the measurement and the model. Additionally, the denominator, which is the variance of the data point, is a measure of how expectable it is to have a large distance in the numerator. The model is optimized by minimizing the chi-square, this will reduce the distance in the nominator weighted by is variance. The estimator for the model parameters is built by finding the value of θ that minimizes the chi-square, as,

$$\hat{\theta}_{\chi^2_P} = min_\theta(\chi^2_P(\boldsymbol{n}, \theta)) \,. \tag{2.4.12}$$

Here, for g.o.f. purposes, the n.d.f. needs to be corrected for the number of independent parameters, m, in the model. Therefore, $k = N_{bins} - m$.

Unlike estimators built with the likelihood method, the chi-square is biased. A model optimized by chi-square minimization will not match the total number of counts from the experiment. However, chi-square estimators are asymptotically unbiased, meaning that when the number of counts per bin is large the estimators are unbiased.

The chi-square statistic presented here is called the Pearson chi-square and has the characteristic of having the variance defined as the expected number of counts in each bin, υ_i. Alternatively, the Neyman chi-square uses as variance the number of counts in the bin, n_i. It is often used by researchers despite having been repeatedly reported as giving worse results and having higher bias, especially when working with bins that have a low number of counts. For this reason the Neyman chi-square should be avoided and the Person chi-square used instead.

One of the main advantages of the chi-square method is that the chi-square value can be used to

evaluate the g.o.f.. The g.o.f. is a method to check how probable it is that the measurements can be described by the fitted model's p.d.f.. In case the probability, given by the g.o.f., is too low, then it shows that the model does not accurately represent the measurement. This method is important when, for example, someone is trying to propose a new model for the description of a phenomenon.

The g.o.f. is calculated in terms of a P-value. In the chi-square case it is defined as the probability, given the fitted model p.d.f., of measuring a data set that generates the same chi-square value or a more extreme one. In the case of the P-value probability being lower than 0.05 or 0.01, depending on a predefined choice, it is said that the model does not fully represent the data. One should keep in mind that this is a purely mathematical test used to discard models that statistically differ from the experiment, despite its merit, it is also a valid argument that models that would be rejected by a g.o.f. test can still prove to be useful.

When using the chi-square to evaluate the g.o.f., it is a recurrent practice to use the so called reduced chi-square which is the chi-square divided by the n.d.f.. This approach should be avoided as, depending on the n.d.f., the same ratio can give very different P-values. For this reason, even if the g.o.f. is not evaluated, the chi-square should always be reported in absolute values and together with the n.d.f., not as the reduced ratio.

Estimators standard error

When reporting a result from an experiment it is fundamental to include its error. The variance comes into play in calculating the statistical error as it gives the information about how much the result could change in case the experiment would be repeated in the exact same conditions.

As stated earlier, doing a Monte Carlo simulation to calculate the variance is difficult. A more practical method is to use the Cramér-Rao lower bound. The bound calculation uses the second derivatives of the log likelihood at the estimated best values of the parameters. Intuitively, this can be thought as a large variance being caused by a wider log likelihood peak, as in this case the peak maximum is less accurately defined. In a more technical description, the Cramér-Rao lower bound states that the variance lower bound is given by the inverse of the Fisher information matrix at the best fit point. For unbiased estimators the bound says that the variance is equal or larger than,

$$\sigma^2_{\hat{\theta}_i} \geqslant [\mathcal{I}(\theta)]^{-1}_{ii} \,. \tag{2.4.13}$$

Where the Fisher information matrix, $\mathcal{I}$, is calculated from the second derivatives of the log likelihood function as,

$$[\mathcal{I}(\theta)]_{ij} = E\left[\frac{\delta}{\delta\theta_i\delta\theta_j}\left(-\log L(\boldsymbol{n}|\theta)\right)\right]_{\theta_{obs}} . \tag{2.4.14}$$

Recalling that the standard error of the estimator $\hat{\theta}_i$ is the square root of its variance. Using equation 2.4.13 and assuming that the variance is equal to its lower bound, it can then be calculated as,

$$\sigma_{\hat{\theta}_i} = \frac{1}{\sqrt{[\mathcal{I}(\theta)]_{ii}}} . \tag{2.4.15}$$

Often fitting algorithms provide the Hessian matrix of second derivatives, it is then useful to use the Hessian matrix as the expected value of the Fisher information matrix. Considering that the Hessian matrix of the log likelihood, evaluated at estimated parameter values, is,

$$[H(\boldsymbol{n}|\theta)]_{ij} = \left[\frac{\delta}{\delta\theta_i\delta\theta_j}\left(-\log L(\boldsymbol{n}|\theta)\right)\right]_{\theta_{obs}} . \tag{2.4.16}$$

Then, the standard error is calculated as,

$$\sigma_{\hat{\theta}_i} = \frac{1}{\sqrt{[H(\boldsymbol{n}|\theta)]_{ii}}} \tag{2.4.17}$$

Despite the Cramér-Rao lower bound being described from the likelihood function it can also be used in a chi-square estimate by scaling the Hessian by $1/2$. The standard error of a chi-square estimate is then calculated as,

$$\sigma_{\hat{\theta}_i} = \frac{1}{\sqrt{\frac{1}{2}[H(\boldsymbol{n}|\theta)]_{ii}}} \tag{2.4.18}$$

Another method of calculating the variance that is useful when the function is not differentiable is the graphical method. In this method the one sigma error bars are given by changing the θ value, from its best fit value, until the value of the log likelihood function changes by $1/2$ or the chi-square function changes by 1. This method is also appropriate when the errors are asymmetric, and given by $+\delta_+, -\delta_-$ instead of $\pm\sigma$. Then the expressions apply,

$$LL(\theta_{obs}) - LL(\theta_{obs} - \delta_-) = LL(\theta_{obs}) - LL(\theta_{obs} + \delta_+) = 1/2 , \tag{2.4.19}$$

and,

$$\chi^2_P(\theta_{obs}) - \chi^2_P(\theta_{obs} - \delta_-) = \chi^2_P(\theta_{obs}) - \chi^2_P(\theta_{obs} + \delta_+) = 1 . \tag{2.4.20}$$

3

Data Analysis: Methodology Review and Improvements

This chapter reviews some of the processes in the data analysis procedure that were subject to deeper analysis during the thesis.

The first section of the chapter is about the topic of the angular resolution of the measurement, how it can be calculated and how it is expected to influence channeling pattern measurements. This section dives into Fourier transforms and uses the frequency spectrum as a measure of information to identify the channeling patterns that are more affected by the measurement resolution.

The second section is about the improved fitting procedure that is implemented in the PyFDD software. This procedure is based on the previous software, FDD, with the addition that PyFDD uses a new approach in several of the analysis steps in order to avoid potential bias and improve analysis results.

The last section is about background, both from gammas and from scattered betas. It highlights the importance of keeping a low level of background and shows the updates made to the GEANT4 [65] Monte Carlo (MC) program for simulating electron scattering in both the pad and the timepix setups.

3.1 Considerations on the angular resolution

The topic of the angular resolution has been part of this thesis work since the start due to the fact that the new timepix detector was seen as a breakthrough for improving the angular resolution and thus provide a measurement with a very fine angular step.

A low angular resolution will in most cases cause a blurring of the channeling pattern, although in the case of the pad detector it also causes pixelisation due to large pixel dimensions. The lower quality of experimental patterns caused by a bad angular resolution of the setup may result in loss of information which may worsen or induce mistakes in the analysis. Although information lost in the pattern blurring can not be recovered, some mistakes in the analysis can be avoided if the simulation model includes a good estimation of the measurement resolution.

The calculations of the angular resolution are based on geometrical factors defined by the setup and detectors in use which are considered to be independent of the experiment. However, when taking into account that some simplifications used in the calculations may be missing second order effects or that the sample quality may also have a blurring effect similar to the one caused by the geometrical factors, it is then relevant to know if the resolution of the measurement can be retrieved from the analysis of channeling patterns by means of a fit.

In the scope of the improvement of the detector position resolution as an enhancer of Emission Channeling (EC) results, another question that should be asked is to what extent the angular resolution should be improved in order to attain the desired objectives in lattice locations experiments. The answer to this can be weighted with the knowledge of how much information can be retrieved from a channeling yield distribution when measured with two competing angular resolution setups.

These questions will here forth be discussed.

3.1.1 Angular resolution of the setup

The angular resolution is a product of the setup and can be approximately calculated by geometrical factors. The factors to take into account are the beam spot size, the detector position resolution and the distance between the detector and the sample. In the calculations here presented the fact that some simplifications are made, makes it wise to assume that what is calculated might deviate from reality by some margin.

One of the first simplifications made here is to assume that all the contributions to the angular resolutions have a two dimensional (2D) Gaussian effect and that it is isotropic, meaning that the effect is the same in all directions. This effect on the channeling patterns can then be modelled by a Gaussian smoothing of simulated 2D yields. This generalization has the advantage that a Gaussian smoothing function can be fully defined by its 1-dimensionally projected standard deviation, σ. Additionally it

now becomes very easy to add contributions from different parts of the setup due to the mathematical property that the convolution of two Gaussian functions is also Gaussian. The Gaussian function that accounts for all the effects has a standard deviation (SD) that can be simply calculated from the original contributions, with the total SD defined as, $\sigma^2 = \sigma_1^2 + \sigma_2^2$. Therefore, the resulting position resolution SD from the detector and beam spot size contributions can be defined as,

$$\sigma = \sqrt{\sigma_{detector}^2 + \sigma_{beam\ spot}^2}\,. \tag{3.1.1}$$

Here, both standard deviations are assumed to be isotropic. While this is always the case for the detector, in the case of the beam spot it can deviate significantly from reality as the ion beam is projected onto a tilted sample. In fact, it is a standard procedure to avoid ion channeling during implantations, that the implantation beam would have tilted incidence in relation to the surface normal of the crystal, usually by 17°. This causes a change in the shape of the beam spot, which for a 17° tilt extends it in one dimension by 4.4 %. For online measurement the tilt angle, and consequent stretching of the beam spot, can be much larger as the implantation angle is dependent on the axis facing the detector. Additionally, the sideways view of the sample from the detector perspective may contribute to the beam spot having an elliptic geometry.

By taking into account the distance from the sample to the detector d, the effect from equation 3.1.1 can be expressed in terms of angular resolution, in degrees, as

$$\sigma = \arctan\left(\frac{\sqrt{\sigma_{detector}^2 + \sigma_{beam\ spot}^2}}{d}\right)\,. \tag{3.1.2}$$

The distance d depends of the setup configuration and can be looked up on table 3.1 which summarizes the distances for the different detector setups.

extension\detector	timepix-quad	timepix3	pad
without extension	316 mm	307 mm	320 mm
with extension	596 mm	589 mm	602 mm

Table 3.1: Distances from the sample to the detector with different configurations and detectors for the EC-SLI setup at ISOLDE.

The position SDs for the pad pixels and the circular beam spot can be calculated from their second moment normalized by their area. Therefore, considering the beam spot to be a 1.0 mm diameter circle, its SD is calculated as,

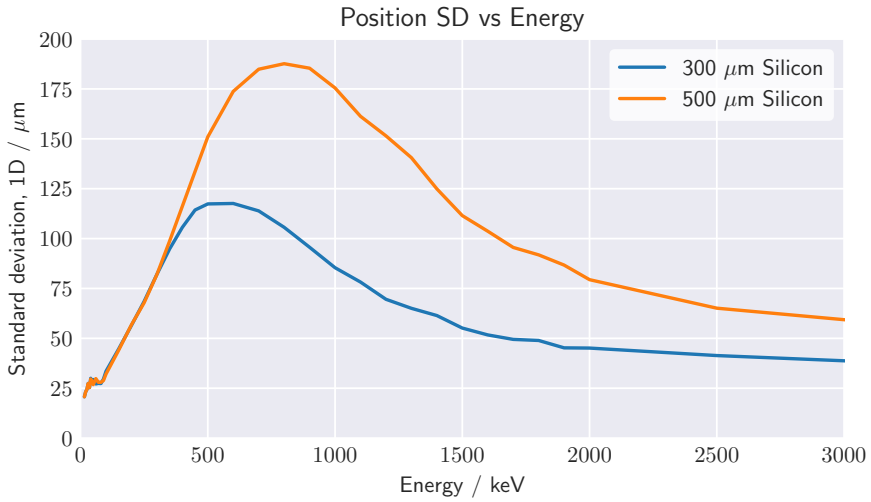

Figure 3.1: The 1-dimensionally projected standard deviation (SD) of the detection position for an electron point source on a timepix detector with two different sensor thicknesses. The values were obtained with GEANT4 simulations of a beam with the size of a pixel and defining the hit pixel as the centroid of activated pixels in a cluster. Depending on the energy distribution of the measured particles the position resolution will vary.

$$\sigma_{beam\ spot} = \frac{1}{2} \times \frac{1.0}{2} = 0.25\,. \qquad [\mathrm{mm}] \tag{3.1.3}$$

Similarly, the position resolution of the pad detector is calculated from the second moment of a square with length equal to the pixel size of 1.3 mm, resulting in,

$$\sigma_{pad\ detector} = \sqrt{\frac{1}{12}} \times 1.3 = 0.375\,. \qquad [\mathrm{mm}] \tag{3.1.4}$$

For the timepix detector the position resolution depends on the electron energy as it influences how far the electrons scatter inside the sensor. For this reason the same method can not be used, instead the position resolution is obtained from GEANT4 [65] Monte Carlo (MC) simulations. These were made by simulating a beam being shot to a pixelized timepix with 300 µm and another with 500 µm Si sensor. The beam considered has the dimension of a pixel in order to avoid effects originating from the location of the beam in relation to the pixel matrix. The simulation then makes a distribution of the distance from the first hit pixel to the centroid of activated pixels, from which the SD is extracted. The values of the standard deviation resulting from the simulation can be seen in Fig. 3.1.

As seen from the simulation results, the highest values for the SD correspond to electrons with energy of 600 keV for a 300 µm sensor with $\sigma_{detector} \approx 110$ µm and 900 keV for a 500 µm sensor with $\sigma_{detector} \approx 175$ µm. As each isotope has different beta emission energy distributions an approximate

Geometrically calculated values for the setup angular resolution		
Pixel size	Detector SD [mm]	Setup SD with 1 mm beam spot [°]
timepix 55 µm, $d = 316$ mm	0.11	0.050
timepix 2x2	0.11	0.050
timepix 4x4	0.13	0.051†
timepix 8x8	0.17	0.055†
timepix 16x16	0.28	0.068†
pad 1.3 mm, $d = 320$ mm	0.375	0.081†
pad 1.3 mm, $d = 602$ mm	0.375	0.043

†Do not use in PyFDD calculations, use sub-pixels instead.

Table 3.2: Table of the setup angular resolution as it changes with the pixel size. In some cases it is useful to add pixels when using timepix, to increase counts per pixel or speed up fitting. This table shows how the angular resolution worsens as pixels are added together. It also shows the values for the pad detector at 320 mm and 602 mm.

value of $\sigma_{detector} \approx 110$ µm is chosen as simplification. Consequently,

$$\sigma_{timepix} = 110\,\mu\text{m} \tag{3.1.5}$$

From equation 3.1.2 and the calculated detector position SD, the resulting setup angular resolutions are displayed in table 3.2. The table also includes resolutions when timepix pixels are added together. This is done by convolving the second moment of the added pixel size with the timepix resolution obtained with the full pixel mesh.

In order to improve the resolution of the setup the use of a smaller beam collimator of 0.4 mm diameter was tested. Unfortunately, as the ion beam width could not be improved further by the beam line quadrupoles, the beam loss in the collimator was too significant to be practical. Nonetheless a small test was done with ^{43}K in GaN and is described in section 5.1

The result of the timepix resolution from eq. 3.1.5 was calculated using as the cluster hit pixel the centroid of activated pixels, which is the method used throughout this thesis. Nonetheless, there are other interesting options for estimating the hit pixel from the cluster data if the information about the charge collected in each pixel is also used. Figure 3.2 compares the obtained detector position resolution from different hit pixel determination methods. These are: the pixel with maximum deposited charge; the pixel that is located at the centroid of all activated pixels; the pixel that is located at the centroid of the deposited charge. From these results it is clear that using the charge centroid is the most accurate method, however it is uncertain how the detector noise and energy resolution from a real world measurement could alter this. Additionally, the complexity of making a good per-pixel detector energy calibration and actualizing it over time, made that it was chosen to only use activated pixel information and accept a small loss in position resolution.

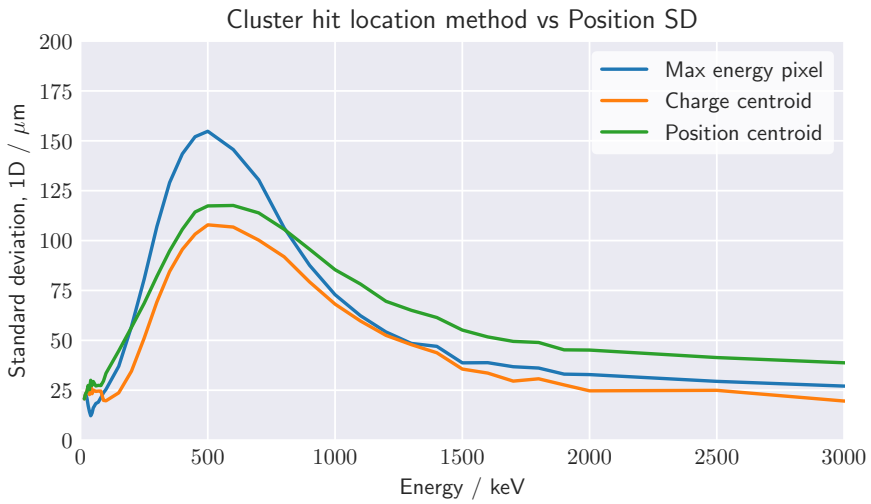

Figure 3.2: The 1-dimensionally projected standard deviation (SD) of the detection position for an electron point source on a timepix detector with respect to different methods for determining the cluster hit pixel. Similarly to Fig. 3.1, the values were obtained with GEANT4 simulations. Although the charge centroid method produces the best position resolution it is also harder to implement than position centroid method.

Getting the resolution from fitting the data

As the value for the resolution, although it can be relatively well approximated from the geometrical factor, has some uncertainties associated due to the used approximations and possible sample effects, one might ask whether the angular SD value could be extracted from the data during a fit procedure.

This approach is hindered by the following considerations. The angular resolution of the setup influences the width of measured emission channeling effects. Since the width is also subject to change by other factors, e.g. displacement of probe atoms from ideal lattice sites, probe atom depth profile, root mean square (rms) displacement of host atoms, sample mosaicity, the fitted value for the angular resolution will to some extent be correlated with these other parameters, so that in general it cannot easily be derived from the measured data.

On the other hand, there exist experimental conditions when one has specific reasons to expect a deviation from the calculated angular SD values. For example, if the beam spot is stretched by a large implantation angle or some mosaicity [66] in the crystal can be expected, then the real SD will be larger than what is expected from the setup angular resolution. For such cases the resolution SD value can be optimized by the fit as the errors introduced by the considerations highlighted in the previous paragraph will be smaller than the use of a SD value solely based on geometrical factors.

3.1.2 Losses of detail due to low angular resolution

Having beforehand knowledge of how much degradation of a channeling pattern measurement is caused by a limited angular resolution is a complicated task yet it has the possibility to give insightful information in the preparation of experiments. This section is an attempt to do just that in a study solely based on simulated channeling data that provides intuitive and general information on which crystallographic axes and which isotopes need better angular resolution. For a quantitative evaluation of the effect of the resolution in a specific determination of a lattice site occupancy, MC methods should be used instead.

Before starting, a quick indication of the necessity for better angular resolution can be taken from the Lindhard critical angles as calculated in table 3.3. The decreasing critical angle with higher energies indicates that better angular resolution is necessary to measure the increasing sharpness of the axial channeling effect.

Isotope	Mean beta energy	Lindhard critical angle for $[0\,0\,0\,1]$
^{43}K	309 keV	1.05°
^{89}Sr	586 keV	0.76°
^{27}Mg	703 keV	0.69°
^{11}Be	4652 keV	0.27°

Table 3.3: The calculated Lindhard critical angle in the $[0\,0\,0\,1]$ direction for a selection of isotopes in GaN.

Considering that a low resolution causes the smoothing of a channeling pattern and that this has the effect of blurring sharp details, it then becomes interesting to quantify the amount of sharp details that can potentially be lost due to resolution. This approach can give a sense of how well the full channeling pattern is detected.

A good way to work with this kind of information in a 2D pattern is through the spatial frequency intensity spectrum of the channeling patterns. By switching the representation of a simulated channeling pattern from the real space to the frequency space and extracting from it its frequency intensity spectrum one can quantify the amount of details and classify them according to their sharpness. With this transformation the amount of sharpness is represented by a frequency power.

Continuing in the frequency intensity spectrum, a good way to represent the effect of the detector resolution is to consider it as a low pass filter. In this line of thought, the integral intensity of the frequencies that are above the filter limit will show how much of the pattern is lost due to the poor resolution of the measurement. This does not necessarily mean that a pattern can no longer be identified but that for it one must rely on a smaller set of features.

An additional possibility when visualizing frequency spectra is to consider the effect of random noise.

While the frequency limit is demonstrated by a vertical cut for which higher frequencies are not measured, the noise is represented by a horizontal line for which features under it can not be distinguished from noise. This happens, as a flat noise in the real space will also be a flat noise in the frequency spectrum. This effect is reduced with the increase of the number of counts in a pattern, effectively increasing the available information and possibly balancing some of the losses from the low resolution.

In order to calculate the frequency detection limit of the detectors two concepts are needed. The Nyquist frequency and the Gaussian low pass filter.

The frequency limit for the pad detector is due to its large pixel size and is given by the Nyquist frequency. The Nyquist frequency defines the highest possible frequency to be measured given the sampling rate, defined here by the angular step between pixels. The Nyquist limit for the pad is calculated as,

$$f_{pad} = \frac{1}{2 \times sample\ rate} = 2.11\,, \qquad [1/\mathrm{degree}] \tag{3.1.6}$$

where the sample rate is given by,

$$sample\ rate = \arctan\left(\frac{pixel\ size}{distance}\right)\,. \qquad [\mathrm{degree}] \tag{3.1.7}$$

Frequencies that are above the Nyquist limit can cause aliasing effects on the measured pattern. This happens when the yield changes sharply inside a pixel and originates artefacts in the pixelated pattern (see Fig. 5.21).

For the timepix detector, the frequency limit is calculated from the representation of the Gaussian smoothing in the frequency space as a low pass filter. The filter function is obtained from the Fourier transform of the Gaussian convolution function which is also a Gaussian. The Gaussian filter function in the frequency space will have its SD, σ_F, defined as,

$$\sigma_F = \frac{1}{\sqrt{2 \times \pi^2 \times \sigma_R}}\,, \tag{3.1.8}$$

where σ_R is the SD of the Gaussian in the real space.

The low pass filter is then defined, for positive frequencies, as Gaussian function centred in zero with σ_F. The frequency limit, which is not a sharp step function as the Nyquist limit, can be defined as the frequency point at which the intensity is reduced by half. This is given by half of the full width at half maximum of the Gaussian, calculated as,

$$f_{timepix} = \frac{1}{2} \times 2.3548 \times \sigma_F = 3.68 \qquad [1/\mathrm{degree}] \tag{3.1.9}$$

Keep in mind that the different ways of assessing the two detectors' frequency limits are not completely comparable as the Nyquist frequency is a hard limit above which no frequencies are measured while for the low pass filter frequencies are still measured but with a lower intensity.

Fig. 3.3 shows the effect that the angular resolution has on the ability to fully measure the details of $[0\,0\,0\,1]$ patterns for a few selected isotopes in GaN. These plots are obtained by means of a 2D Fourier transform of simulated channeling patterns and by subsequently indicating in the obtained intensity spectrum the frequency limits calculated for the pad and timepix detectors. Furthermore, by comparing the area of the detectable frequency intensity to the left of the frequency limit with the undetectable intensity to the right of the limit, isotopes that require better resolutions can be identified.

This analysis uses the average of the frequency intensity spectrum over all sites in $[0\,0\,0\,1]$ simulation libraries for a specific isotope in GaN. It does not compare patterns from any particular combination of sites. It is therefore only useful to assess the required angular resolution for measuring channeling patterns in a general way. For all the analysed channeling simulations, the $[0\,0\,0\,1]$ axis showed higher requirements in angular resolution than the other axes.

From Fig. 3.3 plots, the first thing to notice is that frequencies are higher for high emission energies, hence requiring better resolutions. The frequency spectra for both the ^{43}K and ^{89}Sr show that both detectors can measure the patterns with minor losses. For ^{27}Mg the losses from a pad detector measurement are more significant (noticeable from the lower peak intensity value at low frequencies) making high frequencies more relevant and the use of the timepix detector slightly more adequate. For ^{11}Be the energies are much higher and the negative impact from a low resolution measurement as well. Consequently, for this isotope high angular resolution measurements should be used. While this was realized in recent experiments performed with ^{11}Be using a pad detector with high-resolution geometry, the larger distance from detector to sample of $d = 602$ mm makes exact orientation of the sample considerably more challenging. In any case, use of the timepix, either in normal or high-resolution geometry, should be beneficial for this isotope.

3.2 Fitting the experimental data

The introduction of the timepix-quad detector has been a fundamental motive for the review of the data analysis methods and development of a new fitting software, PyFDD (see also section 4.3). Firstly, due to the larger pixel density, the counts per pixel are reduced to a point where the use of the chi-square as a fit method is not adequate. Secondly, in order to attain the objective of comparing the quality of the results between detectors, the evaluation of the improvements from the use of the timepix detector would benefit from a study of the results uncertainty. This could not be achieved with the existent analysis software, FDD, as it does not correctly calculate the statistical uncertainty of fit results. What

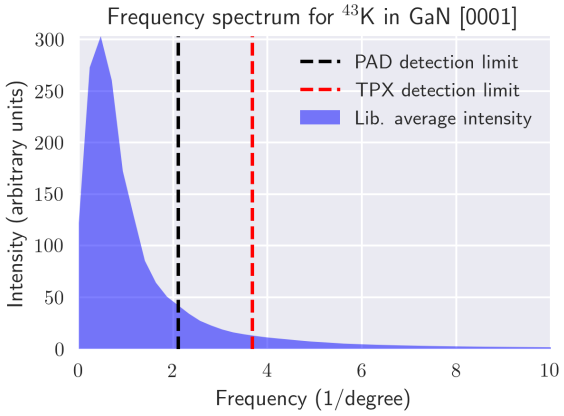

(a) ^{43}K, mean beta energy 309 keV, end point 825 keV

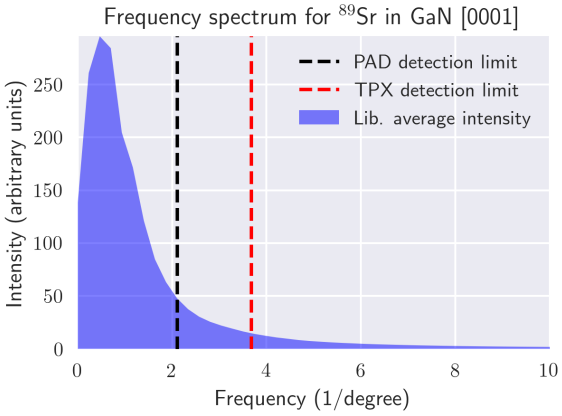

(b) ^{89}Sr, mean beta energy 586 keV, end point 1495 keV

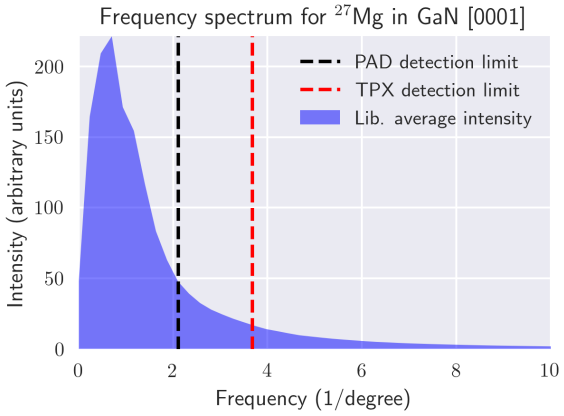

(c) ^{27}Mg, mean beta energy 703 keV, end point 1767 keV

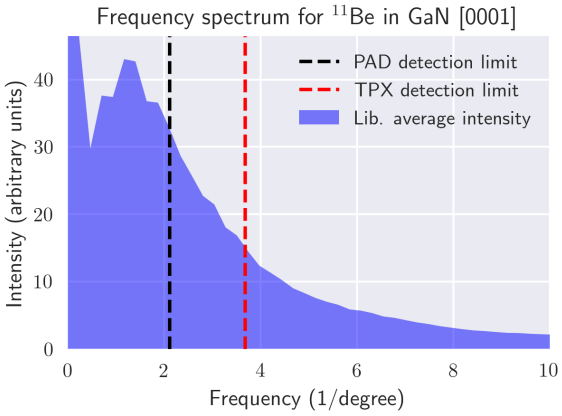

(d) ^{11}Be, mean beta energy 4652 keV, end point 11 506 keV

Figure 3.3: These plots show the intensity of spatial frequencies in emission channeling simulation patterns. Most of the details in channeling patterns are on the relatively low frequencies that are well covered even by the resolution of the pad detector. The patterns from ^{43}K and ^{89}Sr in GaN are examples of isotopes that do not require high angular resolutions. However when the energy of the emitted betas increases, channeling patterns tend to have sharper effects and higher angular resolution is needed to measure the full details of the pattern. This can be seen, for example, in the ^{27}Mg and ^{11}Be intensity spectra.

is more, the review of the fitting methods also revealed some procedural choices in FDD which result in severe limitations of the program when analysing patterns with a small number of counts per pixel. Other procedures that were identified to require changes are the approach how FDD handles the large pixel size of the pad detector, its use of a scaling factor for normalization, and its use of the Neyman chi-square method.

Section 2.4 introduced the statistics background for fitting a model to the repeated measurement of a random variable by chi-square or maximum likelihood optimization. Section 2.2 briefly showed how the emission yields that form a simulated channeling pattern are calculated. This section joins these concepts to build a procedure for the data fitting. The new method was implemented in the PyFDD software, which is proposed as a substitute for the FDD software. In this chapter PyFDD will often be addressed as the name for the improved method and FDD as the name of the previous method.

3.2.1 Pre-fit set up of the data pattern

The data pattern in a channeling experiment is a two dimensional (2D) histogram of counts. Each histogram bin is attributed to a (ϑ, ω) angular position and holds the number of particles that were measured in that direction. One of the first software pieces to be developed and to later be added to the PyFDD software was a module for handling channeling patterns obtained from the timepix detector. In effect, there are several steps that need to be taken before fitting a measured pattern. Most of these steps are common to all kinds of detectors, such as a manual angular orientation, but there are also some steps that are specific to the timepix-quad detector, such as the summing of pixels.

Independently of the detector, a good practice rule when preparing the data pattern is to define a sequence of steps and refrain from changing the order. This helps avoiding common mistakes of mixing files and settings with different coordinates. In the sequence here suggested the first step is to load the pattern matrix and orient it by means of reflections and rotations so that the pattern is displayed as it is seen by the detector.

At this stage the pattern is a 2D matrix of counts where the left, right, up and down are well defined.

After loading, if the detector is a timepix-quad, one needs to ensure that all the pixels are in a regular mesh. Because the central pixels of the detector are larger this is not automatic (see section 2.3). The two central rows and two central columns of pixels have a real width of 3 pixels, therefore to make the mesh regular 2 extra pixel rows and 2 extra columns need to be added in in the center of the detector. The result is a matrix of 516×516 pixels.

The next step is to use the geometrical information of the setup, i.e. pixel size and distance from the detector to the sample, to calibrate the angular range of the detector and define the angular locations of each pixel.

After that it is necessary to mask bad pixels. If the detector has just a few pixels this can be done

by hand, commonly the case when working with the pad detector, on the other hand for large pixel arrays being able to load the pixel mask matrix as a file from the detector readout software is necessary. Furthermore, and especially for the timepix-quad detector, there are additional pixels that need to be masked, some of which are due to how the hit position is defined during clustering, as incomplete clusters connected to masked pixels inflate counts in healthy pixels that neighbour masked pixels. Hence, an advised practice is to expand the mask, obtained from the readout software, to also include every pixel at a distance of 2 from a masked pixel. Pixels at the edge of the detector also need to be masked as these are often noisy, in the pad the edge pixels are trimmed out of the pattern and in the timepix the external four rows and columns are trimmed at the edges. At last, the timepix central larger pixels, as well as their neighbours and the extra empty rows that were added earlier all need to be masked too. In brief, all the pixels that produce clear artefacts in their counts need to be excluded from the analysis. This process needs to be done with extra care as it is a wrong belief that bad pixels can be diluted by the large volume of healthy pixels.

At this point it is necessary to make the decision on how many pixels to combine into one histogram bin. In detectors with large pixels one should simply use each pixel as a bin, whereas for detectors such as the timepix one can choose to add pixels together into larger bins with more counts. The first approach prioritizes angular resolution, while the second prioritizes higher counts per bin to enable the use of the chi-square statistic. When adding pixels together it is important to remember that as large bins that include a masked pixel are also masked this can lead to a reduction in the total counts. Moreover, in order to keep the regularity of the bin mesh, additional pixels at the edges of the detector or near the central rows can be masked.

Once the histogram is built and ready to be visualized, it can be oriented. The orientation is a user input of what is perceived as the center of the axial channeling effect and the angular orientation of a major channeling plane. The orientation is later used as starting point for the optimization and helps avoiding the minimization ending in a local minimum where, for example, a secondary plane is mistaken by a major plane.

The final step when using PyFDD is to set a valid fit range. Because many-beam simulations are generally done with a limited angular range of $\pm 3°$ around the channeling axis, in measurements where the axis is not well centred in the detector some histogram bins may lie outside of the simulated range. Furthermore, during the fit optimization before the position of the channeling axis is known precisely, peripheral bins may lie outside of the simulation range. Owing to the definitions of the chi-square and likelihood cost functions used in PyFDD, it is necessary that the total number of bins in a fit remains constant at all times and that there is always a valid simulation value for each bin. The process to ensure these conditions is to mask peripheral bins that are at an angular distance above $\approx 2.7°$) from the center of axis channel. In contrast, as in FDD the number of bins is not constant during the fit this is not

a requirement.

When using FDD, the final step in preparing the data pattern is to estimate the random level (see 2.2) and scale the measured counts accordingly. First, the random level is estimated by selecting the areas of the measurement that do not have any strong channeling effects and by calculating the average number of counts in these areas. Then the counts in each bin of the whole pattern are divided by the random level. This results in an experimental pattern whose bin values are real numbers close to 1 (approximately in the range 0.5-2), i.e. similar to the normalized yields in the simulated patterns. On the other hand, PyFDD does not scale the count values with the random level for the fit, meaning that counts are fitted instead of channeling yields. The equivalent to the scaling factor in PyFDD is the total number of counts in the pattern which dispenses user input.

Now that the data pattern is calibrated, oriented and pixels are properly masked, it is time to try to find the experimental conditions that lead to the distribution of counts present in its 2D histogram by fitting it with channeling simulations.

3.2.2 Data fitting and parameter estimation

In section 2.4 the basics of parameter estimation were presented. There, it was shown that considering a function that represents the probability density function (p.d.f.) of a measurement, all but for a few undefined parameter values, then, the most likely values of the function parameters are those that minimize either the negative log likelihood 2.4.9 or the chi-square 2.4.12. This section shows how to build the p.d.f., from the many-beam simulation yields, in order to fit the histogram defined in the previous section with the PyFDD method.

The general idea in an Emission Channeling (EC) fit is to find the distribution of occupied crystal lattice sites, present in a broad library of simulations, that most accurately represent the experiment. This is in practice a two step procedure that is repeated with different combinations of lattice sites until the best solution is found; the first step is to choose which sites to test and then the second step is to estimate their respective occupancy fractions by means of a fit. The selection of sites to fit is usually a combination of 1 to 3 sites. The process to find the best solution consists of comparing the tested site combinations by means of their cost function minima after fit, then choosing the site combination that produces a lower cost function and is in agreement with the measurements of other axes and prior knowledge about the sample.

Notice that the process of estimating site fractions does not imply estimating the number of measured particles that have their origin in a specific site. The reason being that each site produces a different total yield pattern in the detector. This point is important as if, in a misleading path, one would consider to fit the number of particles originating from each site, a p.d.f. for each site would be required together with significant changes to the fit process.

Each site included in the analysis contributes with a 2D yield pattern whose intensity is directly scaled with its respective occupancy fraction. As described in section 2.2, the simulated channeling yields are all normalized according to the *random* level. The *random* level represents the expected yield from a sample deprived of any channeling effect and in practice it is composed of the dopants in an amorphous sample. Because of this, a fraction is also attributed to the random level, the value of which is set to satisfy the condition that when added together with the values of the other site fractions (often also called "regular fractions"), the sum reaches 100 %.

Consider as example the counting of particles at the angular position (ϑ, ω) of a sample with three occupied sites. The sites, $\{1, 2, 3\}$, have as respective simulated normalized yields $\{\chi_1(\vartheta,\omega), \chi_2(\vartheta,\omega), \chi_3(\vartheta,\omega)\}$ and respective occupancy fractions, $\{f_1, f_2, f_3\}$. In this formulation, the relation between the number of counts $N(\vartheta,\omega)$ and each of the three sites' normalized yield contribution is defined as,

$$\frac{N(\vartheta,\omega)}{N_R} - 1 = f_1\left(\chi_1(\vartheta,\omega) - 1\right) + f_2\left(\chi_2(\vartheta,\omega) - 1\right) + f_3\left(\chi_3(\vartheta,\omega) - 1\right) , \tag{3.2.1}$$

where N_R is the expected number of counts if the sample were amorphous and therefore devoid of any channeling effect. As an amorphous sample produces a pattern with no anisotropy, N_R is independent of the measurement direction. Solving the equation for $N(\vartheta,\omega)$ results in,

$$N(\vartheta,\omega) = N_R \times \left(f_1\chi_1(\vartheta,\omega) + f_2\chi_2(\vartheta,\omega) + f_3\chi_3(\vartheta,\omega) + 1 - f_1 - f_2 - f_3\right) . \tag{3.2.2}$$

The pattern expected from a sample with no channeling effect is termed *random pattern*, in the normalized yield definition all of its bins have value 1. Note that for comparison, yields for a simulated pattern are commonly in the range 0.5 to 2. A random pattern, $Rand$, is always included in the fit and is associated with a random fraction f_{Rand}. In fitting an experimental pattern, the random fraction, besides being a measure of possible amorphization of the sample, also accounts for the background from gamma or scattered beta particles. Correction methods for the random fraction are explained in section 3.3.1.

In order to build a p.d.f. to fit a measured channeling pattern, the first step is to calculate the yield pattern Y, that combines the contribution of every site. Continuing with the three sites example, the yield pattern equation is,

$$Y_{ideal}(f_1, f_2, f_3) = f_1{\cdot}\chi_1 + f_2{\cdot}\chi_2 + f_3{\cdot}\chi_3 + (1 - f_1 - f_2 - f_3).Rand\,, \tag{3.2.3}$$

with the random fraction f_{Rand}, not directly present, as it is set by the condition $f_1 + f_2 + f_3 + f_{Rand} = 1$.

The yield pattern is then convoluted with a Gaussian function of angular standard deviation σ to take the setup angular resolution into account. Resulting in,

$$Y(f_1, f_2, f_3, \sigma) = GaussianConv(Y_{ideal}(f_1, f_2, f_3), \sigma)\,. \tag{3.2.4}$$

The next step is to map the yields to the histogram bin mesh. Because the yield pattern is simulated with an angular step that does not match the angular distance between pixels nor an alignment is expected between the two meshes, an interpolation of the yield values at each of the histogram bin angular positions is required. Furthermore, the bin angular positions are dependent on the relative orientation of the yield pattern to the histogram resulting from the particular orientation of the measurement. Keeping the measured histogram as a fixed frame of reference, the orientation of the yield pattern is defined by a rotation, ϕ, and a translation, $(\Delta x, \Delta y)$. The oriented yield pattern in the experiment referential is therefore defined as $Y\left(f_1, f_2, f_3, \Delta x, \Delta y, \phi, \sigma\right)$.

During the interpolation of the yield pattern to find its value at the bin location, if the bin has a greater surface corresponding to a bigger solid angle value a single point might not suffice to have an accurate value of the yield. For this situation, it is better to interpolate over a mesh of *sub-pixels* inside each bin and then average the results.

The last step is to transform the yields into probabilities by normalizing the integral to 1. The function, now a p.d.f. and represented as $p.d.f.\left(f_1, f_2, f_3, \Delta x, \Delta y, \phi, \sigma\right)$, is calculated as,

$$p.d.f.\left(f_1, f_2, f_3, \Delta x, \Delta y, \phi, \sigma\right) = \frac{Y\left(f_1, f_2, f_3, \Delta x, \Delta y, \phi, \sigma\right)}{\sum_i^{N_{bins}} Y_i}\,. \tag{3.2.5}$$

where i is the index of each bin used in the analysis. Bins that are masked and bins that are outside of the fit range are discarded.

The p.d.f. can now be used for estimating the parameter values. This is done by finding the parameters that minimize the cost function $C(\theta)$, where θ represents the variables that are optimized. In the maximum likelihood method, $C(\theta) = -LL(\theta)$, and therefore the parameter estimators are built as,

$$\begin{aligned}\left(\hat{f}_1, \hat{f}_2, \hat{f}_3, \hat{\Delta x}, \hat{\Delta y}, \hat{\phi}, \hat{\sigma}\right) = \\ = min_{(f_1, f_2, f_3, \Delta x, \Delta y, \phi, \sigma)} \left(-\frac{N_{cts}!}{O_1! \ldots O_{N_{bins}}!} \prod_{i=1}^{N_{bins}} p.d.f.\left(f_1, f_2, f_3, \Delta x, \Delta y, \phi, \sigma\right)_i^{O_i} \right)\,.\end{aligned} \tag{3.2.6}$$

Alternatively, with the chi-square method $C(\theta) = \chi^2_P(\theta)$ and the parameter estimators are built as,

$$\begin{aligned}\left(\hat{f}_1, \hat{f}_2, \hat{f}_3, \hat{\Delta x}, \hat{\Delta y}, \hat{\phi}, \hat{\sigma}, \hat{N}_{cts}\right) = \\ = min_{(f_1,f_2,f_3,\Delta x,\Delta y,\phi,\sigma,N_{cts})} \left(\sum_{i=1}^{N_{bins}} \frac{\left(O_i - N_{cts} \times p.d.f.\left(f_1, f_2, f_3, \Delta x, \Delta y, \phi, \sigma\right)_i\right)^2}{N_{cts} \times p.d.f.\left(f_1, f_2, f_3, \Delta x, \Delta y, \phi, \sigma\right)_i} \right) \\ = min_{(f_1,f_2,f_3,\Delta x,\Delta y,\phi,\sigma,N_{cts})} \left(\sum_{i=1}^{N_{bins}} \frac{(O_i - E_i)^2}{E_i} \right).\end{aligned} \tag{3.2.7}$$

Where the expected number of counts in bin i is defined as, $E_i = N_{cts} \times p.d.f.\left(f_1, f_2, f_3, \Delta x, \Delta y, \phi, \sigma\right)_i$. Also, O_i represents the number of counts in bin i, N_{bins} is the total number of bins and N_{cts} is the total number of counts.

Although all of the p.d.f. parameters, $(f_1, f_2, f_3, \Delta x, \Delta y, \phi, \sigma, N_{cts})$, can be estimated from the fit of the experimental channeling pattern this might not be the best choice in all cases. In the case of the total number of counts, N_{cts}, it is more accurate if one obtains it directly from the pattern. This is particularly relevant when doing chi-square fits of patterns with a low number of counts as the chi-square method has a large bias in this parameter. Another important case is for the parameter responsible for the Gaussian convolution, σ, as it can be estimated from the setup geometry (see table 3.2).

3.2.3 Fitting methodology improvements

The methods presented in the last two sections, 3.2.1 and 3.2.2, are the improved analysis methods used in this thesis and implemented in the PyFDD software. In this section the parts of the analysis methods that were improved over the previous fit software, FDD, are highlighted and it is described how these changes can affect the fit results.

The first change is in the preparation of the data. It comes as a change in the approach to deal with data points for which no simulations values exist. As many-beam simulations usually only cover an angular range of $[-3°, 3°]$ in relation to the crystal axis and as it often happens that the channeling axis is not perfectly centred in the detector, it is a recurrent situation that some of the measurement bins lie outside of the simulated range. These bins can not be used for the fit, and it happens that the way to exclude them is not the same in each software.

In PyFDD the approach chooses to mask bins that are over $\approx 2.7°$ from the user defined center, allowing a small margin for angular position optimization. This ensures that the number of bins remains constant during the fit which is a requirement for both the chi-square and maximum likelihood methods defined, as they are, in the previous section. Furthermore, keeping the number of bins fixed is necessary for a correct comparison of the cost function fit minima across different lattice sites both in terms of determining the best site and in terms of evaluating its associated uncertainty. This is relevant for both

the chi-square and maximum likelihood cost functions as the total number of bins has a strong influence on their absolute value. This process has the consequence of not using all of the available data. For example, considering that the detector covers a range of $\approx 5°$, a pattern that is shifted from the centre in one direction by 3° will be analysed with a 6 % loss in data points. This can be reduced by using a better input for initial orientation and then increasing the fit range.

In a different approach, for FDD it was chosen to use the maximum number of data points available for the fit, it thus discards outlying bins at each optimization step. It does this by optimizing the reduced chi-square i.e. the chi-square value divided by the number of degrees of freedom (n.d.f.).The fact that the number of bins is not constant but may change during the fit can cause errors in $(\hat{\Delta}x, \hat{\Delta}y, \hat{\phi})$, if the fit routine sees that a reduction in the number of bins to fit is beneficial in comparison to a slightly off value in any of the orientation variables. Nonetheless it should be noted that the circumstances under which the orientations are lost are very rare and occur mostly when the pattern is being fit with sites that differ significantly from the measurement.

Another change is the choice of chi-square. PyFDD uses the Pearson chi-square while FDD uses the Neyman chi-square. The difference is that PyFDD gets each bin variance value from the simulation expected number of counts while FDD gets the variance from the measurement's number of counts. This difference is only significant when the number of counts per bin are low, and in this case the Neyman chi-square is known to have a larger bias than its counter part. The fact that FDD uses a chi-square normalized with the n.d.f. also diminishes, but does not remove, the effect that the comparison of fits between lattice sites may in effect be between patterns where the number of selected bins for the fit might differ.

The third difference between the two methods is how they deal with measurement bins that have a large solid angle, as in these cases the simulation value for the whole bin can not be fully characterized by a single interpolation point in the simulated pattern. On one hand, PyFDD chooses to make a fine mesh inside each pixel and average the simulation values over all of the mesh points. On the other hand, FDD chooses to divide each experimental bin in a larger set of bins with equal value (normalized counts). In the latter case the channeling pattern used in the fit will have more bins than the measurement has pixels. This approach has the problem that is does not use average yields for the bin area, but instead optimizes the square of the differences over the bin area between several points in the simulation yield function and the constant bin value, which is not a completely accurate representation of the physical effect. Additionally it changes the significance of the used chi-square as the bins are no longer independent between each other, in fact, many are duplicates.

The last improvement worth mentioning is that the optimization routine used in PyFDD allows bounded variables. This is used to ensure that the occupancy fractions from the fit can never be negative, a common situation in FDD.

3.2.4 Statistical and systematic uncertainties

Having an idea about the magnitude of the uncertainty in the estimated values gives perspective into the confidence of the results. Additionally, in the scope of this thesis, it can give a strong argument when comparing one detector to the other in terms of the quality of the results.

The first kind of uncertainty to be described here are statistical errors. The concept of this kind of errors has been explained at the end of section 2.4. The calculation starts with the Hessian matrix of second derivatives evaluated at the minimum of the cost function, $\hat{\theta}$, as,

$$[H(\theta)]_{ij} = \left[\frac{\delta}{\delta\theta_i \delta\theta_j} C(\theta)\right]_{\hat{\theta}} \quad . \tag{3.2.8}$$

Where the cost function $C(\theta)$ is either the chi-square $\chi^2_P(\theta)$ or the negative log likelihood $-LL(\theta)$, depending on what was used in the optimization. Then the errors are calculated from the diagonal of $H(\theta)$, as described in equation 2.4.17 and 2.4.18 and here repeated,

$$\sigma_{\hat{\theta}_i} = \frac{1}{\sqrt{[H(\theta)]_{ii}}} \quad , \tag{3.2.9}$$

for the likelihood case. Equivalently,

$$\sigma_{\hat{\theta}_i} = \frac{1}{\sqrt{\frac{1}{2}[H(\theta)]_{ii}}} \quad , \tag{3.2.10}$$

for the chi-square case.

When estimating a lattice site displacement statistical error this latter approach does not work as it is a non continuous variable and therefore not differentiable. Alternatively, the process is to apply equations 2.4.19 or 2.4.20. As it often happens that this error is smaller than the displacement step used in simulation there is not much relevance given to it.

Besides statistical errors, systematic errors also exist. These can, in between other factors, have origins in the many-beam simulations, poor characterization of the detection system, the usage of a physics model that does not fully represent the experiment and background effects. Later in this chapter, section 3.3 explains the effects that background can have on the statistical and systematic errors.

There is no precise method to estimate systematic errors when the true value of a parameter is unknown, in some situations the best value that can be given for the systematic error is just an educated guess. A more scientific method is to look at a set of independent experiments and look at the results dispersion beyond the expected statistical fluctuations and use this as a measure of systematic uncertainty. In emission channeling, one can use the measurements of several axes of a sample to get an idea of how the results diverge. Of course the measurement of each axis cannot be considered as an

independent experiment as many factors are maintained, still it commonly happens that the results vary more than expected by statistical variation.

The methodology, here presented, to estimate systematic errors from a set of measurements of different axes can only be applied in the case that the difference in the fractions or lattice sites between directions is significantly larger than what is expected from the statistical errors. Consequently, as the statistical errors are outweighed by the systematic errors, it is considered that all measurements have the same uncertainty. If this condition applies, then, using the estimated values for each direction, $\hat{\theta}_1, \hat{\theta}_2, \hat{\theta}_3$, the resultant value is a simple average,

$$\bar{\theta} = \frac{\hat{\theta 1} + \hat{\theta 2} + \hat{\theta 3}}{3} . \tag{3.2.11}$$

The error, is then chosen equal to the largest difference between the average and the estimate from any direction,

$$\Delta\hat{\theta} = max(\left[\hat{\theta}_i - \bar{\theta}\right]_{i=1,2,3}) \quad . \tag{3.2.12}$$

Here, because the uncertainty is not the standard error, it is represented by a Δ.

In the alternative case where the difference of results in between directions is close to what is expected from the statistical errors, joining the results is done in another process. In this case, the results are added together by weight of the variance, such as,

$$\hat{\theta} = \frac{\frac{\hat{\theta}_1}{\sigma^2_{\hat{\theta}_1}} + \frac{\hat{\theta}_2}{\sigma^2_{\hat{\theta}_2}} + \frac{\hat{\theta}_3}{\sigma^2_{\hat{\theta}_3}}}{\frac{1}{\sigma^2_{\hat{\theta}_1}} + \frac{1}{\sigma^2_{\hat{\theta}_2}} + \frac{1}{\sigma^2_{\hat{\theta}_3}}} . \tag{3.2.13}$$

With resulting variance calculated as,

$$\sigma^2_{\hat{\theta}} = \frac{1}{\frac{1}{\sigma^2_{\hat{\theta}_1}} + \frac{1}{\sigma^2_{\hat{\theta}_2}} + \frac{1}{\sigma^2_{\hat{\theta}_3}}} . \tag{3.2.14}$$

3.3 Gamma and scattered electron background

In an Emission Channeling (EC) experiment there are two types of background. One is gamma radiation from the decay of probe isotopes in the sample and in the collimator, other radioactive sources in the laboratory, natural radioactive sources in the vicinity and cosmic radiation. The other are beta particles that, despite being emitted from the sample outside the detector solid angle, have scattered inside the

sample itself or on the chamber walls, thus losing all channeling information.

The background not only adds counts to the channeling pattern lowering the intensity of the channeling effect but it also adds a random noise contribution to the number of counts per pixel increasing the uncertainty of the measurement. In order to correct for the perception of lower fractions due to the reduction in intensity of the channeling effect in a pattern, background corrections need to be applied after fitting the data. On the other hand, the noise contribution can only be mitigated by removing the background at the source or by selectively removing its events. The next section explains how the fractions are corrected and is followed by two sections that show how to quantify the correction fractions for both radiation types. In the last section a method is proposed for selectively removing the background during the cluster data treatment.

3.3.1 Background correction factor for occupancy fractions

After fitting a channeling pattern, the obtained fractions are not absolute values and need to be corrected for the background. During the fit it is assumed that the sum of all fractions, including the random fraction, should add up to 1. However, since the random fraction usually also includes a contribution from the background, the fitted site fractions and the random fraction itself need to be corrected for this contribution to the pattern.

Note that the background corrections as described below are of course subject to errors, e.g. due to inaccuracies in the modelling of backscattered electrons, or in the procedures how to estimate the gamma background. Also, sources of background may change over the time of an experiment, e.g. because of the decay of background isotopes in the vicinity of the detector. The absolute site fractions derived by this method are hence subject to an error, which is often estimated to be in the 10 % range. In order to compare site fractions that are not subject to this error, it is often chosen to use relative site fractions, i.e. the fit values f_i for all regular sites are summed, and individual site fractions are given relative to this sum value.

If the measurement of the random fraction is desired, then the contribution of the gamma and the beta backgrounds have to be estimated.

The beta background is due to beta particles which are emitted from within the sample under study, however, in a direction which does not point to the detector, but which still reach the detector due to scattering events in the sample or on the chamber walls.

The correction factor for the beta background is obtained from GEANT4 [65] Monte Carlo (MC) simulations of the scattering of beta particles within the measurement chamber. With D_{e^-} and S_{e^-} denoting the detected number of direct and scattered electrons, the correction factor F_{e^-} is calculated as,

$$F_{e^-} = \frac{S_{e^-} + D_{e^-}}{D_{e^-}} \,. \tag{3.3.1}$$

Equivalently, although using experimental data, the gamma background correction factor is defined as,

$$F_\gamma = \frac{N_{cts}}{N_{cts} - N_\gamma} \,, \tag{3.3.2}$$

where N_{cts} is the total number of counts in a measurement and N_γ is the respective number of expected gamma events, which is calculated from the rate of gamma events during the experiment. The gamma rate is measured by closing for a period of time the vacuum valve in front of the detector which is assumed as essentially transparent for gammas but blocking beta particles.

Once the beta and gamma correction factors are calculated, the total correction factor F is given by,

$$F = F_{e^-} \times F_\gamma \,. \tag{3.3.3}$$

Then each fraction from the fit can be corrected as,

$$f_{i\,corrected} = F \times f_i \,. \tag{3.3.4}$$

Similarly the error in the fraction is corrected as,

$$\sigma_{f_i\,corrected} = F \times \sigma_{f_i} \,. \tag{3.3.5}$$

An intuitive way to understand the fraction correction formula is that by removing the background the anisotropy generated by the channeling increases by the factor F, and consequently the measured fractions f_i. Another way is to consider that during the fit the fractions should include the background and consequently the sum of all fractions should add up to F instead of 1.

3.3.2 Scattered electron background simulations

The background of scattered electrons consists of beta particles that reach the detector in a non direct way and that in their path have lost all channeling information. Beta particles suffer two types of scattering events that can redirect them towards the detector from an arbitrary emission direction, one being scattering inside the sample material and the other being scattering with the walls of the chamber

structure. This effect is also responsible for the fact that the electron detection rate is higher than what would be expected from the decay rate and the detector solid angle.

Insights on electron scattering are learned from GEANT4 MC simulations that track the betas emitted from within the sample. This GEANT4 application that simulates the chamber and detector used was developed initially by Bart de Vries in 2003 [67] and has been updated by several students since.

In these simulations electrons are generated according to the depth profile of the implanted isotopes calculated from SRIM [51] and with an energy corresponding to the beta decay spectrum. The initial momentum direction is randomized over 4π. Particle motion is simulated in GEANT4 by means of choosing small steps during which the particle may be deflected by electromagnetic interactions with its environment. In these simulations, at the end of each step it is verified whether a relevant electron scattering event occurred. Respective to the particle tracking in the sample, an electron is flagged as scattered if at some point it reached the sample substrate, if it originated secondary electrons or if its distance to the detector increased. Respective to the particle tracking in the chamber, the scattering of an electron on the chamber walls is signalled if the electron reached the wall. When scattering occurs the electron is tagged with the type of scattering (sample or wall), then, if it reaches the detector it will be counted as a scattered electron. Electrons that reach the detector directly are also counted.

As only a small fraction of simulated electrons actually reach the detector (typical solid angles are around 8×10^{-3}), a large number of particles need to be simulated. For a very good accuracy at the 30 cm setup, 50 M particles are necessary. At the end of the simulations, the number of electrons that reach the detector directly and the number of electrons that reach the detector by scattering are used in equation 3.3.1 to calculate the correction factor.

The main updates that were made for this thesis on the GEANT4 application was to update the code in order to be compatible with the newest version of GEANT4, small corrections to the chamber geometry, the use of a physics list now available in the GEANT4 package that includes a bundle of physics interactions and serves as a substitute for the previously used list of interactions that had to be coded by the user, in this case the `QGSP_BERT` standard list was used, and finally the inclusion of the timepix-quad setup geometry. Updating to the newest version of GEANT4 allowed the code to be more portable as at the time it was only possible to run the code in a virtual machine that required a heavy ($>$10 Gb) file.

Fig. 3.4 shows the representation of the two simulated structures in the GEANT4 application used in this thesis. Because it is not expected that multiple scattering events occur before a particle reaches the detector, only parts of the chamber that are close to the line of sight with the detector are considered for scattering. The two structures are for simulating the pad and the timepix-quad detector setups. The main difference between them are the detectors, in green, and the position of the collimator, in yellow.

As one of the updates to the GEANT4 simulation was the introduction of a pixelized timepix detector

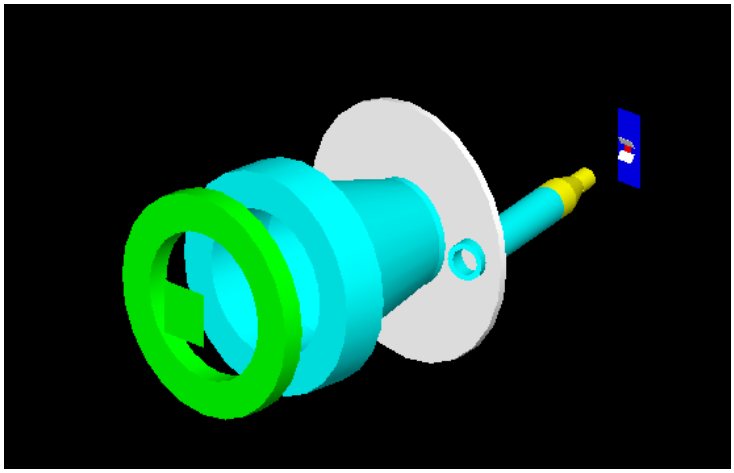

(a) Pad detector simulation setup viewed from a perspective angle.

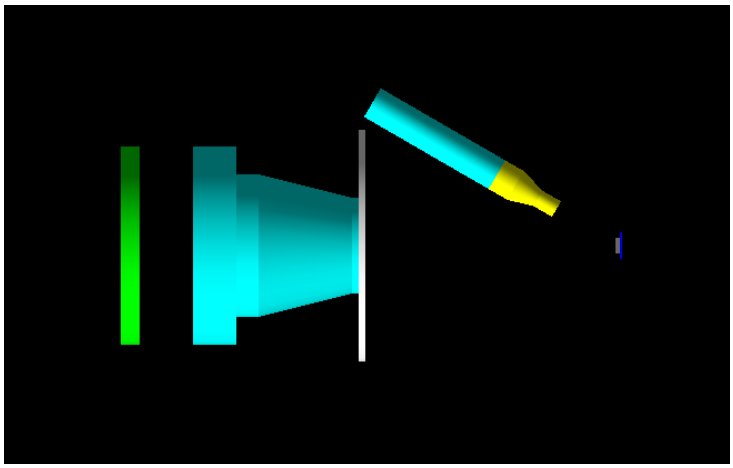

(b) Timepix quad detector simulation setup viewed from the top.

Figure 3.4: Geometrical structures for the simulation of the pad and timepix-quad setup, in the beta scattering GEANT4 application. Because it is unlikely that a particle with multiple scattering reaches the detector only the part of the chamber towards the detector is simulated. The differences between the setups are the positioning of the collimator for the ion beam (in yellow) and the detector shape.

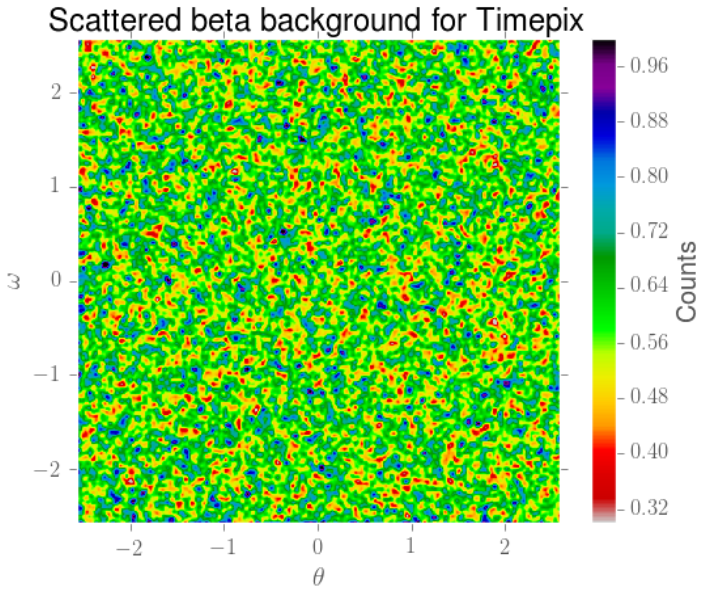

Figure 3.5: Background pattern resulting from a GEANT4 simulation of ^{24}Na implanted in GaN on the timepix-quad setup. 500 M particles were simulated in a run that took 4 days. Since only a fraction of simulated particles reach the detector with 512 by 512 pixels the original pattern had to be smoothed for a better visualization. It is due to the smoothing that the color scale has fractional values. As it appears, the pattern is uniform, it is therefore not expected to originate any bias in the analysis.

it became possible to simulate a two dimensional (2D) background pattern and see if it is uniform. This test is relevant as a non uniform background could create a bias towards some sites. From a GEANT4 simulation of 500 M events in the timepix-quad setup, resulting in the pattern of figure 3.5, no anisotropy could be seen over the detector area. It is therefore assumed that the background of scattered electrons is uniform and does not introduce a systematic bias on the lattice site location.

3.3.3 Gamma background

Gamma background, despite being in general lower than the scattered beta background is noticeable for not being uniform. While in a normal experiment scattered betas can account for 40-50 %, gammas typically account for only 5-10 %. The gamma background can be measured approximately during the experiment by shielding the detector from beta radiation but leaving it exposed to the gamma radiation. This is routinely done by closing the vacuum valve in front of the detector.

The sources for gamma background differ for on-line and off-line measurements. The largest sources of gamma radiation for off-line measurements are possible gamma decays of the probe isotope in the sample itself, other radioactive sources from the laboratory environment, Naturally Occurring Radioactive Materials (NORM) and cosmic radiation. The event rate from these sources of background radiation is very small, it may be as low as one count every few seconds, but this can be comparable to the

sample count-rate when measuring long lived isotopes with $t_{1/2} > 20\,\mathrm{days}$ that have low activity. Radiation from the environment background is expected to irradiate the detector uniformly. Nonetheless, the background radiation might cause non uniformity in case the detection efficiency of the detector is not constant over the detector area, which may happen for example if the detector is not fully depleted.

For on-line measurements the major gamma background source is the gamma decay of isotopes in the sample itself and in the collimator nozzle. Besides, other smaller contributions exist, such as decays in the beam line and in the isotope separator magnet. It is the combination of various sources at different locations, the shielding by the chamber structure and the detector efficiency that cause the background anisotropy in on-line measurements.

Figure 3.6 shows two background patterns for on-line measurements, ^{124}In taken with the timepix-quad detector and ^{56}Mn taken with the pad detector. Both background patterns were taken by closing the vacuum valve in front of the detector and thus blocking the beta radiation. From the figure, it can be seen that there is a horizontal effect, with more counts near the top and bottom edges than in the center. Unfortunately ^{124}In was the only background pattern measured with the timepix that had enough statistics to show a clear structure, for this reason it was not possible here to show the background uniformity for the same isotope in both detectors.

The effect that these kind of background patterns have on the determination of lattice site locations can be exemplified by using these patterns as input in a fit. Obviously the desired output of this test is that all site fractions will be zero. On the contrary, in case the obtained fractions differ from zero significantly more than their respective error bars, then some bias is being introduced by the background.

For fitting the background patterns the orientation variables were fixed at zero $\Delta x = 0, \Delta y = 0, \phi = 0$ and the smoothing variable fixed at $\sigma = 0.05$. In the fit routine only the site occupancy fraction was allowed to vary. The fits were made with all the sites from ^{24}Na in GaN libraries and for three off-surface directions.

Figure 3.7 shows the result of the fit of the background patterns of Fig. 3.6 with a set of libraries for ^{24}Na in GaN. From these results it can be seen that presence of the non uniform gamma background can result in an increase or decrease in the fractions of some lattice sites. Naturally, sites or combinations of sites that produce a flatter pattern are more affected by the background although it also depends on the pattern orientation. Note that even fitting a flat background that is only subject to random counting statistical fluctuations can result in site occupancy fractions that are different from zero, although with fitted site fractions that are close to the statistical errors from the fit. In this sense, the important distinction to make for the effect of the background is between an introduction of variance by a flat background, i.e. an increase in the error bars, and an introduction of bias by a non uniform background, which will affect the accuracy of the result. The variance caused by a flat background can be reduced by acquiring more data, the same can not be done for an induced bias.

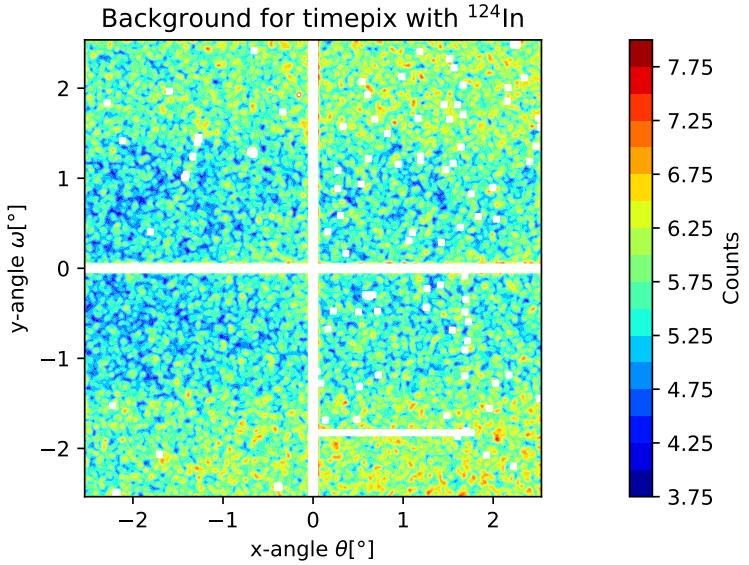

(a) Background pattern on the timepix-quad detector during a ^{124}In beam.

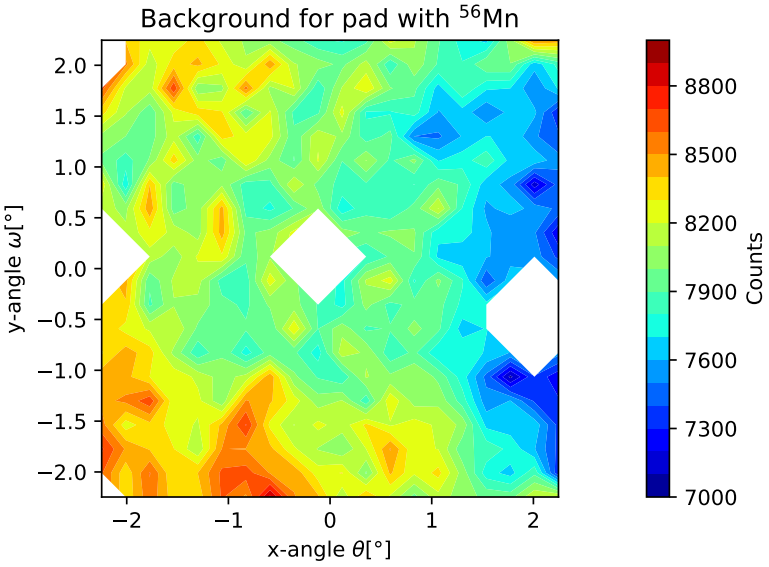

(b) Background pattern on the pad detector during a ^{56}Mn beam.

Figure 3.6: Non uniformity of the gamma background in the pad and timepix-quad detectors. The background on both detectors produces a similar pattern with more counts on the top and bottom than the central horizontal line. Patterns with different isotopes are shown because there were limited measurements of background that could produce a good quality image.

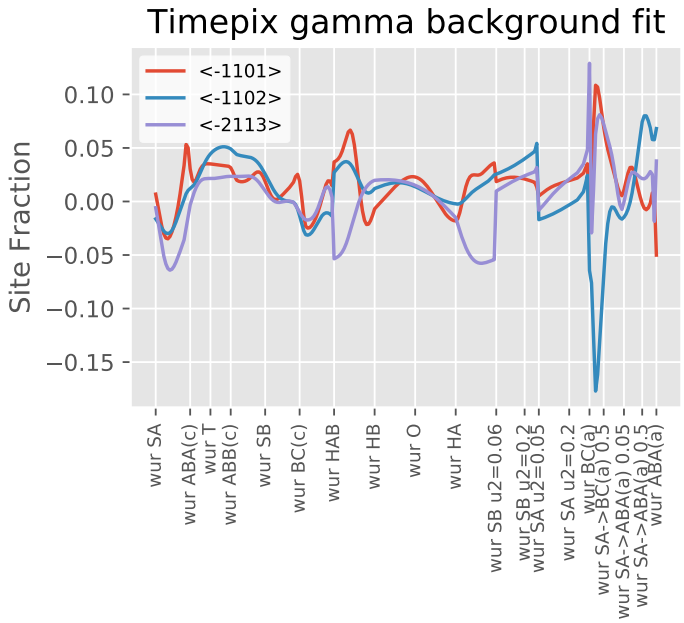

(a) Site fraction obtained by fit of the timepix-quad background pattern with simulated ^{24}Na in GaN patterns.

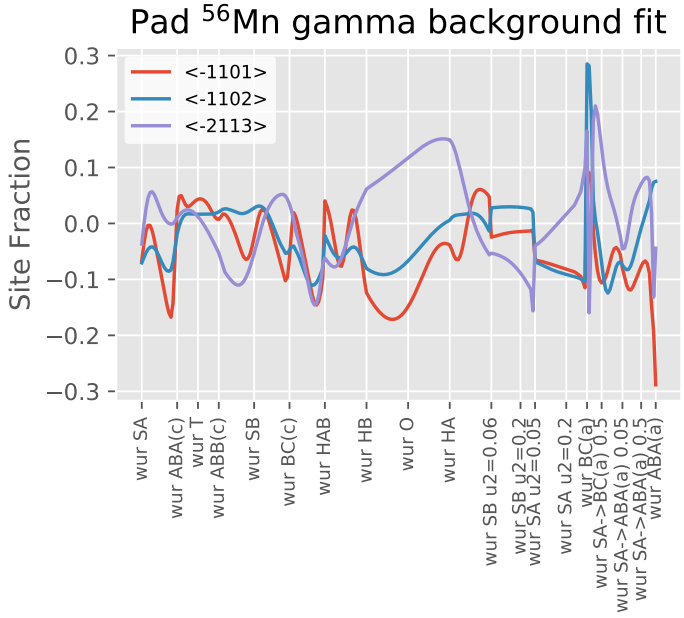

(b) Site fraction obtained from the fit of the pad background pattern with simulated ^{24}Na in GaN patterns.

Figure 3.7: Fit of the background patterns in Fig. 3.6 with simulated patterns of ^{24}Na in GaN. Fits were calculated with the simulated patterns centered and not rotated, i.e., only the site fraction and number of counts were fitted. This shows that the non uniform background can cause a bias towards some sites (see Fig. 5.1 for a description of lattice sites). Additionally, it shows that it is rare for the fraction contribution to be consistent over all the axes.

One possibility for avoiding bias caused by the background, which could be an interesting future project, is to model the background pattern and include it in the fit model. However one should be aware of the costs that such a procedure would involve, specifically the loss of quality beam time that would have to be spent in measuring good quality background patterns, which due to the low intensity would take much longer than acquiring a regular channeling pattern. Since events from the gamma background are a small fraction of the total, about 10 %, and any effect is only as strong as the background intensity, the background non uniformity is generally accepted as an unavoidable error source. Also, because the effect on the lattice sites is not coherent for each direction it is possible to avoid some of the bias by cross validating the measurements of different axes with each other.

To reduce this effect, next section proposes a method of selectively removing background events that has only become possible with the timepix detector.

3.3.4 Reducing gamma background with event selection

The timepix-quad detector has two advantages over the pad when it comes to gamma background. The first being that due to its lower thickness of 300 µm vs the pad detector 500 µm, if in both cases the whole detector volume is fully depleted then the timepix detection efficiency for gammas is comparatively $^2/_5$ lower than the pad, all while keeping beta detection efficiency unchanged. In practice, the efficiency difference is not as large as the pad detector is operated under-depleted, due to the necessity of reducing the leakage current. The other advantage is the possibility of using the hit cluster shape to identify the type of radiation, gamma or beta. The simplest way of doing this is by selecting events according to the number of pixels that are activated by the particle when hitting the detector, i.e., the cluster size.

Because of the different nature of interactions that photons and betas have with the sensor it is expected that the two types of radiation type will deposit energy in areas of different sizes. By means of multiple scattering with electrons in the Si material, beta particles continuously deposit energy along their path that leads to the formation of electron hole pairs that are ultimately detected in the sensor. Due to the high energy of the electrons involved, the scattering can occur over a large volume and therefore activating several pixels before the whole beta energy is deposited or the energetic electrons escape the sensor. The gamma energy range usually present in emission channeling experiments is from a few keV to a few MeV, which is similar to the energy range for betas. Gammas in this range interact with the Si sensor mostly by Compton scattering, creating energetic electrons in the process that will interact with the sensor in the same way as beta particles. However, the energy of the energetic electrons is always a fraction of the energy of the gamma that originated it, for this reason, and especially when the gamma energy is low at start, the energy deposition will be localized and therefore affecting only a small number of pixels. However, if the energy of the secondary electron created by the gamma Compton scattering is large enough then the two types of events (gamma vs beta detection) can not be distinguished.

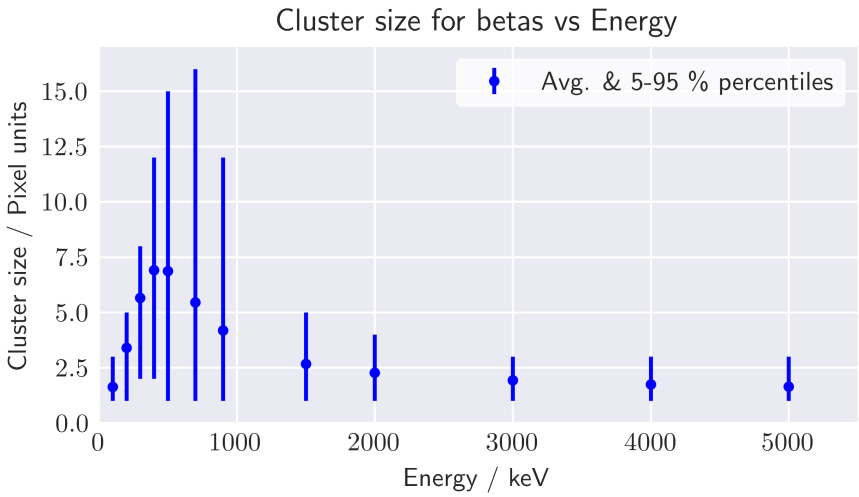

(a) Cluster size distributions for beta particles of various energies.

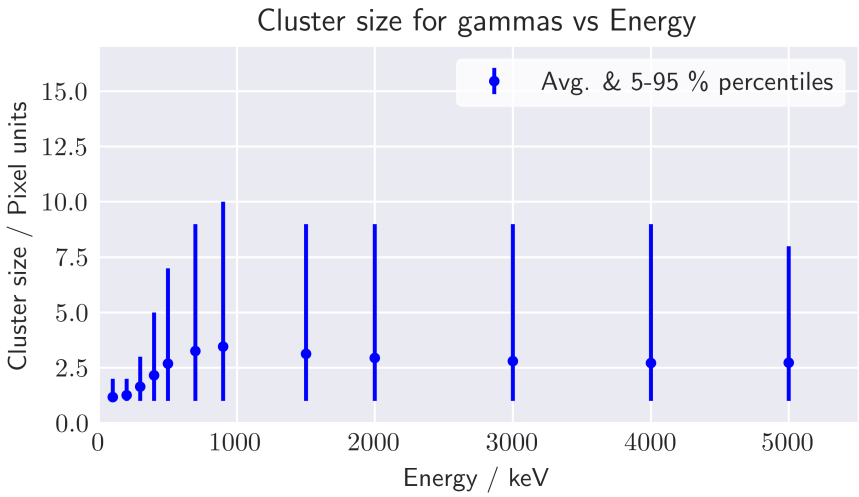

(b) Cluster size distributions for gamma particles of various energies.

Figure 3.8: Plots of the cluster size in number of activated pixels, for beta and gamma radiation in a perpendicular incidence configuration on a 300 µm Si timepix detector obtained by GEANT4 simulations. In the plot the dot represents the average value and the bars the 5-95 % percentiles. It can be seen that in general the cluster size for betas is much larger than for gammas. Beta radiation creates a larger share of big clusters around 500 keV, after which the chance for large scattering events decreases. For gamma radiation the cluster size keeps increasing up to 900 keV where it effectively stabilizes.

Figure 3.8 shows the cluster size distribution for several gamma and beta energies. It can be seen that small clusters are more common for gamma radiation, although betas of very small or very big energies also create small clusters. For this reason, selecting events based on their cluster size will also affect the detection efficiency for beta radiation. In a typical EC experiment this will specially affect low energy betas.

If this selection method is used, because the detection efficiency is energy dependent, the beta energy distribution used in the channeling simulations needs to reflect this efficiency on top of the isotope emission spectrum. It is therefore necessary to understand how cluster selection affects the energy spectrum that is measured.

GEANT4 simulations of detection efficiency with cluster selection were made considering a cluster selection process where a minimum cluster size for accepting a hit is stipulated and no maximum size. These simulations consisted of a beam of gamma and beta particles hitting a 256×256 array of pixels with dimensions of 55 µm side and 300 µm depth. The initial location of the beam particles was uniformly distributed over a central pixel. A pixel trigger threshold of 15 keV was used. The same procedure was used for gamma and beta radiation to get the data represented in figures 3.8 and 3.9.

Figure 3.9, shows the results for the detection efficiency with cluster selection. Gamma detection efficiency decreases rapidly as small clusters are removed. Simultaneously, there is a an undesired loss of detection efficiency in beta particles that is not uniform across energies, which results in the emitted and measured beta energy spectrum being different. The data from Fig. 3.9a can then be used to correct the emitted spectrum with the chosen cluster selection method.

Because of the loss of beta efficiency it is not advised to use a minimum cluster size above 2. None the less, this can result in a significant reduction of gammas under 500 keV and a reduction of about 30 % above that. At the same time, a minimum size of 2 will maintain a fair efficiency for beta particles.

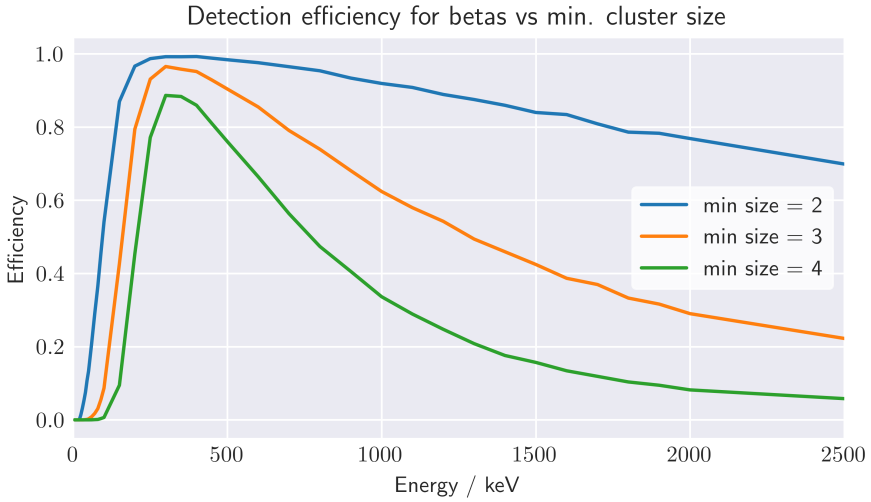

(a) Detection efficiency for beta particles. At low energies the pixel trigger threshold of 15 keV also plays a role in reducing the detection efficiency.

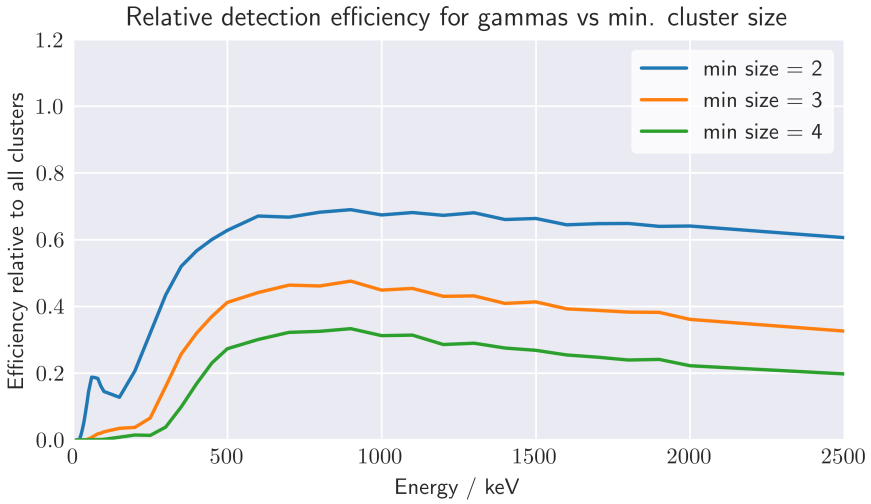

(b) Detection efficiency for gamma particles relative to the efficiency when using all cluster sizes.

Figure 3.9: Detection efficiency change with selection by cluster size. The plot show how the detection efficiency for betas and gammas is reduced when removing small clusters. The efficiency drops faster for gamma than for beta radiation enabling to filter some of the gamma background.

4

Software

A significant part of the Emission Channeling (EC) experimental procedure is the data handling, starting from the detector readout up to the pattern fit. Some of the software used in this process comes from the medipix community, this is the case for the readout program Pixelman (now commercially available as PIXet) and the clustering framework MAFalda which was then adapted to this case. The rest of the software was developed as part of this thesis work.

This chapter has the objective of outlining the software used in order to facilitate its adoption by a future user or future developer. For this reason, underlying problems and chosen solutions are explained. The chapter is also written keeping in mind that, as the medipix development environment evolves so quickly, many of the tools used in this thesis would require an update in order to be suitable for the latest detectors.

The first section of this chapter explains the distribution of the computing system between a measurement and control unit and a data treatment and visualization unit. The second section talks about the software used for cluster identification when treating data from the timepix detector. The last section is about the PyFDD software developed during this thesis, giving examples on how it can be used for data visualization and analysis and also explaining the overall structure of the software classes.

4.1 Computing system - data acquisition and transfer

The computational steps required for the analysis of Emission Channeling (EC) lattice location experiments can be divided in three parts (not taking into account performing the many-beam simulations): Data acquisition, responsible to record and store the measurements; data treatment, treats the measurement event data and builds a channeling pattern from it; data analysis, helps visualize the channeling pattern and does the fit with many-beam simulations.

The data acquisition is the most critical system and it is mounted in a separate computing unit in order to avoid interference from other processes that might overload the computer and slow down or even cause to stop the acquisition. The acquisition with the timepix detector is done by the control program PIXet (v.1.4.2, by Advacam s.r.o., Prague, Czech Republic). The program was set in repeat mode, such that sequential acquisitions of 600 frames were made with each sequence being stored in a separate text file. Using an acquisition time of 0.1 s means that at roughly every minute a new file is produced. For a count rate of 2500 hits /s this results in the storage of roughly 10 MB a minute. As a result, due to the large number of files created per measurement, each measurement is stored in a different folder.

The stored files are just the raw data of the measurement with each line in the file representing the (x, y) coordinates of a triggered pixel and the number of hits in the pixel. As the detector was operated in counting mode no information on the Time over Threshold (ToT) was taken. At the end of each frame a line with the # character is printed. An extract of the data file looks like this:

```
136 40  1
137 40  1
317 401 1
#
403 2   1
403 3   1
#
245 45  1
245 46  1
245 47  1
245 48  1
#
```

These long data files need to be transferred to another computing unit where the data treatment and data analysis systems are set up. While the final data analysis usually takes place well after finishing the experiment, already during data acquisition frequent visual displays of the measured pattern are required in order to monitor the ongoing experiment. Therefore, this transfer process needs to be done in a fast and non disruptive manner that can be frequently repeated. This was achieved with a small shell script that had two tasks, first it would locally mount the data folder from the data acquisition unit (shared via the CIFS protocol), and second, using the linux `rsync` command which, without disturbing any ongoing measurement or file write operations, would read the data files and transfer only the last changes over to the data treatment and analysis unit. The section of the bash script responsible for

Listing 4.1: Section of the bash script responsible for transfering the data files.

```
#!/usr/bin/env bash
echo "sync... press any key to exit"
keypress=''

while [ "x$keypress" = "x" ]; do
  # rsync add -n for dry run
  rsync -vPh --stats -a -u /path/to/remote/mount_point /path/to/local/data_folder
  sleep 10s
  keypress="`cat -v`"
done
```

transferring the data files is shown in listing 4.1. There the `rsync` command is run with the update option and is repeatedly called after 10 s breaks ensuring that only the most recent data is transferred.

4.2 Data treatment - clustering

Section 2.3 has already explained that as beta particles scatter over several of the detector's pixels a clustering algorithm that joins triggered pixels into single hits is necessary. This section talks about the MAFalda [68] software that was used for clustering timepix data and build the patterns measured by the detector.

The Medipix Analysis Framework, MAFalda, is a C++ framework based on ROOT [69]. The framework was made in a modular way, in it several modules can be connected in order to build user applications for specific needs. In the emission channeling application the module used was the `BlobsFinder` which identifies clusters in each frame by searching for neighbouring activated pixels. The clustering was set to allow a discontinuity of up to 3 non-activated pixels in the cluster so as not to over-count hits located near masked pixels. From the clusters, the channeling pattern is built by increasing by one count a histogram bin at the geometrical center of the cluster. In MAFalda the histogram bins are defined with the same mesh as the detector pixels.

The data treatment of the measurement files with the MAFalda framework is always done in two steps. The first step is to convert the input file into a root file format with a secondary program called `mpxdataconverter`. The second is to run the MAFalda user application over the converted data file.

Converting the data to a root format has the advantage of being more compact than a text file and easier to handle within root. Although for this particular case, where a fast feedback from the measurement was necessary, it is seen as a cumbersome step. Furthermore, as a new root file needs to be made at each update of the measurement pattern, at later stages of lengthy measurements when the

amount of data becomes significant it can take a considerable amount of time just to convert the data.

Since the MAFalda application accounts for most of the data treatment time, for the purpose of monitoring experiments this process was sped up by modifying MAFalda to store at the end of each analysis the frame number and the status of the two dimensional (2D) channeling histogram. After which, an added option of continuing the analysis from the previous point could be used. Despite this, the data treatment step continued to be slow as `mpxdataconverter` always had to be run over all the data from the start.

As more and more groups start using the medipix detectors new tools are being developed that could be useful for emission channeling. Even though MAFalda was the best option at the time it has lately seen a stop in development. As a consequence it is my belief and suggestion that future Emission Channeling (EC) projects should consider other data treatment options or even the development of their own software.

Another reason why alternative software might be adopted is that clustering with timepix3 data needs to be done in a slightly different manner. This is because in the timepix3 hit data output is in a continuous stream with a time stamp per activated pixel, instead of frames. In this situation, the clustering algorithm needs to distinguish hits by both location and time.

4.3 Data analysis - PyFDD software

PyFDD [70, 71] was developed to avoid the simplifications used in the FDD fit methodology, which severely limit its use for measurements with small numbers of counts per pixel and also distort the statistical significance of the results (see section 3.2). At the same time PyFDD brought many changes in the usability that users were accustomed to in FDD. One of the main changes is that PyFDD is a python library, this means that there is no Graphical User Interface (GUI) and that in order to use it the user needs to code a fitting application in python. PyFDD helps by making this process much simpler, in fact it can be done in just a few lines of code.

The main reason for having PyFDD as a library instead of an application with GUI is that making a GUI takes time, but other reasons exist. One reason is that this simplifies and speeds up the process of adding and testing new functionalities as it does not require an update and bug checks to a GUI. Another reason is that by having users have a closer contact with the code it is hoped that it will be easier for anyone to change it and contribute to its development. This is also the reason why PyFDD was developed in Python, a presently popular language, and why its code is publicly distributed.

Figure 4.1 shows the PyFDD class dependency tree and gives a short description for each of them. The structure is quite simple. On the left side of the figure there is the measurement side composed by the `DataPattern` class, which holds the channeling pattern and has all the respective manipulation meth-

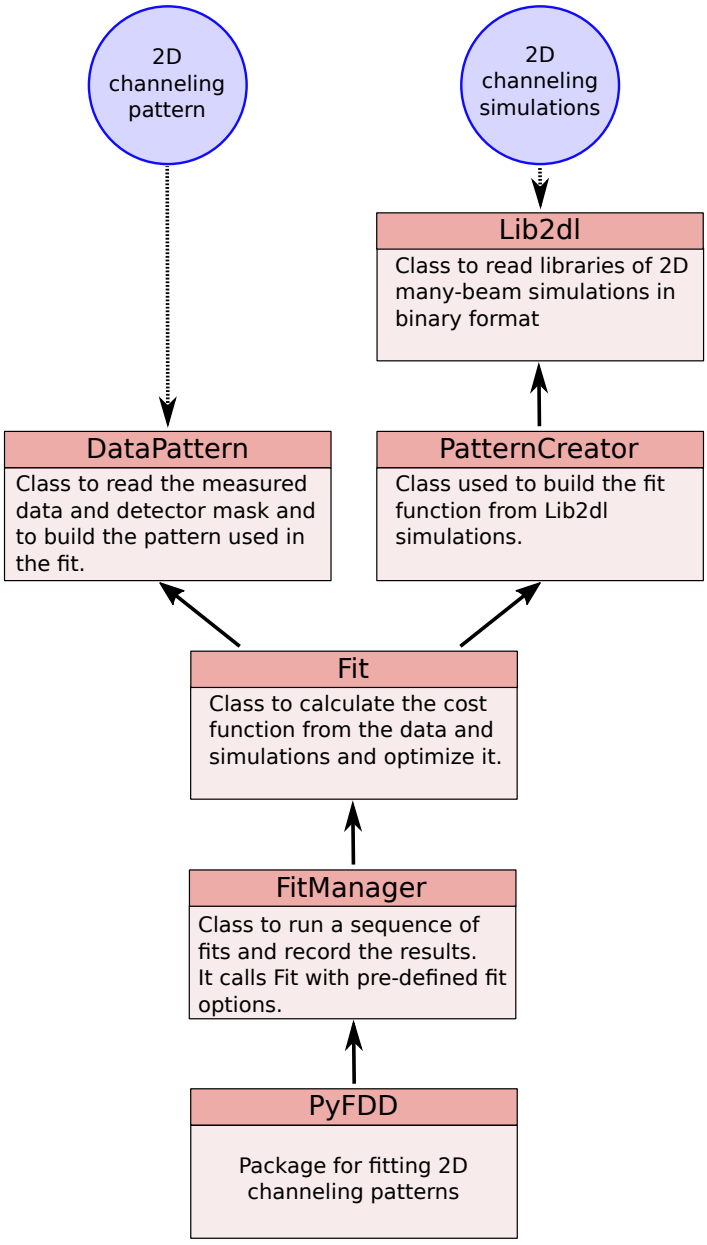

Figure 4.1: Schematics of the main classes of PyFDD and their dependencies. PyFDD class structure has been made in order to increase modularity and facilitate further development, either for integration in other projects or for the development of a GUI application. In a normal data analysis case the user only needs to interact with the DataPattern and the FitManager classes.

ods. On the right of the figure there is the simulation side composed by the `Lib2dl` and `PatternCreator` classes, which read the simulation library files and produce the probability density function (p.d.f.) for the fit. The `Fit` class calculates and optimizes the chi-square and maximum likelihood cost functions. The `FitManager` class, provides a simpler way for the user to interact with the `Fit` class, it holds the default parameter values, has built-in loops over site combinations and saves the fit outputs in a well organized .csv file.

This section will explain the main classes of the software and go through their main functionalities. At the same time, key examples are given on how the library can be used. Additional complete examples can be found in the examples folder of the software package [71].

4.3.1 DataPattern class

The `DataPattern` was the first class to be developed, still when PyFDD was not a project for fitting of these experimental patterns. The objective was to put together a set of tools necessary to work with timepix patterns and to visualize them easily. Now, the `DataPattern` class is made to hold the two dimensional (2D) experimental channeling patterns. Its main data objects are a data matrix which is a 2D histogram of the number of counts, a mask matrix that has the role of holding masked bins (masked due to hardware or fit angular range selection) and two matrices of X and Y angular coordinates that define the angular location of each bin.

Here are some of the features that can be found in the `DataPattern` class. One is a function to rotate and mirror the pattern, which is used to visualize the pattern as seen by the detector. For correctly orienting the sample towards the detector it is essential to know in which direction the goniometer that is holding the sample needs to be rotated so that the channeling effect is well positioned with respect to the detector. Another feature, this time specific for the use of timepix-quad detectors, is to correct the size of the pixels that stand between the 4 chips, as these have 3 times the size of than a standard pixel. The mask matrix and mask related functions are also included in the `DataPattern` class, these are responsible for setting the mask, masking pixels based on the chosen area to fit and, optionally, masking pixels whose number of counts deviates more than an adjustable value from the normal distribution of counts in the pattern. Furthermore `DataPattern` objects can be added together, subtracted or multiplied by a scalar.

An additional important feature of the `DataPattern` class is the function too add adjacent pixels. Using each of the detector's pixels as a histogram bin might result in the number of counts per bin being too low to enable a chi-square fit. Maximum likelihood is a good option for those cases, but if the user prefers a chi-square statistic and can accept a loss in angular resolution, adding pixels together is a good solution. This process is done by following some pre-set rules for which awareness is recommended. When pixels are added, the coordinates of the new larger bin are updated accordingly. If one of the

original pixels composing the large bin is masked, then the final bin will also be masked. When the pattern matrix can not be divided to have an integer number of pixels in each bin, any remaining pixels at the edges of the pattern are removed. Also, the distribution of bin boundaries is chosen so that the number of pixels to be masked in between the timepix-quad chips is kept at a minimum.

Finally the `DataPattern` class is used to set starting values for the fit parameters $(\Delta x, \Delta y, \phi)$ that define the orientation of the pattern. It does this by first displaying the pattern in a smart way that automatically scales the color scale. Then a tool, similar to the one existent in FDD, allows the user to click on the pattern and input a location for the center of the channeling effect and angular orientation of the main crystal plane. Using the user orientation input, it can also set a fit region that is centred on the crystal axis and does not extend beyond the simulated area of $\pm 3°$.

An example that uses the methods here presented can be seen on listing 4.2. There the `DataPattern` creation process is explained for a channeling pattern that consists of the sum of two patterns measured with the timepix-quad detector. In this example, the two patterns are added, then the timepix pixels are added into bins with 4×4 pixels. After the user has defined the orientation of the channeling pattern a valid fit area of $\pm 2.7°$ is set around the channeling axis.

Listing 4.2: Example of a DataPattern for a timepix measurement with two EC pattern files.

```
# Import necessary libraries
import pyfdd
print('PyFDD version', pyfdd.__version__)
from ecsli_tools import load_tpxquad_mask
import matplotlib.pyplot as plt

# Input files
filename1 = "/home/user/path/to/pattern_1.txt"
filename2 = "/home/user/path/to/pattern_2.txt"

# Create DataPattern objects for each file.
# The timepix-quad has 4 chips 2 horizontal and 2 vertical
# The real size of the pixels between chips is of 3 standard pixels
dp1 = pyfdd.DataPattern(file_path=filename1, nChipsX=2, nChipsY=2, real_size=3)
dp2 = pyfdd.DataPattern(file_path=filename2, nChipsX=2, nChipsY=2, real_size=3)
dp = dp1 + dp2

# Mask
# use of a load function specific for the timepix-quad at the ec-sli setup
mask = load_tpxquad_mask("/home/user/path/to/detector_mask.txt")
dp.set_mask(mask, expand_by=0) # Set expand by > 0 when pixels are not added
    together.

# Orient
# use 'rr','rl','mh',mv' for rotate right, rotate left, mirror horizontal and
    mirror vertical
# in the desired order
dp.manip_orient('rr,mh')  # Timepix-quad orientation

# Angular calibration
dp.manip_create_mesh(pixel_size=0.055, distance=316)

# Add extra pixels to account for bigger central pixels
dp.manip_correct_central_pix()

# Sum pixels (factor), zero central pixels and remove edge pixels
dp.manip_compress(factor=4, rm_central_pix=2, rm_edge_pix=4)

# Set the angular orientation for the pattern
fg = plt.figure()
ax = fg.add_subplot('111')
dp.draw(ax, percentiles=(0.04, 0.99)) # Set percentiles to automatically set the
    visualization color scale
dp.get_angle_tool() # Tool for user input
plt.show()

# Set fit range centred on the channeling axis user input location and aligned to
     the angular orientation of the main crystal plane
```

```
dp.set_fit_region(distance=2.7)
# Save
dp.io_save_json('/path/to/datapattern.json')
```

4.3.2 PatternCreator class

The `PatternCreator` class is responsible for building the fit p.d.f. using the mathematical formulations described in section 3.2. In this process, it needs to have information about the angular positions of the detector pixels, the mask of the `DataPattern` in use and many-beam simulation patterns. The simulation patterns are stored in a custom binary file, with extension .2dl, that can be accessed with the use of the `Lib2dl` class.

A new pattern can be created by giving the following inputs: the index of the lattice site patterns and corresponding fractions; the integral value of pattern in number of events; the values for the translational and rotational orientation and, optionally, the value for the standard deviation of the Gaussian smoothing.

The pattern creating process has four parts. The first, is the construction of a pattern from a linear combination of yield simulations according to the mathematical formulations described in section 3.2 up to the pattern normalization step. The second, is the update of the detector pixel coordinate mesh by translational and rotational operations. The third step, is the interpolation of pattern values for the new coordinates of the detector pixels. The final step is to set the pattern integral, that can be 1, in the case of the pattern being a p.d.f., or the total number of counts.

If the bins of the pattern have a solid angle large enough so that it is erroneous to consider that the simulation is constant over the bin area, then, before the pixel coordinate updates and respective interpolation of the simulation to the pixel positions, the coordinate mesh is expanded into smaller sized virtual bins called sub-pixels. After which, simulated pattern values are interpolated for each sub-pixel location, these are then averaged to give a simulation value to the original bin.

There are two options that were added to the class, initially with the purpose of testing the software but whose usefulness might go beyond its original purpose. These options are to use the simulated pattern to emulate a realistic experimental pattern with the expected noise fluctuations. One of the methods generates events on the pixel matrix with the method of Monte Carlo where each pixel probability of being hit by a particle is given by the pattern p.d.f.. The other method, which is faster and equally accurate when the counts per pixel are large, is to calculate a pattern with the intended total counts and give a Poisson noise to each of the pixel values. Note that the latter method also has random contribution to the total number of counts. Fig. 4.2 shows three of the four possible pattern generation types (except for the p.d.f. type) for a ^{24}Na in GaN simulation along the $[0\,0\,0\,1]$ direction.

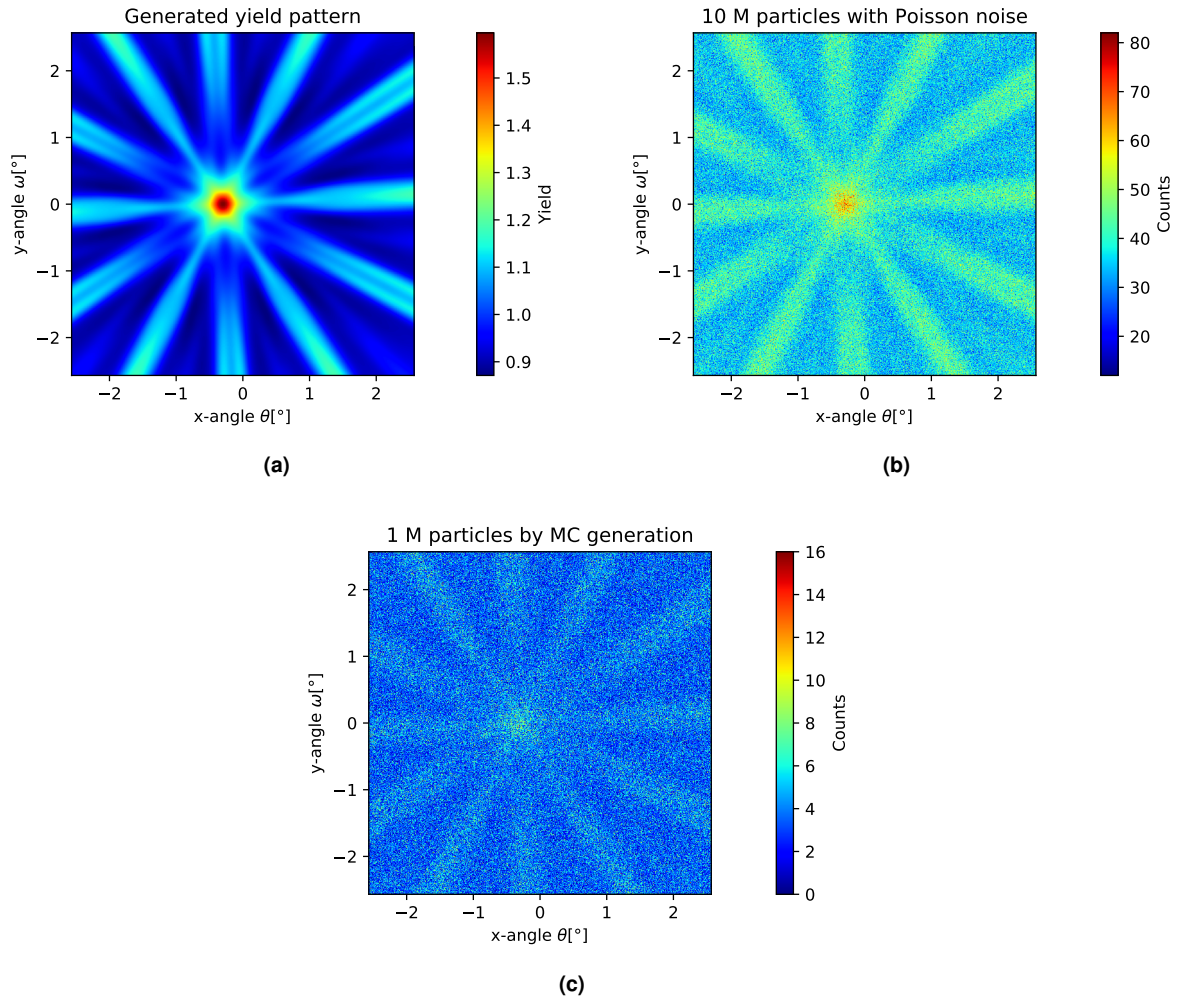

Figure 4.2: Three types of patterns generated by the `PatternCreator` class for a ^{24}Na in GaN simulation along the $[0\,0\,0\,1]$ direction. Panel a) shows the yield pattern and panels b) and c) show the same pattern for a hypothetical measurement with 10 M and 1 M counts respectively. The panel b) pattern has a simulated Poisson noise per pixel and in panel c) the 1 M were distributed over all pixels according to the p.d.f. by Monte Carlo. The patterns were generated for a Ga substitutional site with 50 % occupancy and with a small offset in the orientation. The detector considered was a timepix-quad detector.

4.3.3 Fit class

The Fit class uses a `DataPattern` object as the measured pattern and a simulation pattern given by a `PatternCreator` object to calculate the cost function. The cost function can either be from chi-square or a negative log likelihood statistic, the minimization of which optimizes the fit parameters.

The chosen minimization algorithm for the fit is the L-BFGS-B from the SciPy python library [72, 73] which uses a limited memory (L) and bounded (B) version of the Broyden-Fletcher-Goldfarb-Shanno (BFGS) algorithm. This algorithm was chosen for being easy to install along with the other used python libraries, for allowing for bounded variables, which is useful to keep fractions always positive, and be-

cause it gave coherent results. One disadvantage of this algorithm is that it does not accurately calculate the Hessian matrix, which is required for calculating the parameter uncertainties after the fit. For this reason the Hessian matrix is calculated separately after the fit.

Another option for the minimization method was the Minuit algorithm [74] from ROOT. Even though the algorithm exists in a python library [75] and has the necessary features for the present case, it was not pursued as an option in order to keep a reduced number of dependencies.

During the fit, the function parameters $(f_1, f_2, f_3, \Delta x, \Delta y, \phi, \sigma, n_{total})$ are optimized in an iterative process. The BFGS algorithm does this process in a similar way to gradient descent but instead of doing a step in the gradient direction that is proportional to the gradient modulus, it will do a line search along the gradient direction that starts with a step size of 1 and is optimized in a few iterations. While a step of 1 might be an acceptable step for the optimization of ϕ, which is an angular value in degrees, ranged from –180° to 180°, it is too small or too big for optimizing other variables. For example, it is too small for N_{cts} which is the total number of event with an order of magnitude around 10^6, and too large for optimizing the fractions f_1, f_2, f_3 whose values range from 0 to 1. In order to have each variable have an adequate step size, the fit class gives the option to scale the variables. Using good values in the scale option settings also has the advantage of simplifying the fit, this can drastically reduce the number of required iterations and make the fit much faster.

The Fit class also works as an interface for the minimization routine configuration, in this case, Scipy L-BFGS-B. Out of the available options the parameters that are worth mentioning are `maxiter`, `maxfun`, `ftol` and `eps`. The `maxiter` parameter is the maximum number of iterations that the algorithm can do and `maxfun` is the maximum number of function calls, i.e., to the chi-square or the log likelihood functions. The `ftol` parameter is a threshold that defines when a fit is successful and stops optimization. A too high value of `ftol` can lead to a non-optimum solution and add some noise in the results, a too low value can make the fit too long to run and in some cases enter an infinite loop (due to a bug it seems that the infinite loop can not always be avoided by limiting the number of iterations). The `eps` parameter is the step that will be used to calculate the gradient, there should not be any need to change this value unless the scale values are significantly changed.

Initial values are an important input to avoid local minima of the cost function and produce a fast and accurate fit. The fit class has methods for setting the initial values as well as to keep them fixed during the fit. Sometimes, when the fit results are very close to the initial values it can be a good test to change the initial values and see if the results are the same.

At last, the Fit class also has the methods necessary to calculate the Hessian matrix and with it the parameter uncertainties.

4.3.4 FitManager class

Due to its complexity the Fit class is not meant to be used directly, instead it should be accessed via the `FitManager` class, which simplifies the whole analysis process. A major part of the simplification process is about having tested default values in the various options and parameters available in the `Fit` class. The `FitManager` uses the `DataPattern` orientation and counts to set the fit initial values. It also has robust default values for the function parameters scale (also called step modifiers) that were optimized for fit accuracy and speed. At last it has a set of predefined profiles, “coarse”, “default” and “fine”, to easily set the minimization algorithm parameters with increasing precision.

The `FitManager` class also provides the methods to easily run a fit for a linear combination of any number of sites (in most cases only one or two sites are considered, occasionally three), or for sequences of fits that run through a loop that inludes a range of sites. Results from the fit are saved into a pandas DataFrame [76] which can then be exported to a .csv or excel file for an easy visualization of the results. Furthermore, resulting fit patterns can be retrieved into a `DataPattern` object that can then be exported or plotted.

The listing 4.3 shows an example of the use of the `FitManager` class for the fit of a channeling measurement using a chi-square cost function, a combination of 2 lattice sites and 2 sub-pixels. The resolution sigma is fixed at 0.05°, and the minimization profile is set to “fine”. The fit manager will do a sequence of fits with the first site kept fixed at the site #1 and the second site will be scanned from the site #1 to site #248. The script ends with saving the fit results and the resultant best fit pattern.

Listing 4.3: Fit of a range of sites with FitManager example.

```
filename = /path/to/datapattern.json
libraryname = /path/to/library.2dl
savename = /path/to/savefile.csv

# To initiate the fitmanager define, the cost function, the number of sites and
    the number of subpixels
fm = pyfdd.FitManager(cost_function='chi2', n_sites=2, sub_pixels=2)

# Set the pattern and library to fit with
fm.set_pattern(filename, library)

# Set a fixed value if needed
fm.set_fixed_values(sigma=0.05)

# Set a minimization profile
fm.set_minimization_settings(profile='fine')

# Set a pattern or range of patterns to fit
P1 = np.array([1])    # single site
P2 = np.arange(1,249) # range - one more than the last

# Run fits
fm.run_fits(P1, P2, get_errors=True)

# Save the results
fm.save_output(save_name)

# Save the best fit pattern
dp_bestfit = fm.get_pattern_from_best_fit(normalization='yield')
dp_bestfit.io_save_json('/path/to/bestfitpattern_yield.json')
```

5

Measurements of Lattice Locations of Implanted Radioactive Probes with the Pad and Timepix Detectors

Chapter 5 is a compilation of a series of emission channeling measurements of different radioactive isotopes implanted in gallium nitride, GaN, and respective lattice location analysis. Here, results obtained from data taken with the timepix detector are shown together with a comparative analysis of data taken with the pad detector. In addition to the lattice location studies, this chapter also presents insights on the analysis methods learned from the use of high angular resolution channeling measurements and the use of the PyFDD software for the analysis.

GaN was chosen as the case study for testing the detectors for the following reasons; it is easily available as good quality single-crystalline films, it is able to withstand comparably high implantation fluences without the accumulation of excessive radiation damage, it has both technical applications as well as scientific interest, and there exist older emission channeling data and analysis that can be used

for comparison.

GaN has a wurtzite crystal structure. Fig. 5.1 shows a cut along the major lattice plane $[1\,1\,\bar{2}\,0]$ of GaN which indicates the substitutional and major interstitial sites. For future reference along this chapter the site naming convention will be used as it is indicated in the figure.

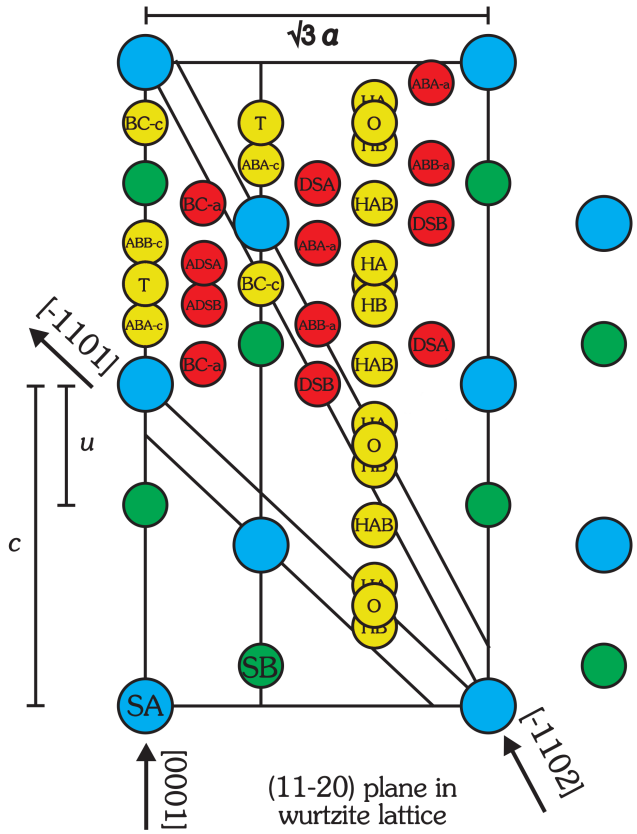

Figure 5.1: Schematics of lattice sites in GaN considered in simulations. Each site is represented with a short identification. SA and SB are the substitutional sites for Ga and N respectively, BC-c and BC-a are bond-centered sites along and off the c axis, ABA and ABB are anti-bonding sites, DSA, ADSA, DSB and ADSB are displaced sites from SA or SB. T and O are the wide open interstitial positions along and parallel to the c-axis, while HA, HB and HAB are "hexagonal" sites obtained by displacements from O sites parallel to the c-axis.

5.1 ^{43}K in gallium nitride

Potassium doping of GaN does not have any particular technical application, however, from a scientific point of view it is interesting to compare its properties with neighbouring elements of the groups 1 and 2 of the periodic table. In that respect a recently published manuscript [77] addressed the emission chan-

neling lattice location results of light alkalis and alkaline earths in GaN and AlN. It is hence interesting to see how K fits into the reported trend that Be, Li, Na, and Mg are amphoteric impurities in GaN, i.e. able to occupy both substitutional Ga and interstitial sites, while Ca and Sr are only found on substitutional Ga sites. The low ionization energy of K makes it an easily available radioactive beam at ISOLDE as it does not need to be ionized with lasers. Additionally, ^{43}K has a relatively long half life of 22.3 h, which allows the collection of sufficiently large amounts of probes without having radiation saturating the detector readout. The beta decay of ^{43}K has an average energy of 317 keV which should cause wide angular channeling effects that can be well detected even with large pixel detectors. This factors caused that the emission channeling measurements of ^{43}K in gallium nitride were an opportunity for comparing data taken with the pad and the timepix detector in an experiment where all relevant crystallographic directions were measured with both detectors for several annealing steps.

As the intent was to compare detectors, in order to avoid having uncertainties that could arise from different samples or different implantations, the measurements were performed simultaneously with both the pad and the timepix detectors. In order to enable the use of a chi-square analysis with the pad and with the full pixel mesh of the timepix detector, each channeling pattern was taken with a high number of events, avoiding in this way the use of different analysis methods for each detector or the summing of adjacent pixels on the timepix patterns. Moreover, the long decay half life gave the opportunity to perform the experiment with a single initial implantation meaning that the sample damage was not further increased at any point in the process.

The experiment was done in the implantation chamber with the pad detector sitting at an angle of 17° with the beam direction and the timepix-quad at –30° (see Fig. 2.2). The details of the implantations are compiled in table 5.1 for sample #472. The position of the detectors is fixed by the chamber geometry but the 47° angle between the two detectors was an unexpected advantage as it allowed the simultaneous measurement of the $[\bar{1}\,1\,0\,1]$ axis by the timepix detector and of the $[0\,0\,0\,1]$ axis by the pad detector, in this way saving some time. The detectors were placed at about 32 cm from the sample according to the distances detailed in table 3.1.

After implantation, the $[0\,0\,0\,1]$, $[\bar{1}\,1\,0\,1]$, $[\bar{1}\,1\,0\,2]$ and $[\bar{2}\,1\,1\,3]$ axes were measured in the Room Temperature (RT) as-implanted state and again after 10 min annealing at 150 °C, 300 °C, 450 °C, 600 °C, 750 °C and 900 °C. Since it takes less time to make a pattern with the pad, due to its higher count-rate and not needing high statistics, all axes were measured at each of the annealing steps with the pad detector, on the other hand, with the timepix detector patterns were only produced for the annealing steps at 300 °C, 600 °C and 900 °C. The pad patterns were taken with about 1 M counts and the timepix patterns with about 6 M counts, this allowed sufficient counts per pixel for enabling a chi-square analysis also with the timepix detector data.

The lattice site analysis was performed by chi-square minimization with the PyFDD software. Ac-

cording to the methods previously described, at first the channeling patterns were oriented and a fit range of 2.7° centered around the channeling axis was set. In the timepix patterns, in order to use the best angular resolution available, pixels were not added together. For the fit of both the pad and timepix pattern, the sigma value for the Gaussian convolution was kept fixed at 0.050° which corresponds to the expected angular resolution due to the size of the beam spot without taking into account the detector's pixel size. The simulation values for the larger pixels of the pad detector were averaged over the pixel area using a 6 $\times$ 6 sub-pixel mesh. At last, the total number of counts in the expected patterns for each site was not optimized in the fit and kept equal to the total number of events in the data pattern.

The approach taken to identify the occupied sites started with single site fits for each of the possible sites and looking at the resulting chi-square. This analysis returned a couple of local minima on sites with small displacements from the Ga substitutional, namely from the Ga substitutional towards the bond centered (c-axis) site, the bond centered (a-axis) site and the anti-bonding (a-axis) site. However, results from the four different axes measured were not consistently pointing to one specific displacement, therefore no such displacement could be identified with certainty and a different approach was adopted.

The next trial was to do the fits including a higher number of sites. In this process several combinations of displaced sites around the Ga substitutional were tested. The fit results for all the axes did not show a coherent combination of displacements, with some channeling directions always favouring one of the displacements over the other. The compromise to this uncertainty was to consider that the impurity is in a modified Ga substitutional site with a larger site root mean square (rms) displacement u_1.

The common practice is to initially assume that the rms of the probe atom is close to the u_1 of the host atoms assumed in the simulations, for which the values $u_1(Ga) = 0.0589$ Å and $u_1(N) = 0.0656$ Å [78] were used. With this method the calculated patterns assume an ensemble of ^{43}K sites, around the SGa site, with a Gaussian probability distribution of standard deviation u_1 along each of the 3-dimensional axes. The resulting patterns from the measurements in the room temperature as-implanted state can be seen in Fig. 5.2 and 5.3.

The impurity rms displacement can not be optimized by the fit routine, for this reason simulations using higher $u_1(^{43}\mathrm{K})$ values are included in the simulation libraries. In this case, the included simulations for the SGa site use values of u_1 ranging from 0.05 Å to 0.24 Å in steps of 0.01 Å. Fig. 5.4 shows the u_1 values for the ^{43}K impurity on SGa sites following several annealing temperatures obtained from the analysis of the timepix and pad detector data. Both detectors show $u_1(^{43}\mathrm{K})$ around $0.15(4)$ Å after implantation and a reduction to around $0.12(3)$ Å after annealing at 300 °C.

Fig. 5.5 shows the site occupancy for the same measurements. It can be seen that the occupancy fraction is fairly constant with increasing annealing temperature. The fractions derived from the analysis do not reach 100 %, for which there are several possible reasons: implantation damage which remains

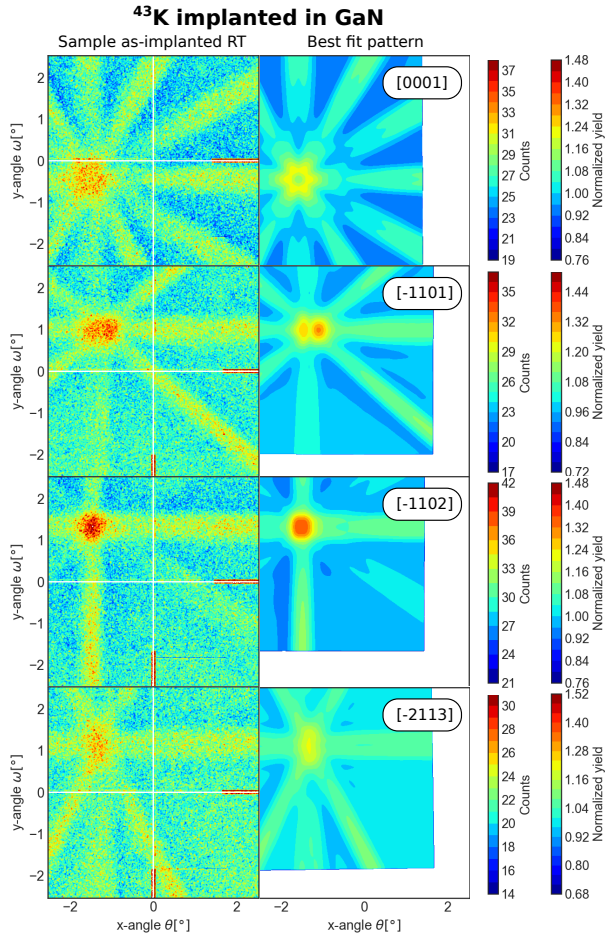

Figure 5.2: Timepix-quad detector measured patterns of ^{43}K implanted in GaN, on the left, together with the best fit patterns for the $[0\,0\,0\,1]$, $[\bar{1}\,1\,0\,1]$, $[\bar{1}\,1\,0\,2]$ and $[\bar{2}\,1\,1\,3]$ axes, on the right. The best fit patterns are built from simulations in accordance to the detector pixel mesh and resolution. The normalized yield color scales have been calculated from the simulated yields of the fitted sites. White areas in the plots represent points for which there is no simulation or measured data. The central crosses of white pixels on the timepix detector correspond to the masked pixels at the edge of the four timepix chips.

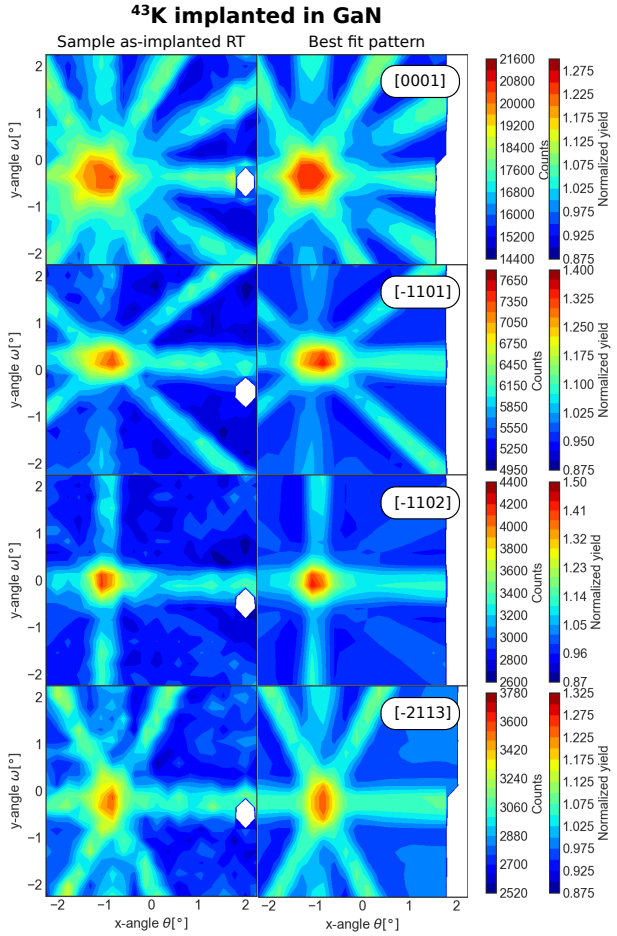

Figure 5.3: Pad detector measured channeling patterns of ^{43}K implanted in GaN, on the left, together with the best fit patterns for the $[0\,0\,0\,1]$, $[\bar{1}\,1\,0\,1]$, $[\bar{1}\,1\,0\,2]$ and $[\bar{2}\,1\,1\,3]$ axes, on the right. The best fit patterns are built from simulations in accordance to the detector pixel mesh and resolution. The normalized yield color scales have been calculated from the simulated yields of the fitted sites. White areas in the plots represent points for which there is no simulation or measured data.

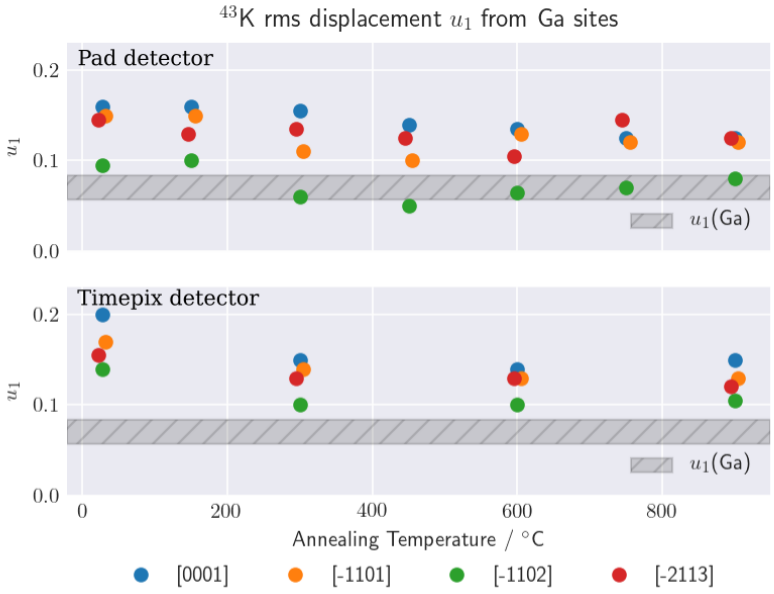

Figure 5.4: ^{43}K rms displacement u_1 from Ga sites as a function of annealing temperature following RT implantation. Potassium occupies a range of sites around the Ga substitutional site that can not be resolved and are therefore here summarized as a Ga substitutional site with a higher u_1. Both measurements show a small reduction of u_1 after annealing at 300 °C. The shaded area in the plots indicates the thermal vibration amplitude of Ga according to literature values, which range from 0.057 Å to 0.084 Å.

unannealed in the sample, an underestimation of the correction for scattered electrons, or the possibility that there exist additional lattice sites of K that could not be resolved by the analysis.

With the interest in further testing the effect of improving the angular resolution, this experiment was later repeated using a beam collimator of 0.4 mm in diameter. The measurement was made with the timepix-quad detector and using a different sample (#330 Montpellier) at RT. Results for this sample showed slightly higher values of u_1, having $u_1 = 0.25$ Å for the direction $[0\,0\,0\,1]$, $u_1 = 0.2$ Å for the direction $[\bar{1}\,1\,0\,1]$, $u_1 = 0.17$ Å for the direction $[\bar{1}\,1\,0\,2]$, $u_1 = 0.21$ Å for the direction $[\bar{2}\,1\,1\,3]$. From this test no significant improvement in the channeling was seen due to the better angular resolution, however the higher values for u_1 might be a consequence of increased implanted damage since a relatively high fluence was implanted into the small beam spot.

The decrease of u_1 with the annealing temperature is hard to identify by eye from the channeling patterns and little insight can be given by showing the initial and final patterns. Alternatively, in order to provide some understanding of the influence of u_1 on the channeling effect, simulations of the yield at $u_1 = 0.06$ Å and $u_1 = 0.18$ Å as seen by each detector are shown in Fig. 5.6. From these simulations it is noticeable that the rms has a strong effect on the axial channeling but a weak effect on the planar channeling. As is seen, the lower angular resolution of the pad detector leads to a considerable modification of the pattern, however, this fact by itself does not imply that the precision with which the fraction or the

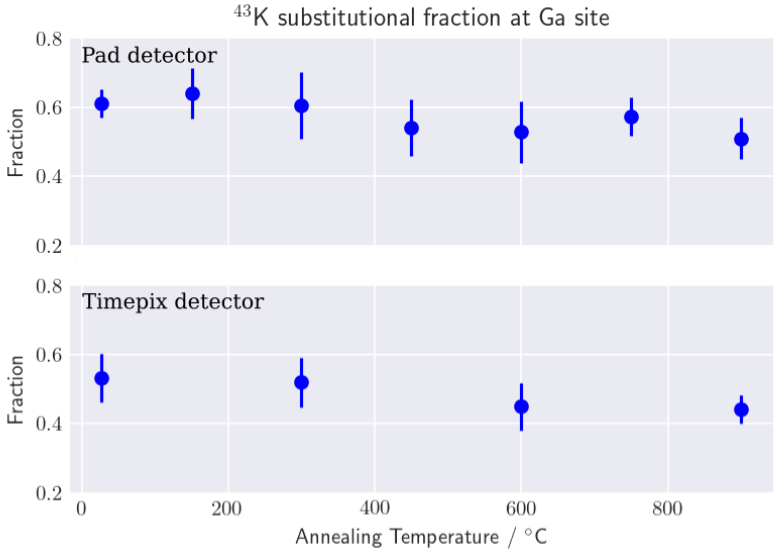

Figure 5.5: Ga site occupancy fraction of ^{43}K implanted in GaN. The data points are the average of the four measured directions and error bars are represented as the largest deviation from the average of all the measured directions. The measurements done with the pad show a higher fraction than the ones done with the timepix ($\approx +10\,\%$), a possible cause for the effect can be that the gamma background can not be correctly characterized simply by blocking the beta radiation with the detector valve.

rms displacement can be quantified is much reduced. In fact, since this effect is taken into account by the fit software, the effect is mitigated.

The results of the two detectors are largely in agreement with just some small differences present, namely, both a higher fraction ($\approx +10\,\%$) and a lower u_1 value at RT ($\approx -17\,\%$) for the pad measurements. The most likely cause for the differences in the fractions is the gamma background correction. The contribution of gamma background is estimated by closing identical vacuum valves in front of the detectors. This blocks all electrons so that the remaining count-rate results from higher energy gammas that originate in the sample and pass through the valve or from gammas that reach the detector independently from the state of the valve. However, since the valves also absorb to some extent lower energy gammas, the procedure underestimates the real gamma background. The error that is made depends on the efficiency with which each detector responds to low-energy gammas; thus, if the timepix detector has a higher efficiency or a lower threshold to detect low energy gammas, this could explain the difference.

Other causes, as to what could cause the differences between the two measurements were considered but later discarded. The first being a statistical difference, which could be easily dismissed as the statistical error bars obtained by the fit are too small to explain the effect. Another cause could be the pixel size, in order to test this hypothesis the same analysis was done with the timepix data but summing 24×24 pixels into super-pixels that approximate the size of the pads. In this analysis the value of the

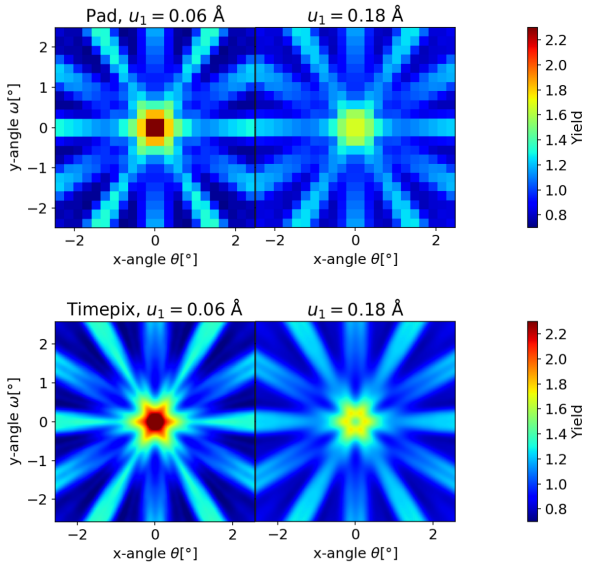

Figure 5.6: $[0\,0\,0\,1]$ channeling pattern simulation as seen by the pad and timepix detectors for $u_1 = 0.06$ Å and 0.18 Å. The figure shows that the u_1 for ^{43}K in GaN has a larger effect on the axial channeling than on the planar channeling. On the axial channeling increasing the rms of the emitter has the effect of reducing the peak and creating a ring like structure, on the other hand, the effect on planar channeling is of a smoothing nature. The ring like structure of the axial effect is a consequence of the fact that for larger rms of the emitter atoms the most tightly bound channeling states are reduced in intensity while states with larger angular momentum with respect to the axis are increasingly occupied.

sigma was kept at the previously used value and the super-pixel simulated values were calculated as the average of the simulation over its area with the same procedure that is done with the pad detector. The results of the timepix data grouped into super-pixels did not change the u_1 nor fraction results by much, indicating that the difference is not related to the pixel size. At last, it was also thought that the beta background could have an effect but GEANT4 simulations have shown that it is quite uniform in the detector's area and very similar at both detector geometries.

Conclusions on ^{43}K implanted in GaN

The easy availability of strong ^{43}K beams at ISOLDE and the convenient half life of this isotope provided an excellent opportunity to prepare samples that allowed to perform parallel lattice location studies from the same sample using both timepix and pad detectors.

Since the impurity rms displacement u_1 has a pronounced influence on the angular width of channeling effects and the same is true for the angular resolution of the measurement, the best fit u_1 parameter has a strong correlation with the sigma value of the Gaussian convolution that models the resolution. Although this is a known effect, the perception of this correlation during the analysis has highlighted the fact that it is important to know the correct value for the resolution standard deviation as well as to correctly handle large pixels by averaging the simulation data over the pixel area.

The drawbacks of the timepix detector that had an impact on the experimental process were the lower count-rate, long data processing and slow visualization feedback during the experiment. Despite the higher effort in using this kind of detectors, for this particular case, no large benefit has been seen from the high resolution measurements.

In relation to the lattice site studies it was concluded that ^{43}K occupies a Ga substitutional site in GaN and that this site is stable with annealings up to 800 °C. At the same time, there remains some disorder in the position of the ^{43}K probes around the Ga site, which is only slightly reduced by annealing, most notably around 300 °C. Overall the lattice location features of implanted ^{43}K in GaN were thus found to be quite similar to the cases of ^{45}Ca and ^{89}Sr, which were studied previously using pad detectors [79], whereas, in contrast to Li, Be, Na, and Mg (cf. [77] and sections 5.2 and 5.3), no interstitial fraction was found for K.

The comparative analysis of the two detectors has shown a good agreement between the two measurements. However, a small difference between the two results, yet above the error margin, has suggested that limits in the characterization of detector response and measured background are responsible for the deviations noted.

5.2 ^{24}Na in gallium nitride

Sodium doping of GaN, just as potassium, has its scientific interest based on the comparison of its properties with neighbouring elements of the periodic table. In effect it does not have any practical applications as a dopant despite having been in the past proposed as a candidate for being an acceptor impurity in GaN. This idea was later discarded as first principle studies have concluded that in the substitutional position sodium is not a viable acceptor [80]. From the data analysis point of view, this experiment has the capacity to provide additional insight as it is known from the literature that Na occupies a mixture of substitutional and interstitial sites, according to ref [81] these sites are occupied by 44 % and 56 % respectively and annealing at 1073 K has no effect on the fractions. As will be seen from the analysis presented here, which also forms part of recently published manuscript [77], the results of ref [81] are verified in the as-implanted state but differ after high temperature annealing.

Similarly as with the ^{43}K experiment, the channeling measurements of ^{24}Na ($t_{1/2} = 15$ h) in GaN were executed simultaneously with the two detectors and after a single implantation. ^{24}Na was implanted with a 1 mm diameter, 40 keV energy and 6.6 pA current radioactive beam at an angle of 17°, after which channeling patterns were measured along the $[0\,0\,0\,1]$, $[\bar{1}\,1\,0\,1]$, $[\bar{1}\,1\,0\,2]$ and $[\bar{2}\,1\,1\,3]$ directions. The sample was measured in the as-implanted state at Room Temperature (RT) and after a 10 min annealing at 800 °C. A compilation of the implantation details is given in table 5.1, under ^{24}Na in GaN with sample #472.

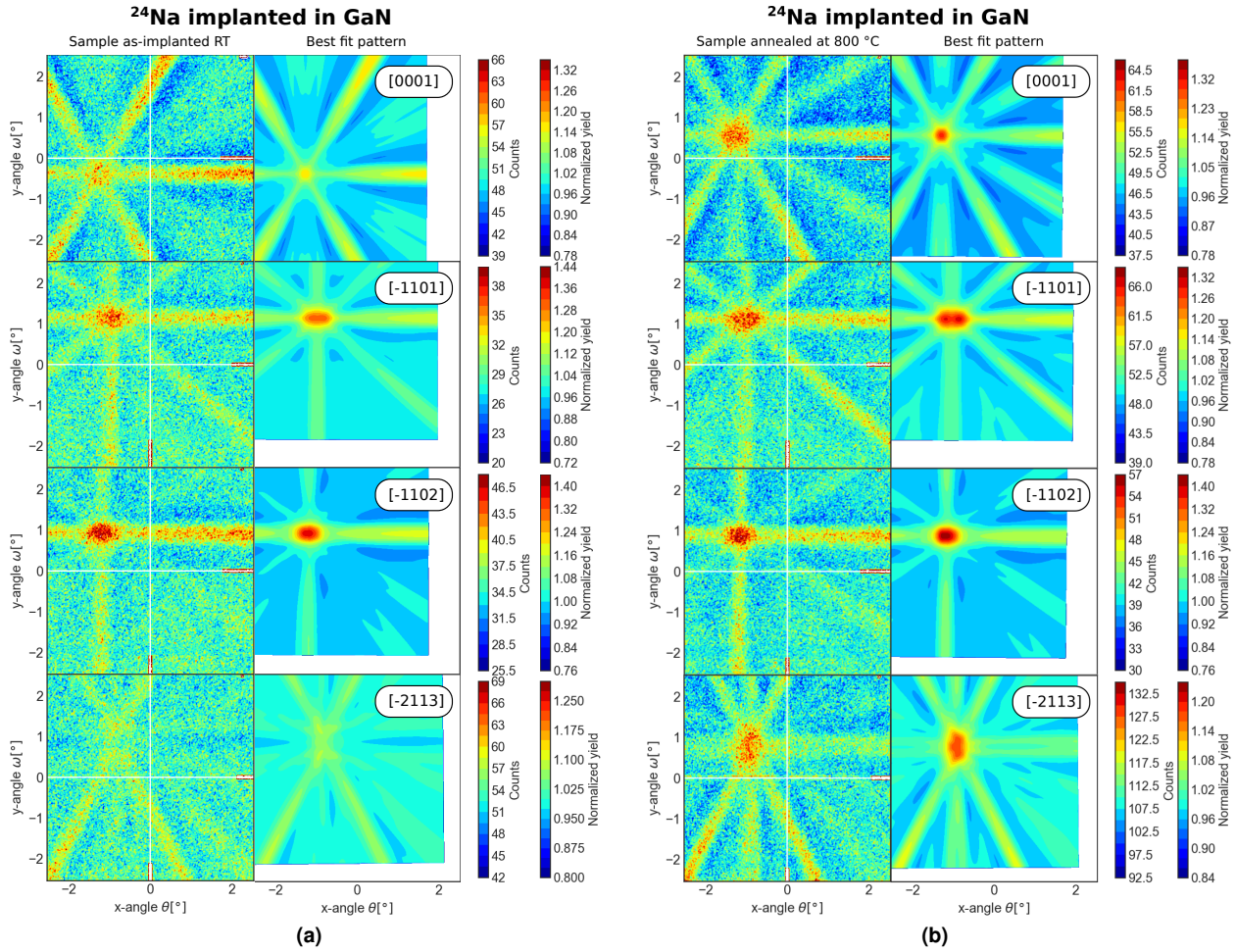

Figure 5.7: Timepix-quad detector measured channeling patterns of ^{24}Na implanted in GaN together with the best fits, for the $[0\,0\,0\,1]$, $[\bar{1}\,1\,0\,1]$, $[\bar{1}\,1\,0\,2]$ and $[\bar{2}\,1\,1\,3]$ axes. Figure (a) refers to the as-implanted measurements at 27 °C and figure (b) following annealing at 800 °C. On each pair of patterns the left one is experimental and the right one is the pattern built from simulations that best fit the data. The normalized yield color scales have been calculated from the simulated yields of the fitted sites. White areas in the plots represent points for which there is no simulation or measured data. The central crosses of white pixels on the timepix detector correspond to the masked pixels at the edge of the four timepix chips.

The patterns measured with the timepix in the RT as-implanted state had a total of 9 M, 4.7 M, 5.8 M and 9.6 M counts for the $[0\,0\,0\,1]$, $[\bar{1}\,1\,0\,1]$, $[\bar{1}\,1\,0\,2]$ and $[\bar{2}\,1\,1\,3]$ directions respectively. For the 800 °C annealed measurements of the same directions, the number of counts was 8.4 M, 8.3 M, 6.8 M and 19 M.

The analysis of the channeling patterns was performed by chi-square minimization using the PyFDD software. The simulation values for the pad detector large pixels were averaged using a 6x6 sub-pixel mesh and for the timepix the full detector pixel mesh was used without summing neighboring pixels. For both detectors an angular resolution sigma value of 0.05° was used.

The fit results were optimized by performing two-site fits where the first site was kept fixed at the substitutional Ga site while the second site was scanned over all other simulated sites, looking for improvements in chi-square that are consistent for all patterns of the four channeling directions measured. As expected, it was found that Na occupies a mixture of the Ga substitutional site and an interstitial site close to the O site. It was also found that the $[0\,0\,0\,1]$ direction presented some indication that the root mean square (rms) u_1 could be larger than expected, yet, as the opposite was also true in other directions no conclusion on the rms could be made.

Fig. 5.7 shows the timepix measurements in the RT as-implanted state and following annealing at 800 °C. In this figure, hints of a site change can be seen in the variation of the strength of the planar channeling effects. Planar channeling is the underlying effect that manifests itself by the straight lines of increased yield that cross at the axial channel in the pattern. In effect, it is noticeable that following 800 °C annealing the diagonal planar channeling shows a higher number of counts than at RT. The clearest indication of the site change, however, is visible in the $[\bar{2}\,1\,1\,3]$ pattern, where the central axial effect and the effects from the horizontal $(0\,1\,\bar{1}\,0)$ plane change from blocking to channeling following $T_A = 800$ °C. The rms u_1 ambiguity that exists in the $[0\,0\,0\,1]$ axis is also visible in the figure from the differences in the sharpness of the axial channeling between the simulation and measured patterns. More precisely, the simulation that uses $u_1 = 0.06$ has a sharp axial channeling effect while in the experimental observation the axial channeling manifests a ring like structure characteristic of higher rms vibration values.

For identification of the most probable interstitial site, two-site fits were performed where the first site was kept fixed at the Ga substitutional position, while the location of the interstitial site was sequentially moved parallel to the c-axis. The resulting variation in chi-square with the position of the interstitial site can be seen in Fig. 5.8. The average displacement from the O site amounts to $+0.02(3)$ Å for the 3 directions at RT after implantation and then to $-0.08(17)$ Å after being annealed at 800 °C.

The fractions of the best fit sites as a function of annealing can be seen in Fig. 5.9. This figure shows that the average relative site fraction for the substitutional site changes from 46(7) % at 27 °C to 76(8) % at 800 °C and the interstitial from 54(7) % to 24(8) % respectively. Additionally there is a slight reduction in the total fraction after annealing, which is possibly due to migration of the isotopes to different depths, i.e. a slight shift of the ^{24}Na profile deeper into the crystal would cause a reduction of the total fraction.

In analogy with the timepix measurements, the same crystallographic directions were also measured with the pad detector in the as-implanted state and following annealing. The pad detector patterns can be seen in Fig. 5.10. As the focus was put on the timepix detector these patterns were taken with lower statistics, having at the RT as-implanted state 4.3 M, 1 M, 0.9 M and 1.3 M counts for the $[0\,0\,0\,1]$, $[\bar{1}\,1\,0\,1]$, $[\bar{1}\,1\,0\,2]$ and $[\bar{2}\,1\,1\,3]$ axes and after annealing at 800 °C 0.9 M, 1 M, 0.5 M and 1.2 M counts for the same axes.

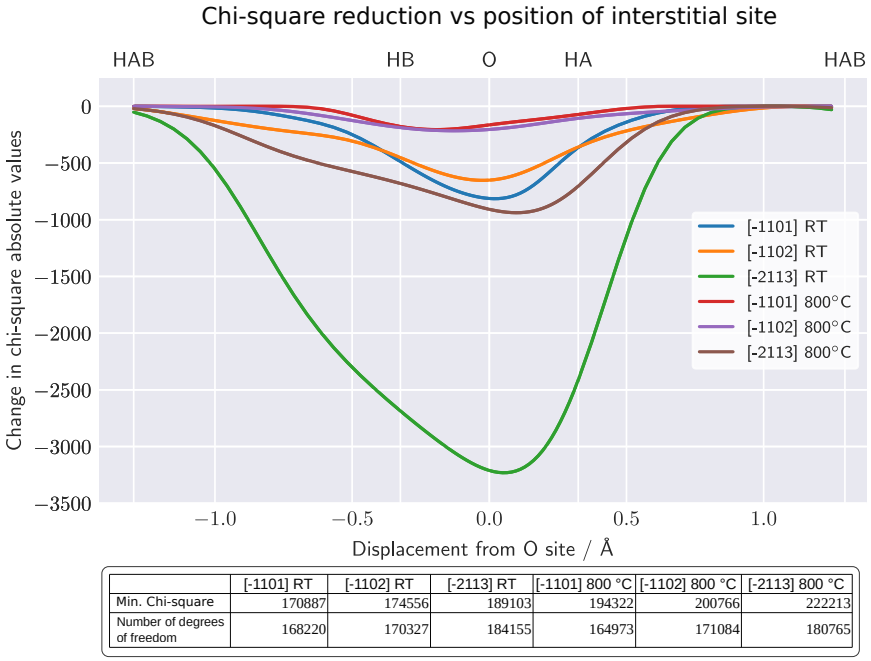

	[-1101] RT	[-1102] RT	[-2113] RT	[-1101] 800 °C	[-1102] 800 °C	[-2113] 800 °C
Min. Chi-square	170887	174556	189103	194322	200766	222213
Number of degrees of freedom	168220	170327	184155	164973	171084	180765

Figure 5.8: Identification of the most probable interstitial position of ^{24}Na in GaN from timepix detector measurements. The plot shows the change of the chi-square when in a two site fit the first site is kept fixed at the Ga substitutional position and the second, interstitial site is moved parallel to the c-axis. The most likely interstitial site is found to be close to the O site. The table at the bottom of the figure allows a comparison between the value of the chi-square with the number of degrees of freedom serving as an indicator for the goodness of fit.

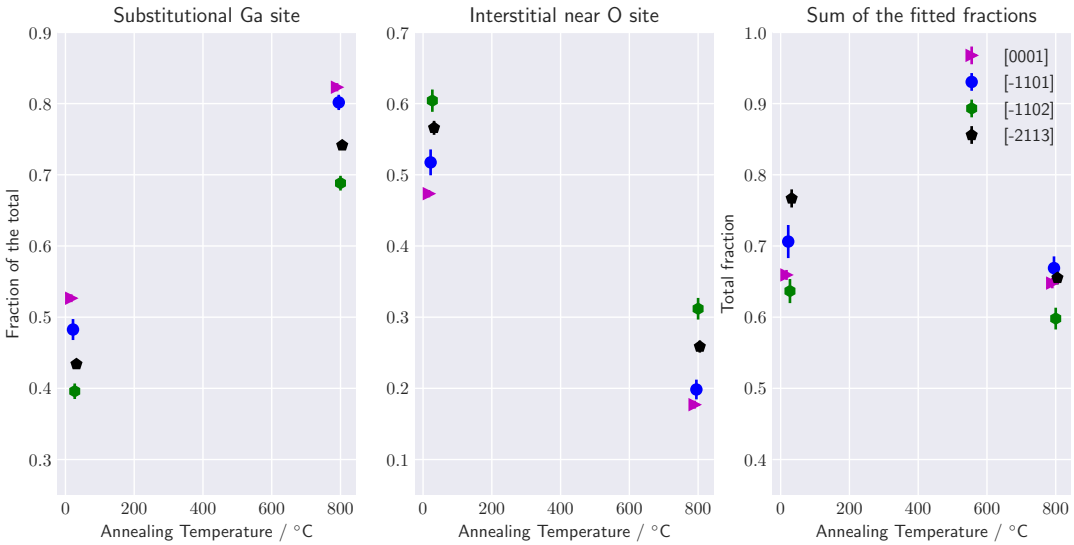

Figure 5.9: Site occupancy dependence with the annealing temperature as described from the analysis of the timepix measured data for ^{24}Na in GaN. For the two occupancy plots on the left the fractions from the fit are scaled so that the sum of the two sites is 100 %. The third plot on the right shows the total fraction obtained by the fit, followed by background correction. The sites considered are the Ga substitutional and the best fit site close to the interstitial O site.

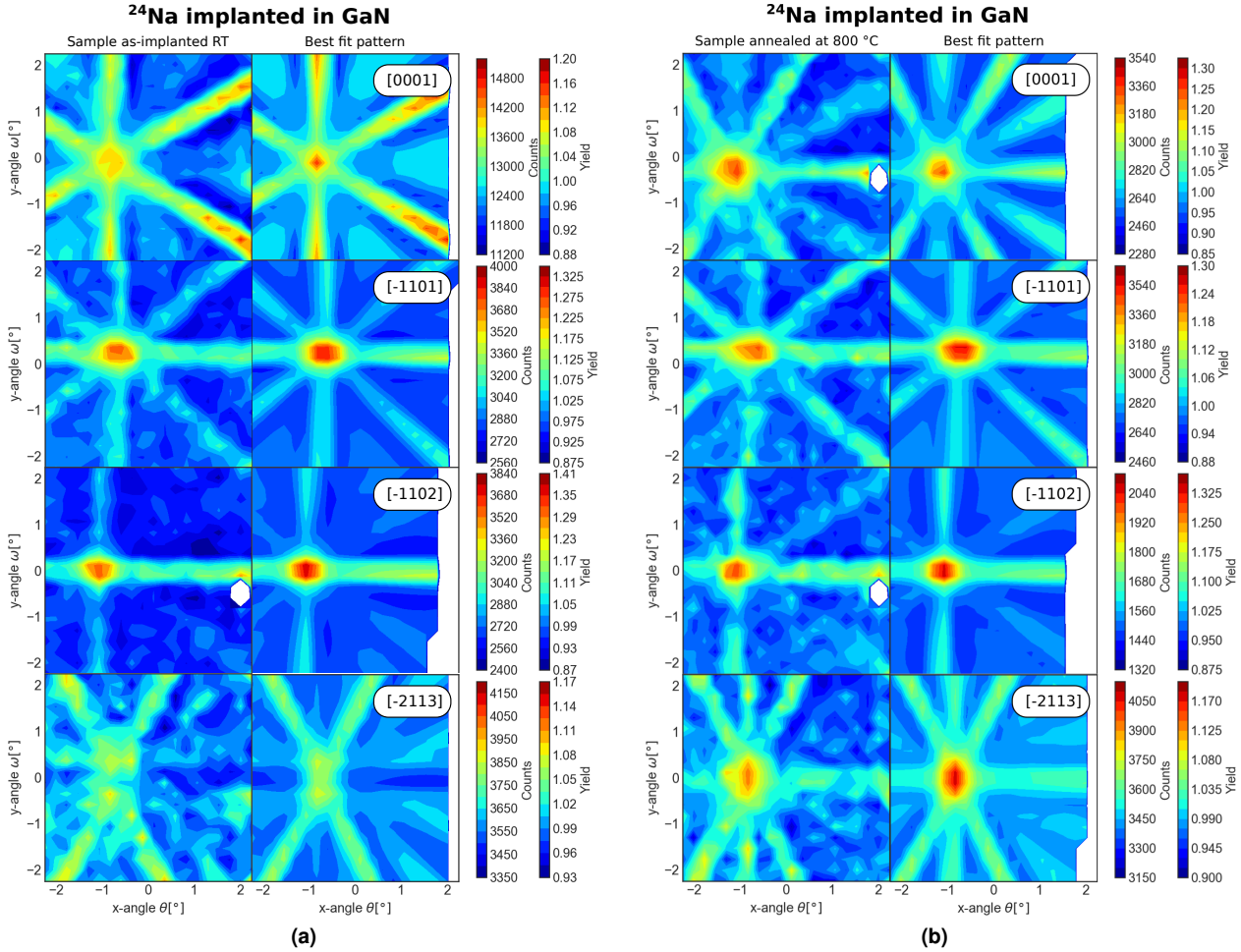

Figure 5.10: Pad detector measured channeling patterns of ^{24}Na implanted in GaN together with the best fit patterns, for the $[0\,0\,0\,1]$, $[\bar{1}\,1\,0\,1]$, $[\bar{1}\,1\,0\,2]$ and $[\bar{2}\,1\,1\,3]$ axes. Figure (a) refers to the as-implanted measurements at 27 °C and figure (b) after annealing at 800 °C. Note that in the as-implanted $[0\,0\,0\,1]$ channeling plot the sample was not yet oriented with one of the $(1\,1\,\bar{2}\,0)$ planes horizontal (as was the case for the timepix measurement shown in Fig. 5.10a). On each pair of patterns the left one is experimental and the right one is built from simulations by the fit. The normalized yield color scales have been calculated from the simulated yields of the fitted sites. White areas in the plots represent points for which there is no simulation or measured data.

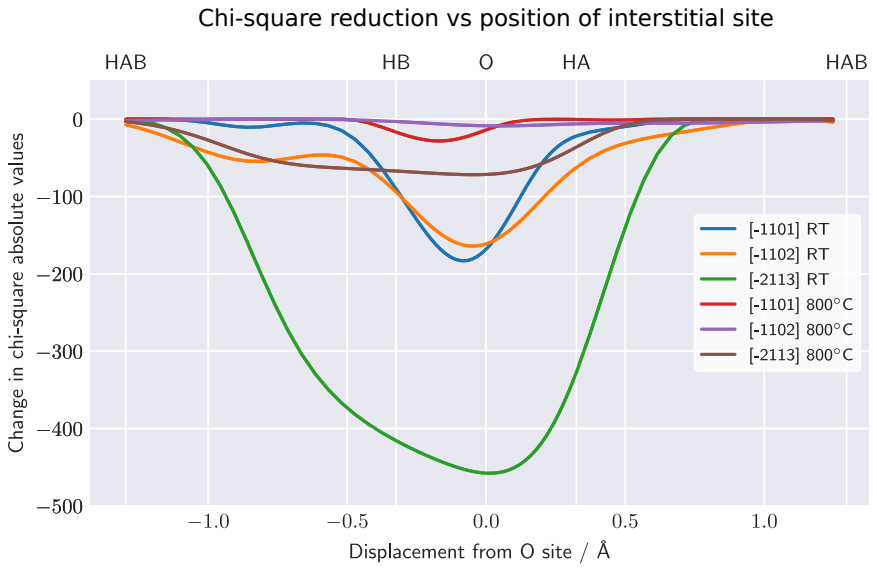

	[-1101] RT	[-1102] RT	[-2113] RT	[-1101] 800 °C	[-1102] 800 °C	[-2113] 800 °C
Min. Chi-square	677	440	473	616	413	671
Number of degrees of freedom	357	323	341	357	323	341

Figure 5.11: Identification of the most probable interstitial position of ^{24}Na in GaN from the pad detector measurements. As in Fig. 5.8 the plot shows the change in chi-square of two-site fits when moving the second, interstitial site parallel to the c-axis, while keeping the first site fixed at the Ga position. Also here the most likely interstitial site is found to be close to the O site.

Similarly as with the analysis of the timepix data, it was found that ^{24}Na occupies two sites, the Ga substitutional and an interstitial. In addition, here too there was ambiguity on the value of the rms u_1 value for the $[0\,0\,0\,1]$ axis.

The most likely position of the interstitial site was identified in the same way as with the timepix data, by looking at the chi-square of two-site fit values, one site set as the Ga substitutional and the other with a variable position parallel to the c-axis. The site identification results can be seen in Fig. 5.11. It was found that on average the best site is displaced from O by –0.04(4) Å at 27 °C and –0.05(11) Å after annealing at 800 °C.

The lattice site occupancy before and after annealing can be seen in Fig. 5.12. In the as-implanted state at RT the average relative fractions obtained were 47(7) % for the Ga substitutional site and 53(7) % for the interstitial site, then, after annealing at 800 °C the fractions changed to 76(4) % and 24(4) % for the same sites. Additionally, there are signs of probe atom migration in the sample as the total fraction reduces with annealing.

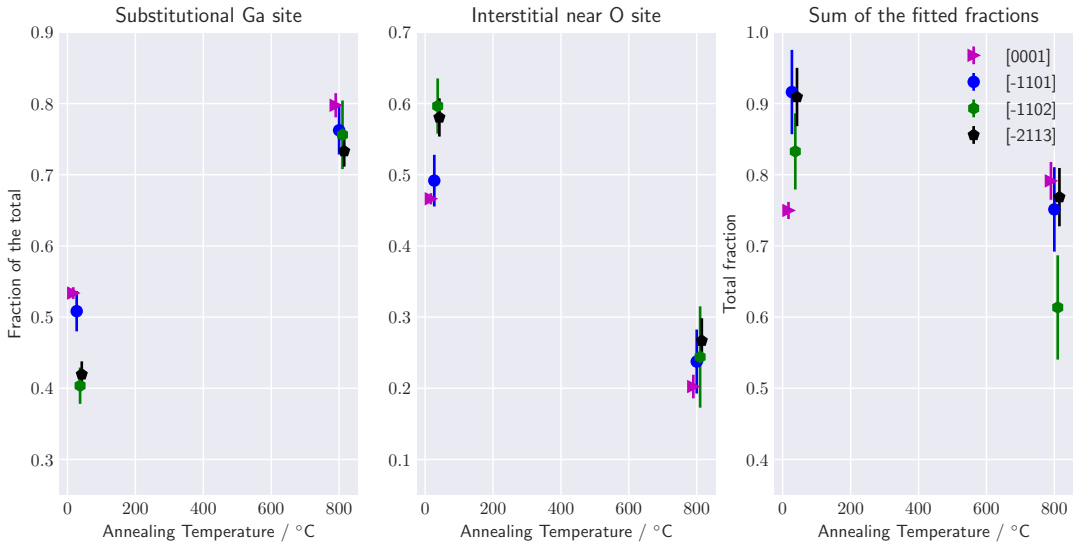

Figure 5.12: Site occupancy dependence with the annealing temperature as described from the analysis of the pad measured data. For the two occupancy plots on the left the fractions from the fit are scaled so that the sum of the two sites is 100 %. The third plot on the right shows the total fraction obtained by the fit followed by background correction.

Conclusions on ^{24}Na implanted in GaN

The measurement and analysis of an isotope that changes site with annealing brings a different kind of insight than the case of ^{43}K where the rms u_1 was in play. In the first case the importance lies in the changing yields and shape of the channeling axis and planes, in the latter the information is mostly concentrated to the shape of the axis channeling and the differences are more subtle, the smaller effect in the planes is very similar to a smoothing effect and so it is more affected by errors in the angular resolution. These two kinds of analysis are therefore complementary for testing the timepix detector.

The results from both detectors show very similar relative fractions but they also show significant contrast on the total fractions. In fact the pad measured fractions for the RT measurement were on average $\approx 16\,\%$ higher than the timepix's and for the 800 °C annealed measurement the fractions were on average $\approx 9\,\%$ higher. What this says is that in both cases the shape of the anisotropy was identified as respective to similar fraction but there seems to be a source of error in the background correction. While in the ^{43}K experiment the ratio between the fractions of both detectors was fairly constant it is hard to say if in this case there is another effect playing a role, such as for example diffusion changing the depth profile, an underestimation of the timepix gamma background (see table 5.1), or if it is a result of statistical fluctuations as the pad detector measurements have large error bars. Despite that having observed that the addition of timepix pixels into super-pixels, with the size of pad pixels, had the effect of diminishing the sum of the site fractions the causality of the effect remained unclear as a large portion

of the data was lost due to masked pixels affecting the super-pixels.

The analysis here presented has shown that in the as implanted state ^{24}Na occupies at 47 % the substitutional Ga substitutional site and at 53 % a near O interstitial site. After annealing at 800 °C for 10 min there is a clear shift from interstitial to substitutional sites, resulting in occupancy fractions of 76 % and 24 % for the same sites. Despite the interest in having a better understanding of the rms vibration for the probe atoms it was not possible to reach a conclusion on its value. Comparatively to the results here given, ref [81] presents an occupancy of 44 % and 56 % for the substitutional Ga and interstitial sites independently of the annealing temperature.

5.3 ^{27}Mg in p-type gallium nitride

Previous work by the EC-SLI collaboration has shown that radioactive ^{27}Mg probes implanted in p-type GaN occupy, in addition to substitutional Ga positions, also interstitial sites close to the HA position [43]. In the course of that work it became obvious that, besides the implantation temperature, also the accumulation of radiation damage or possibly even the fluence rate of implantation (i.e. the implantation current), may influence the Mg site distribution. Follow-up experiments, where implantations were performed at different temperatures and using different implantation currents, then also offered further possibilities of comparing the performance and analysis procedures of timepix and pad detectors.

For the timepix measurements implantations of ^{27}Mg ($t_{1/2} = 9.46$ min) in gallium nitride were performed with a 40 keV beam going through a 1 mm collimator, after which the channeling patterns were measured along the $[\bar{1}\,1\,0\,1]$ direction at 200 °C, 600 °C and 800 °C. Because of the short half life of ^{27}Mg the patterns are measured simultaneously with the isotope implantation at the given temperature, rather than after annealing as it is done with long lived isotopes. With the aim of testing the effects of the beam current, the sample was first implanted with a beam current of 0.2 pA, and later, after having measured at various implantation temperatures and waited for decay of the old ^{27}Mg activity, the procedure was repeated at a higher implantation current of 1.4 pA. Further details of the implantations can be consulted in table 5.1 for sample #475.

Note that in this case the timepix experiments were not performed on the same sample as the pad detector measurements, and also under somewhat different implantation conditions. This should be kept in mind when assessing differences in the results obtained with the two detectors.

The timepix patterns for this experiment were produced with the full detector matrix without summing adjacent pixels and the fit was done with the PyFDD software using the maximum likelihood optimization as the counts per pixel were too low for a chi-square fit. The sigma value for the Gaussian convolution was kept fixed at 0.050°.

As in the case of ^{24}Na described in section 5.2, the identification of the most probable interstitial

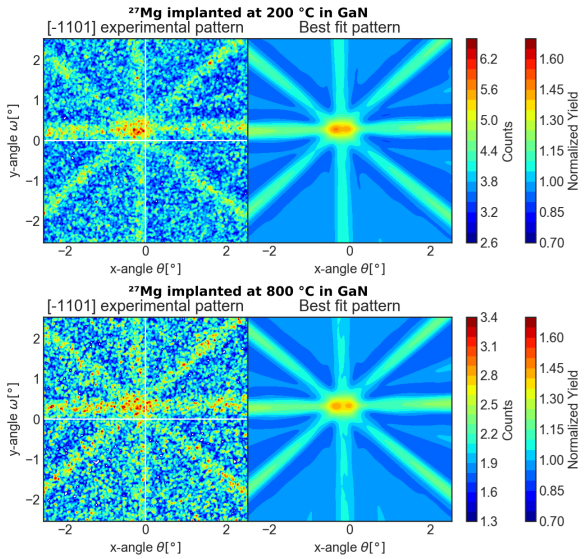

Figure 5.13: Emission channeling timepix measurement along the $[\bar{1}\,1\,0\,1]$ axis of ^{27}Mg implanted in GaN at 200 °C and 800 °C with the lower beam current of 0.2 pA. On the left is the measured pattern and on the right is the pattern, built from simulations, that best fits the data pattern. The normalized yield color scales have been calculated from the simulated yields of the fitted sites. The difference between the two measurements is hardly noticeable by eye, nonetheless the fit software reliably extracts the site fractions from the relative intensities of axial and planar effects caused by the specific superposition of substitutional and interstitial patterns.

site was achieved by a two site fit where the first site was kept fixed at the Ga substitutional and the second site was scanned parallel to the c-axis passing through the O interstitial site. In this process it was verified that the best site combination was a Ga substitutional plus an interstitial close to the HA site. The best fit pattern for the 200 °C and 800 °C measurements at low implantation current is shown in Fig. 5.13. The measurements at the lower beam current had 1 M, 1.3 M and 0.5 M counts for the patterns at 200 °C, 600 °C and 800 °C and the patterns measured with higher current had 1.1 M, 1.5 M and 1.5 M counts for the same temperatures.

Fig. 5.14 shows the identification of the most probable interstitial site with annealing temperature and implantation current. In this plot, each data point corresponds to the value of the cost function after a two site fit composed of the Ga substitutional site and the interstitial site that has a variable displacement from the O interstitial site. The reason why the depth of the minima varies considerably is due to the variation in the number of counts per pattern and because the interstitial fraction decreases with implantation temperature, therefore causing a lower impact on the cost function value.

The most probable sites for the low current implantations are found to be displaced from the O site by +0.162 Å, +0.373 Å and +0.373 Å at 200 °C, 600 °C and 800 °C respectively. With the high current implantation these displacements are +0.227 Å, +0.421 Å and +0.470 Å for the same temperatures. From these numbers it could seem like the interstitial sites for the higher current implantations have a larger displacement, but as the effect is small a direct correlation is not certain.

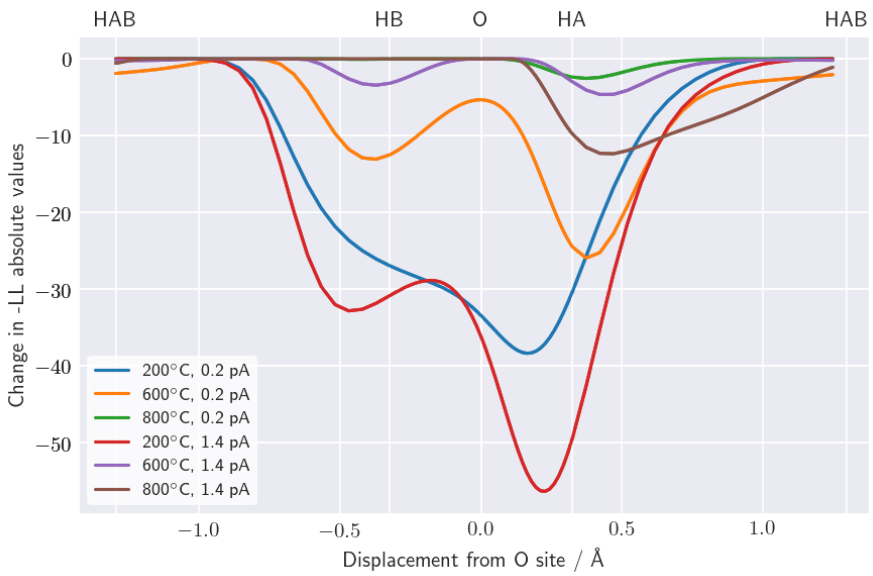

Figure 5.14: Identification of the most likely interstitial site of ^{27}Mg in p-type GaN measured with the timepix detector. The plot shows the change of the negative log likelihood (-LL) when in a two site fit the first site is kept fixed at the Ga substitutional and the second site has a variable interstitial position. The most likely interstitial site is found to be around the HA site.

Displacement coordinates are here given without statistical error bars as these are so small that not only they are hard to accurately determine but also have a questionable relevance when faced with systematic errors. If one would need to know the statistical errors in the site then it is necessary to look at the change in absolute values of the chi-square at the minima in Fig. 5.14. For a negative log likelihood plot, a one sigma error bar on the site displacement corresponds to the displacement that increases the negative log likelihood from its minimum by +1/2 (+1 for a chi-square plot). This error is so small that it is often below the displacement step in the simulations.

The temperature dependence of the fractions for the best fit sites is displayed in Fig. 5.15. It is shown that the relative substitutional fraction increases with the annealing temperature from around 76 % at 200 °C to 91 % at 800 °C and that there is a decrease in the interstitial fraction from 24 % to 9 % at the same temperatures. Although, for the two implantation currents the fractions at 27 °C and 800 °C are close, it seems that at 600 °C the ^{27}Mg transition from interstitial site to substitutional site is faster at the higher current implantation. Such a behaviour would be in line with the mechanism for the site change discussed in Ref. [43], which postulates that with rising implantation temperature interstitial Mg becomes mobile and combines with Ga vacancies created by the implantation. Since higher implantation currents also produce a larger number of vacancies, the site change would in this case be accelerated.

This isotope has also been measured with the pad detector in an earlier experiment. In this experiment ^{27}Mg was implanted with a beam collimated to 1 mm and with a current of 1.4 pA into GaN. In this pad experiment the angular resolution is actually better than in the timepix case as the distance to the

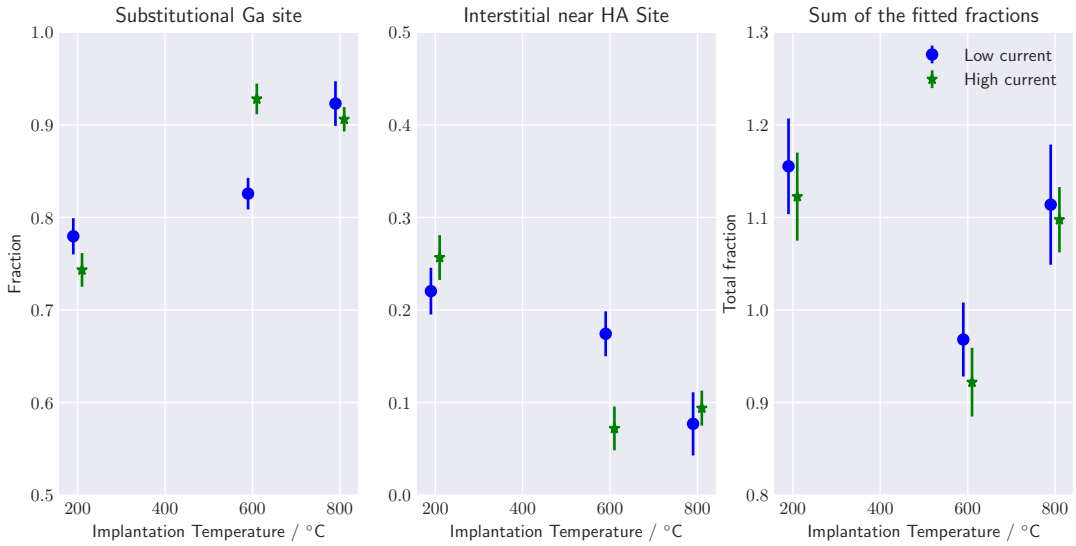

Figure 5.15: Site occupancy dependence with the implantation temperature for ^{27}Mg in GaN as described from the analysis of the timepix measured data. The fractions from the fit are scaled so that the sum of the two sites is 100 %. The two sites considered are the substitutional Ga and the best fit site between the interstitials O and HA at each temperature. At room temperature both sites are occupied, fractions of 74-78 % and 22-26 % were determined for the substitutional and interstitial sites, respectively. At 800 °C the interstitial site drops to 8-9 %, with 90-92 % of probes occupying the substitutional site.

sample was increased to 584 mm, in contrast the solid angle of the detector is reduced to about one fourth. The sample was implanted at 27 °C, 300 °C, 450 °C, 600 °C, 700 °C and 800 °C and simultaneously measured along the $[\bar{1}\,1\,0\,1]$ direction. At each respective temperature the obtained patterns had a total number of counts of 1.4 M, 1.4 M, 1.4 M, 1.6 M, 1.5 M and 0.9 M. Implantation details are further described in table 5.1.

The patterns were fit with two sites, one fixed at the Ga substitutional and an other varied from the O interstitial site parallel to the c-axis. The best fits of the patterns at 27 °C and 800 °C can be seen in Fig. 5.16. The identification of the most likely position of the interstitial site was performed by chi-square fitting, the results of which can be seen in Fig. 5.17 for each temperature up to 450 °C. Note that for implantation temperatures at 600 °C and above the interstitial fraction of ^{27}Mg was too small to perform a reliable identification of the position of the interstitial site. The chi-square fit gives the best results when the substitutional site is displaced from the O site by +0.37 Å, +0.42 Å and +0.47 Å for the temperatures of 27 °C, 300 °C and 450 °C respectively.

The site change of ^{27}Mg with increasing implantation temperature is shown in Fig. 5.18. In this plot the fractions for the most likely position of the interstitial site are used with exception of the data measured at 600 °C, 700 °C and 800 °C where the displacement of the interstitial site could not be identified and alternatively the results from fitting with the HA site are considered. The first two plots

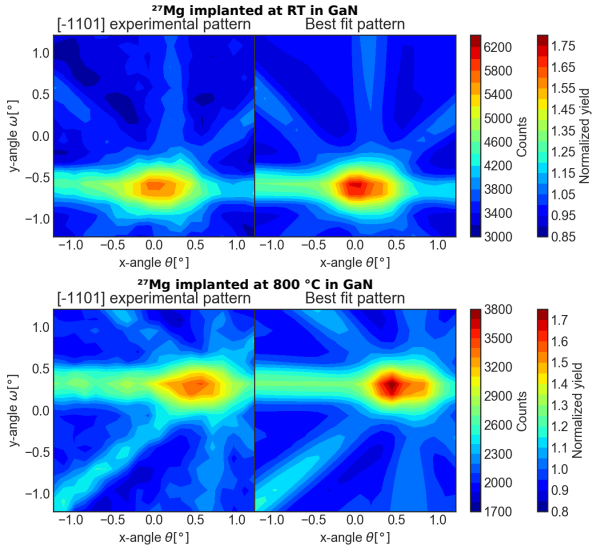

Figure 5.16: Emission channeling pad measurements of ^{27}Mg implanted in p-GaN along the $[\bar{1}\,1\,0\,1]$ axis at 27 °C and at 800 °C. For each pattern pair the left one is the measured pattern and on the right is the pattern, built from simulations that best fit the data pattern. The normalized yield color scales have been calculated from the simulated yields of the fitted sites. Here the site change is well visible on the 800 °C pattern as the channeling effect of the diagonal planes is more pronounced indicating a higher substitutional fraction.

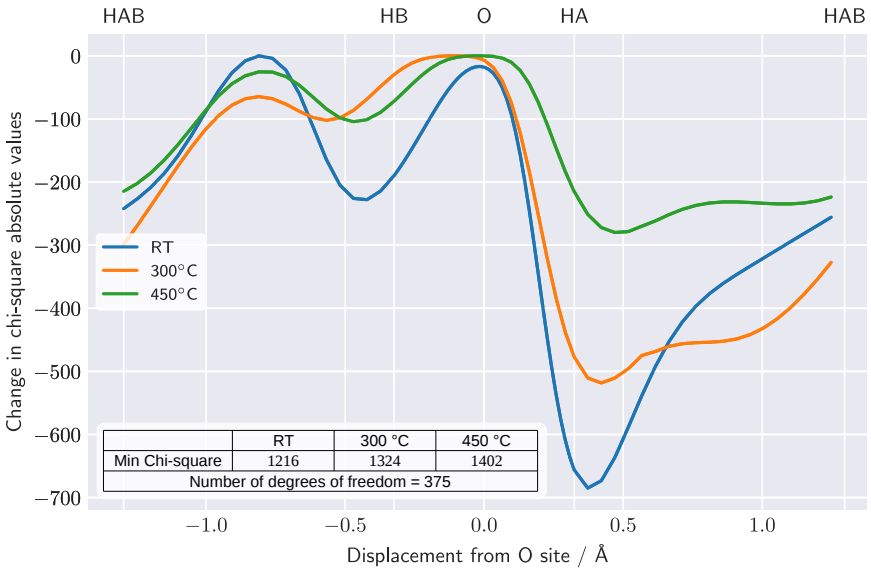

Figure 5.17: Identification of the most likely interstitial site of ^{27}Mg in p-type GaN measured with the pad detector. The plot shows the change of the chi-square when in a two site fit the first site is kept fixed at the Ga substitutional and the second site has a variable interstitial position. The most likely interstitial site is found to be around the HA site.

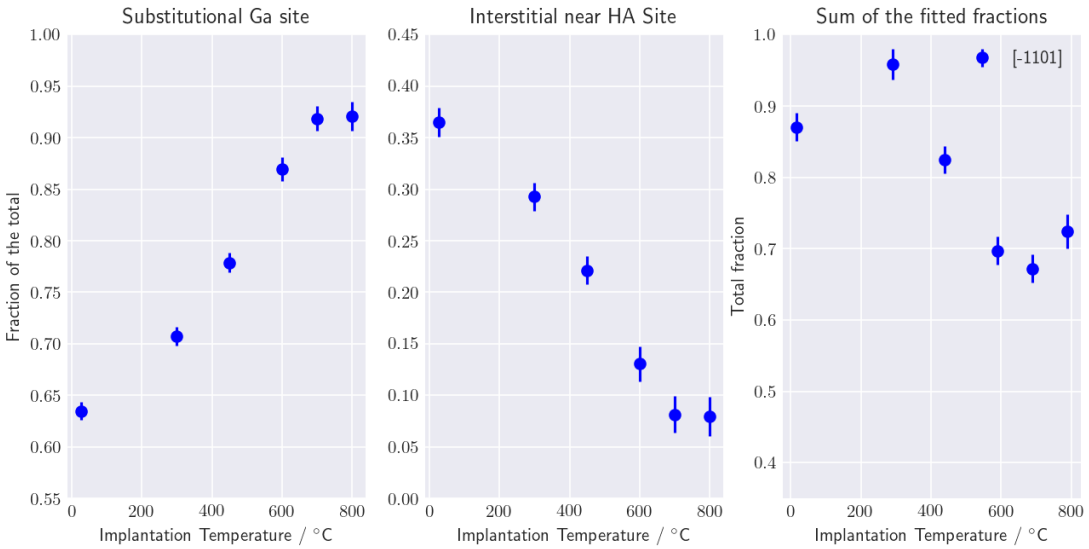

Figure 5.18: Site occupancy dependence with the implantation temperature as described from the analysis of the pad measured data. The fractions from the fit are scaled so that the sum of the two sites is 100 %. The sites considered are the Ga substitutional and the best fit site between the interstitials O and HA at temperatures under 500 °C, above which the HA site is used. At RT implantation both sites are occupied, in fact fractions of 63 % and 37 % are measured for the substitutional and interstitial sites respectively. At 800 °C the interstitial site drops to 8 %, with 92 % of isotopes occupying the substitutional site.

show the relative fractions from the Ga and near HA substitutional sites; there a clear tendency can be seen that the interstitial dopants gradually switch to the Ga substitutional site with the increase of the implantation temperature. On the third plot, showing the sum of the absolute fractions, an increase in the total fraction is seen after annealing at 300 °C which can be an effect of the restructuring of the implantation damage. At higher temperatures, it seems other effects exist as the total fraction decreases, a likely possibility is the diffusion of the implanted isotope to larger depth. This decrease at higher implantation temperatures, however, was not seen to the same extent in the timepix results.

Conclusions on ^{27}Mg implanted in GaN

This study of ^{27}Mg in p-type GaN was a demonstration of the use of timepix on an emission channeling experiment, where the lattice site fractions are tracked over a sequence of implantation temperatures. It is seen that the data taken with the timepix agree with what was obtained from previous measurements done with the pad detector.

The analysis showed clear changes in the lattice sites of implanted ^{27}Mg, revealing a systematic behaviour as a function of implantation temperature when relative fractions on substitutional and interstitial sites were plotted.

In contrast, as in the case of the ^{24}Na experiment, absolute, background-corrected site fractions showed a greater variety, which is visible from the fact that the sum fractions displayed in Figs. 5.9, 5.12, 5.15, 5.18 are not constant. The reasons for this are not fully understood, but factors that could explain such a behaviour are changes in the depth profile of the implanted isotope (likely for the annealed ^{24}Na sample), and a variation in the contribution of background to the measured patterns. The latter is more likely to occur during on-line experiments, as in the case of ^{27}Mg, where measurement conditions are subject to change. For instance, changes in the collimation and direction of the incoming ^{27}Mg beam may cause a variation in the gamma background of the measurements, since typically only around 30-50 % of ^{27}Mg is implanted into the sample, while the rest is left on the 1 mm collimator. While electrons emitted from ^{27}Mg on the collimator cannot reach the detector, gamma particles can. The overall contribution of gamma particles to the detector count-rate is usually not too high for ^{27}Mg (typically 10 %) but it may reach 30 % for badly collimated beams. Similarly, a different response to low energy gamma particles and related errors in the background correction are considered the most likely cause of the discrepancy in the sum fractions determined from timepix compared to pad detector measurements.

The measurements have shown that ^{27}Mg impurities are divided into two sites, the Ga substitutional and the interstitial close to the HA site. The timepix measurements describe that at 200 °C 76 % of the isotopes occupy the substitutional site, at 800 °C the occupancy increases to 91 %. Similarly, with the pad detector the substitutional fraction obtained was of 63 % at 27 °C which went up to 92 % at 800 °C. As with the ^{24}Na experiment the relative fractions agree very well in both experiments.

5.4 Detector usage and analysis insights

This section is about using the data acquired during the experiments to give further insights on the data acquisition and analysis. The practical exercise of trying to reproduce the same results with two measurement systems has proven to be a good way to push for the better understanding and improvement of the experimental method. Differences had to be explained and minimized as much as possible. Among the physical properties that proved to be the hardest to match between the detectors have been the absolute and random fractions of the implanted isotope. Two factors that could play a role in this effect are here analysed, the background correction and the pixel size.

Table 5.1 compiles the experimental conditions of the experiments here described and respective background correction values. Analysing these values in a systematic way could hint for clues on the total fraction discrepancy. The beta correction factors are calculated from GEANT4 simulations for the given isotope and implantation depth profile. Contrary to expectations, the simulations show that the beta energy spectrum has a reduced effect on the correction factor. Additionally, as the geometries of the setup for the two detectors are almost the same, when at 315 mm distance, the correction factors

Host crystal	Isotope	Sample #	Imp. energy	Imp. angle	Imp. current	
GaN	^{43}K	472	40 keV	17	9 pA	...
GaN	^{43}K	330	50 keV	17	–	...
GaN	^{24}Na	472	40 keV	17	7 pA	...
GaN p-type – pad	^{27}Mg	476	30 keV	17	–	...
GaN p-type – tpx	^{27}Mg	475	50 keV	17	0.2 pA & 1.4 pA	...

	Collimator	Total imp. fluence	Distance	Imp. range	Imp. straggling	
...	1 mm	$\approx 4 \times 10^{13}$ atoms/cm^2	32 cm	238 Å	116 Å	...
...	0.4 mm	$\approx 7 \times 10^{13}$ atoms/cm^2	32 cm	291 Å	140 Å	...
...	1 mm	$\approx 3 \times 10^{13}$ atoms/cm^2	32 cm	419 Å	208 Å	...
...	1 mm	$\approx 2 \times 10^{13}$ atoms/cm^2	60 cm	299 Å	155 Å	...
...	1 mm	$\approx 7 \times 10^{11}$ atoms/cm^2	32 cm	500 Å	249 Å	...

	β corr. pad	β corr. tpx	γ corr. pad	γ corr. tpx
...	1.74	1.74	1.12	1.07
...	–	1.74	–	–
...	1.74	1.74	1.13	1.07
...	1.63	–	1.076	–
...	–	1.75	–	1.075

Table 5.1: Table summarizing the experimental conditions and background corrections. The beta background corrections are calculated by means of GEANT4 simulations, for the set of experimental conditions here described these show little variation with emission energies or implantation depth. The gamma background also has only small variations between experiments but shows consistently larger values for the pad detector.

are essentially equal. Similarly, it seems that the isotope does not have a large effect on the gamma background correction, although there is a noticeable increase from the timepix to the pad detector due to the increased detector volume and possibly due to imperfections in the measurement of the gamma background.

It was questioned if the lower resolution caused by the large pixel size of the pad detector could be another effect altering the total fraction obtained by the fit. To test the effect of the pixel size, timepix pixels were added together in square bins with incrementing size to emulate the effect that large pixels have on the fit results, the outcome of which is shown in Fig. 5.19.

In order to produce this analysis in the most unbiased way some measures were taken. Simultaneously to the increase of the bin size, the sub-pixel mesh that is used to average the simulation over the bin area, was also increased. This ensured that a similar sampling rate of the simulation was maintained during this analysis. Additionally, the summing of pixels was done in a way that keeps the central cross between detector chips masked and as small as possible. However, an increase of the area of central masked pixels could not be avoided as it followed the increasing bin size. Furthermore, large bins that

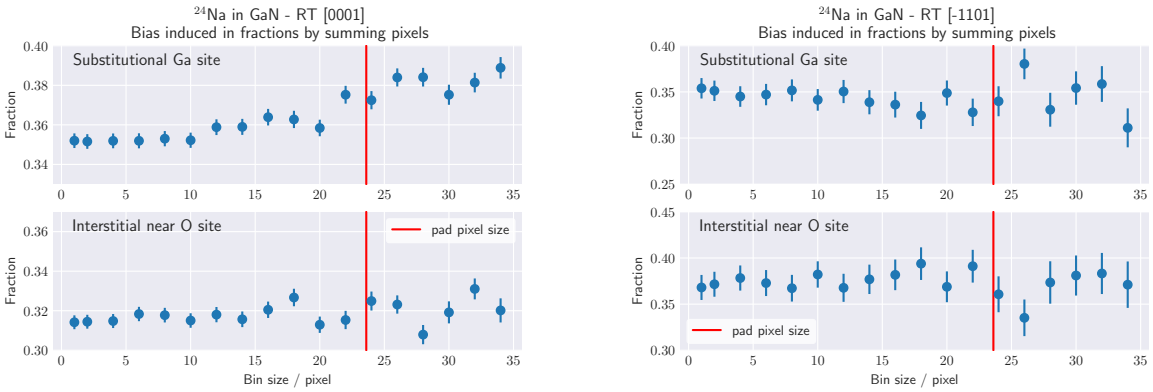

Figure 5.19: Effect of the bin size on fractions. These two figures show the effect of increasing the bin size with the sum of adjacent pixels on fractions. Figure a) shows the change in fraction obtained from a $[0\,0\,0\,1]$ pattern, which is expected to be more sensitive to the angular resolution, and figure b) show the fractions obtained from a $[\bar{1}\,1\,0\,1]$ pattern. The bias caused by the increase in pixel size is very small below a bin size of 10 and amounts to at max 3% at the pad pixel size level. Only the substitutional Ga $[0\,0\,0\,1]$ axis shows a clear tendency of an increase in the obtained fraction. The bin size is here represented by its side length, so that a bin size of 5 has 5 $\times$ 5 pixels.

include one or more masked pixels are also masked. These factors cause that the underlying dataset for each bin size test is not completely constant, which adds some degree of variability to the results.

The summing of pixels into large bins causes a loss of information similar to what is lost with a decrease of angular resolution. An immediate effect of this reduction in information is the increase of the error bars. Another effect that contributes to the increase of the error bars seen in Fig. 5.19, is the increase in the masked area and consequent reduction in the number of counts. More importantly, fluctuations in the fraction of $\approx 3\%$ can be seen once the bin size has reached the level of the pad detector pixel size. Two effects could be acting here: Firstly, because the data included in the fit pattern is not always the same, as the mask varies with the size of the bin mesh, some fluctuation is due to occur. Secondly, if a better fit of the data can be achieved when the data is packed into a lower resolution pattern with large bins, then it is possible that this would induce a higher channeling fraction. The latter could explain the gradual increase in the substitutional Ga fraction for the $[0\,0\,0\,1]$ axis.

Another interesting and practical aspect of summing bins is the speed-up of the analysis. Fig. 5.20 shows the effect of increasing the bin size on the analysis time. This is important as in a first approach it can be beneficial to sacrifice some angular resolution for a faster analysis. As the plot in the figure shows, the reduction in fit time only happens up to a bin size of 4 $\times$ 4 pixels, this is mostly due to the fact that above this value more sub-pixels are necessary.

Besides reducing the amount of information available in the pattern, large pixels can cause aliasing artefacts. Aliasing effects occur when the size of pixels is larger than the features of the channeling effect. When aliasing occurs, small shifts in the pattern can cause apparent significant changes in the

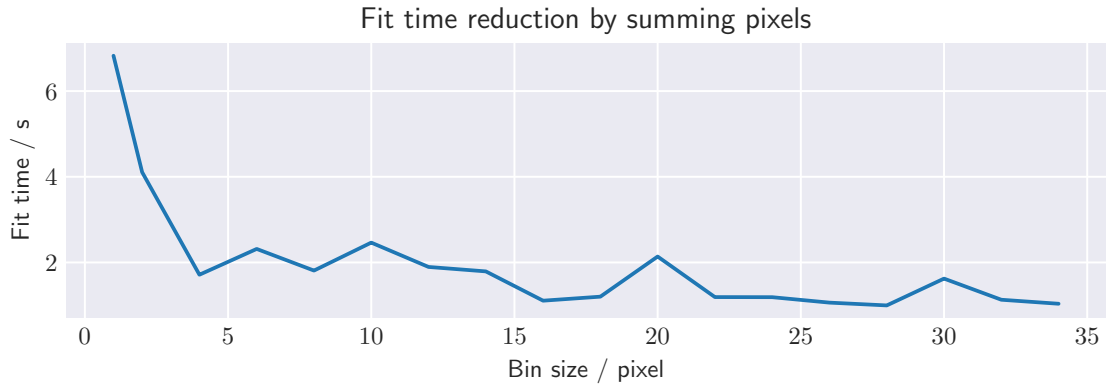

Figure 5.20: Fit time of a timepix channeling pattern versus the bin size. For this fit a timepix-quad experimental channeling pattern of ^{24}Na in GaN is fit with its two best fit sites. The plot shows that the fit time stabilizes around 4×4 pixels summed, this is in part because the pixel reduction needs to be compensated by a finer sub-pixel mesh. Note that the absolute fit time presented here is not to be seen as a benchmark as it may vary between experiments. The bin size is here represented by its side length, so that a bin size of 5 has 5×5 pixels.

observed pattern. Fig. 5.21 exemplifies the effects of aliasing with a one dimensional Gaussian that is sampled and represented by a bar plot; as the Gaussian shifts the bar plot changes significantly even though the Gaussian does not. The same principle is then applied to a simulated channeling pattern to demonstrate the effect on axial channeling, even though the same channeling conditions produce the two patterns these look significantly different. The last figure shows how, during the fit, PyFDD succeeds in recreating the aliasing effects in the pattern's diagonal planes channeling, hence mitigating the effect.

On the whole, it can be said that using bins with only one pixel takes a lot of time to fit but conserves information. Also, using bins with many summed pixels can cause some degree of bias in the fractions due to the loss of information and requires care in avoiding aliasing effects.

In the special case of chi-square fits, as explained in section 2.4.2, bias can occur if the number of counts per bin is low. In order to visualize this effect, Fig. 5.22 analyses the effect of the number of counts per pixel in the resulting fit fractions. This information is useful for the experimentalist to make the best choice in how many pixels to add in each bin so that bias is reduced to an acceptable level. The plot was done by taking experimental patterns from the ^{24}Na in GaN experiment with good statistics and recreating them with the intended number of counts by means of the Monte Carlo (MC) technique. Patterns generated in this way cause an inherent random fluctuation in the obtained fractions that is represented by the error bars. What can be seen from this analysis is that for the chi-square the initial variation is much larger than the error bars due to the fit method bias. This bias gets then reduced to roughly 1% when reaching 20 counts per pixel.

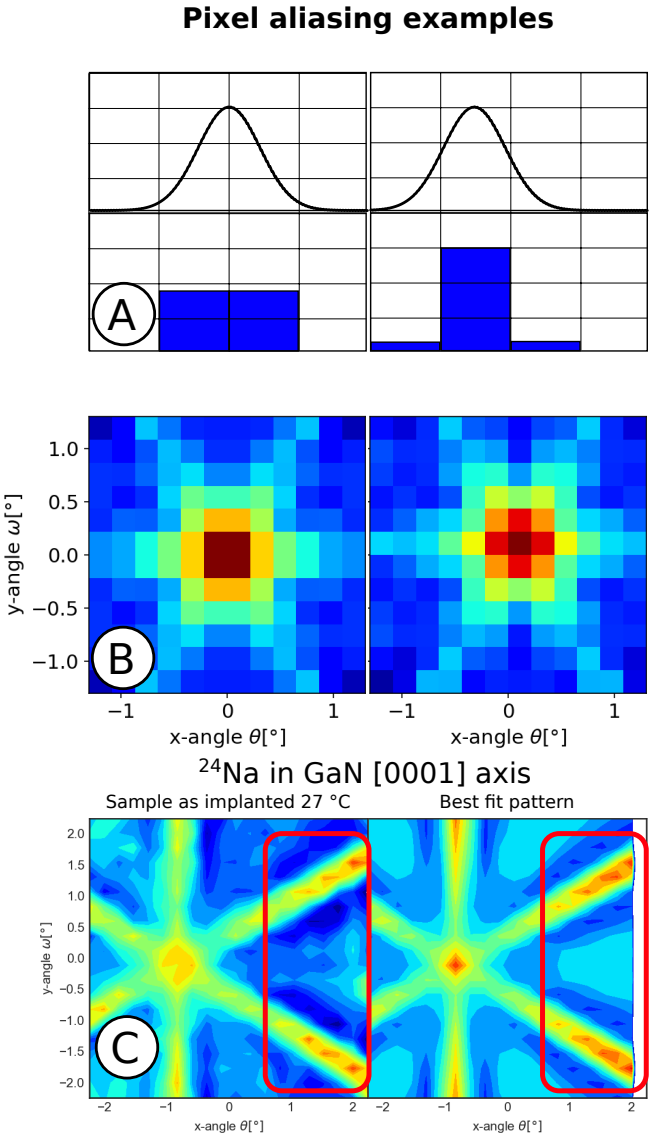

Figure 5.21: Examples of pixel aliasing. Firstly, the A part shows how the same Gaussian can be sampled completely differently by the bottom bar plot because of a small shift. The B part illustrates the same effect using a simulated emission pattern which is sampled with two slightly different orientations by bins the size of the pad detector pixels. As one pattern is shifted by half a pixel compared to the other the two patterns seem quite different despite having been built from the same simulated conditions. The bottom C part shows an experimental pattern and its corresponding best fit. In the highlighted planar channeling it can be seen that due to aliasing effects the plane shows an oscillating feature that is not a real channeling effect, it also shows that the PyFDD software accurately reconstructs the effect.

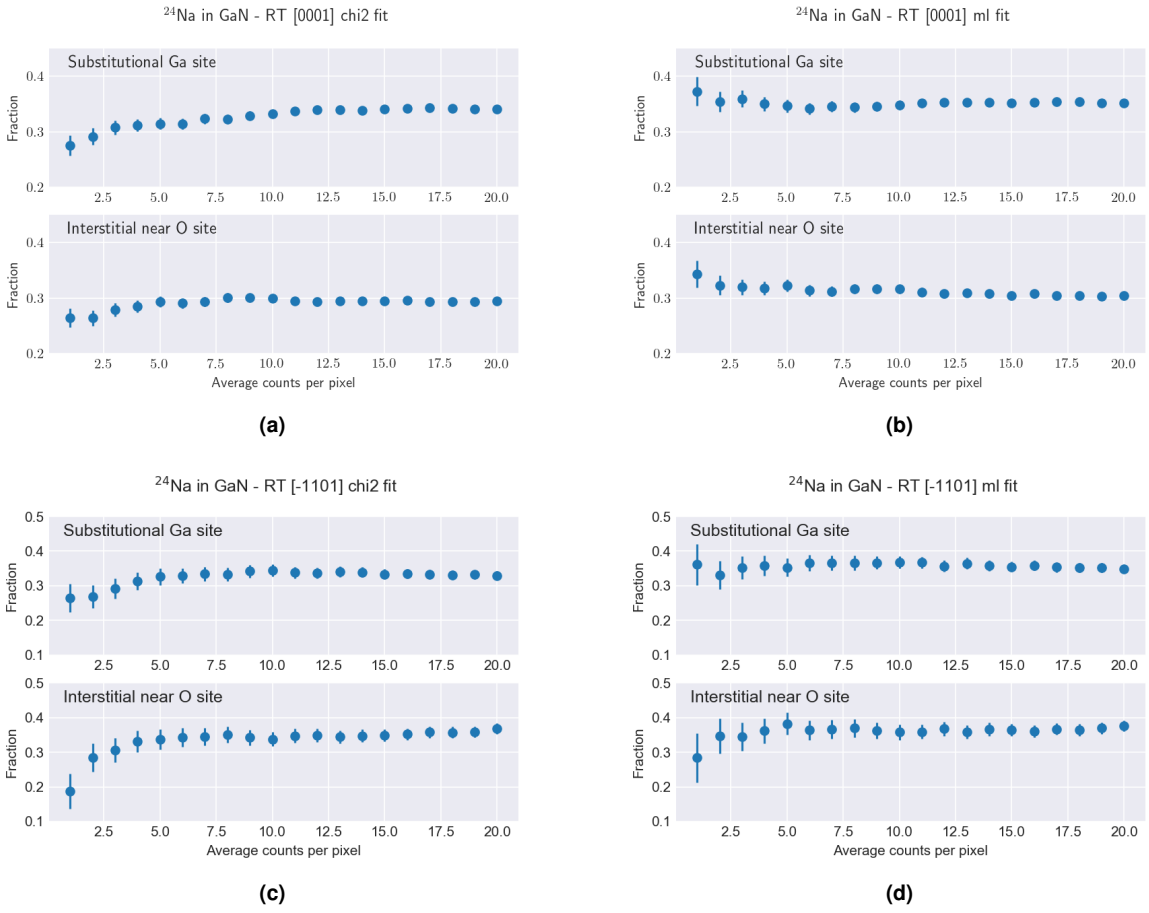

Figure 5.22: Bias in chi-square fits due to low pixel counts. Panels (a) and (c) are fitted fractions resulting from the chi-square approach, in comparison to the maximum likelihood technique [panels (b) and (d)], illustrating the convergence of results with the increase in the number of counts per pixel. For a low number of counts the variation in the maximum likelihood plots is due to the random fluctuations and is of the order of magnitude of the error bars, on the contrary, the chi-square plots show a bias that is much larger than the error bars. With increasing number of counts per pixel the chi-square bias gets reduced down to $\approx 1\%$ at 20 counts per pixel. The fit patterns were produced by Monte Carlo generation using the shape of real experimental patterns taken with the timepix-quad as the PDF.

6

Conclusions

In this thesis the application of a timepix-quad detector was investigated for lattice site location experiments with electron Emission Channeling (EC). The need for finding a replacement for the old pad detectors and the perspective of gaining useful additional channeling information from the high position resolution of this new detector, provided the motivation for this study. Subsequently, the focus of this work was directed to the experimental technique state of the art and to the careful evaluation of, how improvements in detector technology can contribute to the evolution and performance of the EC technique.

This work started with the installation of the timepix-quad detector and adjacent computing systems for data treatment. The detector technology is now at a stage where plug and play solutions offer a stable working system for the detector and readout software. This greatly simplified the installation process as the detector could start operating simply by being connected to a power source and to a computer by USB-3. What was still required to do in terms of the installation was to mount the detector inside a custom-built vacuum chamber and connect it to the readout hardware, located outside the chamber, by means of a custom-made vacuum feed-through.

This installation required small re-adjustments of the detector from time to time, however, it proved

to be acceptably stable to be used in EC over the four years it was operated, with the detector being used around 8 weeks a year, mainly during beam times with short lived isotopes. Over time, some deterioration of the timepix-quad detector was noticeable with the increase of the number of noisy pixels. This could be partially mitigated with a reduction of the bias, an increase of the detector value for the IKrum setting allowing for a higher leakage current and also, with updates to the pixel rejection mask. The detector was tested and able to run continuous 3-days non-stop acquisitions.

Even though the timepix detector is an energy sensitive detector, it was mainly used in counting mode. The energy calibration of the timepix requires an irradiation of the detector with a high flux source of x-rays of different energies. Since this is a complicated process that requires access to an x-ray machine and the process has to be repeated every time the detector configurations are changed, this detector feature was not used.

The operation characteristics of the timepix-quad detector and of the older pad detector were compared. Firstly, while both have a similar surface area ($\approx 28 \times 28\,\mathrm{cm}^2$) the setup that uses timepix has a slightly better overall angular resolution as a result from the much smaller pixel size but unchanged beam spot size on sample. Secondly, in operating conditions that avoid detector readout saturation and pileup, both detectors can achieve similar count-rates (3500 counts / s for the pad and 4000 counts / s for the timepix). Higher count-rates are possible with the pad but this would imply higher dead-time, similarly, a higher count-rate is possible with the timepix but this would mean having more events per frame and therefore more pileup. However, as the timepix operates with a frame based readout it has a significant dead time of 48 % when using frames of 0.1 s and therefore for the same sample activity an online measurement would take twice as long as with the old pad detector.

While the detector hardware and control software are readily available from the manufacturer the data treatment software for event clustering and building of histograms is still under development and it is continuously being adapted to the changes in readout values and increased data volumes that arrive as new detector chips are being developed. Therefore, appropriate software is generally developed in-house, like it was done for this thesis, and shared between the collaboration research teams. Adjacent to the detector control computer another one was set up only dedicated to data treatment and analysis. There, the data treatment for clustering pixel triggers and building channeling patterns was set up with an adapted version of the MAFalda framework code [68].

The MAFalda framework code allowed to implement an on-line analysis of the incoming flux of data. However, as it was not initially implemented for fast treatment of ongoing experiments, the data treatment time is longer than desirable, even after custom changes were introduced such as saving the current state of the treatment during online measurements. In fact, depending on how much data has been acquired since the previous analysis this process could take just a couple of minutes, or it could take over 1 h in the case of an overnight measurement. For this reason, I advise that for the purpose of

clustering hit pixels other solutions should be investigated, some of which are mentioned in section 2.3. As it stands, the readout system for the pad detector provides the visualization of an ongoing measurement significantly faster than what is achieved with the timepix detector.

Emission channeling patterns acquired with the timepix-quad detector required some changes of the analysis process. This led to the development of a new software, PyFDD, aimed at the analysis of channeling data taken with high density pixel detectors. The first changes of all were made in the pattern treatment process and accounted for methods of masking pixels, visualization and corrections to the pixel mesh, particularly at the timepix chip edges. The most relevant change was the implementation of the fit by maximum likelihood (in addition to the chi-square fit) in order to adapt the statistical methods and reduce bias in the analysis of data from detectors with small pixels, such as the timepix, which often have a low number of counts per pixel. The impact of this fit method was made clear by a comparative test where it was shown that the maximum likelihood fit method significantly reduces the bias in comparison to the chi-square method when the number of counts per pixel is lower than 20. Above this limit both methods provide similar results, however the chi-square has the advantage of being able to provide a value for the quality of fit.

The evaluation of the benefits gained from the increased angular resolution when comparing the pad and timepix detectors was performed using the results' uncertainty of the experimental measurements as an indicative value for change in quality. For this reason special care was put during the development of PyFDD on the correct calculation of statistical error bars. In fact, all the improvements implemented in the statistical methods were aimed at reducing bias in the analysis and evaluating the improvements in the results due to the changes in the detection system. Despite the focus of this work on the setup angular resolution, the use of the size of the error bars as an indicator of quality is just as appropriate to study the potential impact on the quality of the results from future changes that might be added in the measurement or simulation process. Furthermore, the chi-square, as is given by PyFDD, can be used to calculate the quality of fit as a p-value (see section 2.4.2) which can also be used as a valuable indicator of improvement, however, in order for this value to give useful information a better agreement between the model and experimental patterns is needed.

One of the objectives of the thesis was to test the timepix detector setup in a well studied material for which GaN was chosen. Lattice location studies were then made for implantations of ^{43}K ($t_{1/2} = 22.3\,\mathrm{h}$), ^{24}Na ($t_{1/2} = 15\,\mathrm{h}$) and ^{27}Mg ($t_{1/2} = 9.46\,\mathrm{min}$), all of which were analysed using the PyFDD software.

For potassium, it was found that this element occupies a Ga substitutional site which is stable up to 800 °C annealing. However, the probe atoms seem to occupy a distribution of sites near the Ga substitutional site that can be reproduced by assuming a higher root mean square (rms) displacement amplitude u_1. This study highlighted the need to accurately define the angular resolution while fitting due to the fact that it correlates with the u_1 value. For this reason the PyFDD feature, which allows to

set the angular resolution value at fit time, instead of doing previous simulations for a range of different angular resolution values, proved useful.

In the sodium study it was found that in the Room Temperature (RT) as implanted state this probe element occupies at 47 % the Ga substitutional site and at 53 % a near O interstitial site. The occupancy fractions change to 76 % substitutional and 24 % interstitial upon annealing at 800 °C. Comparing the data measured for the same experimental situation with both detectors, it was found that while the relative fractions were very similar between the detectors the total fractions had some differences. It is believed that this effect is mostly due to differences in the gamma background measurements and respective corrections.

At last, the measurement of magnesium in GaN has shown that it occupies a mixture of Ga substitutional and the HA interstitial sites with respective fractions at RT implantation of 76 % and 24 % for the timepix detector and for the pad 63 % and 37 %. After annealing at 800 °C the fractions for the same sites changed to 91 % and 9 % for the timepix detector and for the pad 92 % and 2 %. Note that in this case the measurements of the two detectors were not from the same sample, explaining some of the variation in the results. Nonetheless, in these experiments it became increasingly clear that measuring the total fraction of occupied sites is a complex challenge involving background measurements and simulations, as well as, dispersion of probes during annealing.

The beta and gamma background has also been a major topic of interest in this thesis. In a first approach the GEANT4 simulation software for beta background simulation was adapted to the conditions of the timepix detector and to a newer version of GEANT4 and root. From there the study continued to evaluate the impact that the background has on the lattice site location measurements. From the simulations of beta particles it was seen that the particle fluence of scattered betas is uniform over the detector area and that for the beta energies of the isotopes used in this thesis there is no difference in the beta background correction factors. On the contrary, for the gamma background it was seen that the fluence is not uniform over the detector and, consequently, it has an effect on the resulting fractions. Furthermore, there are strong indications that the measurement of the gamma background is underestimated for the lower gamma energies, this is particularly evident for the timepix detector.

In a more general perspective, with this thesis it was shown that changing from a pad detector with 1.3 mm pixels to a highly pixelated timepix-quad Position Sensitive Detector (PSD) will not significantly improve the quality of the lattice location results for most experiments. Nonetheless, the thesis particularly highlights that there are still significant differences between the simulation (fit model) and the acquired data which reveals that there is room for improvements which do not depend on changes to the channeling measurement system but instead require better understanding and more complex modelling of the data acquired. Furthermore, this thesis provides the statistical tools necessary to evaluate the impact of future model improvements.

From this point forward it is interesting to look at the vast future possibilities for improvements in data modelling and discuss which paths could be privileged to follow, as it is still unclear which specific points will lead to a better model. Something to consider is that most likely each of these future options will increase the number of parameters in the analysis causing some additional complexity in the fitting and interpretation of the results. However, some of these extra parameters can have additional scientific interest for the understanding of the measured sample and have the potential to offer more physics knowledge than just an enhanced accuracy. A first step in this direction would be to include a measurement of the gamma background in the fit model so as to correct for its anisotropy. In this case the probability density function (p.d.f.) of the fit would be defined as

$$p.d.f. = F_{\gamma}^{-1} P_{channeling} + (1 - F_{\gamma}^{-1}) P_{\gamma\, background}\,, \tag{6.0.1}$$

where $P_{channeling}$ would be the p.d.f. of the channeling pattern, $P_{\gamma\, background}$ would be a p.d.f. built from a measurement of the gamma background and F_{γ} is the gamma background correction factor. Another option would be to tune parameters in the emission channeling simulation steps that happen after the many-beam calculations and therefore do not require a re-run of the most computationally intensive part. One example of this is the depth profile of the implanted probe elements that is known that it can vary during annealing. Consequently, the current method of using a unique depth profile defined by the implantation conditions and detector position in relation to the sample, for all annealing steps might lead to biased fit results. However, as other methods exist that are more sensitive to depth profiles, like ion beam channeling, it may be argued that the gains to such an improvement approach are limited. A much more ambitious research option, yet much more complex, is to make comparative testing of other existing many-beam software (such as the MSOFT discussed in section 2.2) in the search for better model simulations. A major switch in simulation software such as this would require a lot of work, however it could also benefit from a lot of the tools existing in these softwares that help simulate new and more complex structures, possibly also faster.

As an outcome from this thesis, there are also some ideas that are advised against being included in near future plans. One, is the idea to enhance the technique by improving the angular resolution through a reduction in the implantation beam spot, extremely difficult to do from beam focusing vs transmission conditions, and also potentially increasing too much the ion density concentration and consequent implantation damage. As a matter of fact, it was clearly shown that the benefits of timepix detector come from the practical aspects of its use, related to the active development and modern solutions it provides, but not from the increased pixel density. Another, is the improvement of the modelling of the particle detection system by accounting for a non-isotropic angular resolution caused by non-circular ($\approx$1 mm diameter) beam spots, the reason being that the value for the resolution can be easily updated to its two

dimensional (2D) average and that the stretching artefacts caused by such beam spots is small when compared to other factors. The last idea which is not advised to be followed, is the simultaneous fit of several axes, at least until the magnitude of the systematic errors becomes smaller than its statistical error counterpart.

At last, it is clear that the future of the detectors for emission channeling holds a place for the timepix detectors. At the time of writing this thesis the next generation of detector chips, the timepix-4 are being tested. These provide readout without dead time and astonishing count-rate speeds. These new detectors also provide new challenges and will require new software capable of fast clustering for showing the data pattern with little delay during online measurements. Nonetheless, they also show a bright future of fast and reliable lattice location of isotopes by emission channeling.

Bibliography

[1] H. Hofsäss and G. Lindner, "Emission channeling and blocking," *Physics Reports*, vol. 201, no. 3, pp. 121–183, Mar. 1991. [Online]. Available: https://doi.org/10.1016/0370-1573(91)90121-2

[2] H. Hofsäss, S. Winter, S. G. Jahn, U. Wahl, and E. Recknagel, "Emission channeling studies in semiconductors," *Nuclear Instruments and Methods in Physics Research Section B: Beam Interactions with Materials and Atoms*, vol. 63, no. 1, pp. 83–90, Jan. 1992. [Online]. Available: https://doi.org/10.1016/0168-583X(92)95174-P

[3] H. Hofsäss, U. Wahl, and S. G. Jahn, "Impurity lattice location and recovery of structural defects in semiconductors studied by emission channeling," *Hyperfine Interactions*, vol. 84, no. 1, pp. 27–41, Dec. 1994. [Online]. Available: https://doi.org/10.1007/BF02060641

[4] H. Hofsäss, "Emission channeling," *Hyperfine Interactions*, vol. 97, no. 1, pp. 247–283, Dec. 1996. [Online]. Available: https://doi.org/10.1007/BF02150180

[5] U. Wahl, "Emission channeling studies of Li in semiconductors," *Physics Reports*, vol. 280, no. 3, pp. 145–285, Feb. 1997. [Online]. Available: https://doi.org/10.1016/S0370-1573(96)00021-X

[6] U. Wahl, J. G. Correia, A. Costa, E. David-Bosne, L. M. C. Pereira, L. M. Amorim, V. Augustyns, K. Temst, A. Vantomme, M. R. da Silva, D. J. Silva, J. P. Araújo, P. Miranda, and K. Bharuth-Ram, "Emission Channeling with Short-Lived Isotopes (EC-SLI) at CERN's ISOLDE Facility," in *Exotic Nuclei*. WORLD SCIENTIFIC, Sep. 2014, pp. 563–573. [Online]. Available: https://doi.org/10.1142/9789814632041_0061

[7] D. S. Gemmell, "Channeling and related effects in the motion of charged particles through crystals," *Reviews of Modern Physics*, vol. 46, no. 1, pp. 129–227, Jan. 1974. [Online]. Available: https://doi.org/10.1103/RevModPhys.46.129

[8] Y. Wang and M. Nastasi, Eds., *Handbook of Modern Ion Beam Materials Analysis*, 2nd ed. Warrendale, PA: Materials Research Society, Mar. 2010.

[9] A. Vantomme, "50years of ion channeling in materials science," *Nuclear Instruments and Methods in Physics Research Section B: Beam Interactions with Materials and Atoms*, vol. 371, pp. 12–26, Mar. 2016. [Online]. Available: https://doi.org/10.1016/j.nimb.2015.11.035

[10] L. Pereira, A. Vantomme, and U. Wahl, "Characterizing defects with ion beam analysis and channeling techniques," *Characterisation and Control of Defects in Semiconductors*, pp. 501–561, Sep. 2019. [Online]. Available: https://doi.org/10.1049/PBCS045E_ch11

[11] E. Alves, U. Wahl, M. R. Correia, S. Pereira, B. De Vries, and A. Vantomme, "Annealing behavior and lattice site location of Er implanted InGaN," *Nuclear Instruments and Methods in Physics Research Section B: Beam Interactions with Materials and Atoms*, vol. 206, pp. 1042–1046, May 2003. [Online]. Available: https://doi.org/10.1016/S0168-583X(03)00930-3

[12] Q. F. Xiao, S. Hashimoto, W. M. Gibson, and S. J. Pearton, "Channeling lattice location of Se implanted into InP by RBS and PIXE," *Nuclear Instruments and Methods in Physics Research Section B: Beam Interactions with Materials and Atoms*, vol. 45, no. 1, pp. 464–466, Jan. 1990. [Online]. Available: https://doi.org/10.1016/0168-583X(90)90876-V

[13] L. Shao, Y. Q. Wang, M. Nastasi, and J. W. Mayer, "A technique to study the lattice location of light elements in silicon by channeling elastic recoil detection analysis," *Nuclear Instruments and Methods in Physics Research Section B: Beam Interactions with Materials and Atoms*, vol. 249, no. 1, pp. 230–233, Aug. 2006. [Online]. Available: https://doi.org/10.1016/j.nimb.2006.04.004

[14] M. Vairavel, B. Sundaravel, and B. Panigrahi, "Lattice location of O18 in ion implanted Fe crystals by Rutherford backscattering spectrometry, channeling and nuclear reaction analysis," *Nuclear Instruments and Methods in Physics Research Section B: Beam Interactions with Materials and Atoms*, vol. 383, pp. 47–51, Sep. 2016. [Online]. Available: https://doi.org/10.1016/j.nimb.2016.06.009

[15] J. Lindhard, "Motion of swift charged particles, as influenced by strings of atoms in crystals," *Physics Letters*, vol. 12, no. 2, pp. 126–128, Sep. 1964. [Online]. Available: https://doi.org/10.1016/0031-9163(64)91133-3

[16] J. Lindhard, "Influence of Crystal lattice on motion of energetic charged particles," *Kongel. Dan. Vidensk. Selsk., Mat.-Fys. Medd.*, vol. 34: No. 14, Jan. 1965. [Online]. Available: http://gymarkiv.sdu.dk/MFM/kdvs/mfm%2030-39/mfm-34-14.pdf

[17] A. P. Pogany and P. S. Turner, "Reciprocity in electron diffraction and microscopy," *Acta Crystallographica Section A: Crystal Physics, Diffraction, Theoretical and General Crystallography*, vol. 24, no. 1, pp. 103–109, Jan. 1968. [Online]. Available: https://doi.org/10.1107/S0567739468000136

[18] J. U. Andersen, S. K. Andersen, and W. M. Augustyniak, "Channeling of electrons and positrons," *K. Dan. Vidensk. Selsk., Mat.-Fys. Medd*, vol. 39, no. 10, pp. 1–58, 1977.

[19] J. U. Andersen, E. Bonderup, E. Lægsgaard, and A. H. Sørensen, "Incoherent Scattering of Electrons and Linewidth of Planar-Channeling Radiation," *Physica Scripta*, vol. 28, no. 3, pp. 308–330, Sep. 1983. [Online]. Available: https://doi.org/10.1088%2F0031-8949%2F28%2F3%2F008

[20] J. U. Andersen, E. Bonderup, and E. Laegsgaard, "Channeling Radiation — Quantum Theory," in *Coherent Radiation Sources*, ser. Topics in Current Physics, A. W. Sáenz and H. Überall, Eds. Berlin, Heidelberg: Springer, 1985, pp. 127–164. [Online]. Available: https://doi.org/10.1007/978-3-642-51185-1_6

[21] J. U. Andersen, "Channeling and Blocking of Energetic Particles in Crystals," in *Particle Penetration and Radiation Effects Volume 2: Penetration of Atomic and Molecular Ions*, ser. Springer Series in Solid-State Sciences, P. Sigmund, Ed. Cham: Springer International Publishing, 2014, pp. 549–588. [Online]. Available: https://doi.org/10.1007/978-3-319-05564-0_11

[22] R. Catherall, W. Andreazza, M. Breitenfeldt, A. Dorsival, G. J. Focker, T. P. Gharsa, G. T. J, J.-L. Grenard, F. Locci, P. Martins, S. Marzari, J. Schipper, A. Shornikov, and T. Stora, "The ISOLDE facility," *Journal of Physics G: Nuclear and Particle Physics*, vol. 44, no. 9, p. 094002, Aug. 2017. [Online]. Available: https://doi.org/10.1088%2F1361-6471%2Faa7eba

[23] U. Wahl, "Advances in electron emission channeling measurements in semiconductors," *Hyperfine Interactions*, vol. 129, no. 1-4, pp. 349–370, Dec. 2000. [Online]. Available: https://doi.org/10.1023/A:1012697429920

[24] P. Weilhammer, E. Nygård, W. Dulinski, A. Czermak, F. Djama, S. Gadomski, S. Roe, A. Rudge, F. Schopper, and J. Strobel, "Si pad detectors," *Nuclear Instruments and Methods in Physics*

Research Section A: Accelerators, Spectrometers, Detectors and Associated Equipment, vol. 383, no. 1, pp. 89–97, Dec. 1996. [Online]. Available: https://doi.org/10.1016/S0168-9002(96)00622-5

[25] U. Wahl, J. G. Correia, A. Czermak, S. G. Jahn, P. Jalocha, J. G. Marques, A. Rudge, F. Schopper, J. C. Soares, A. Vantomme, and P. Weilhammer, "Position-sensitive Si pad detectors for electron emission channeling experiments," *Nuclear Instruments and Methods in Physics Research Section A: Accelerators, Spectrometers, Detectors and Associated Equipment*, vol. 524, no. 1, pp. 245–256, May 2004. [Online]. Available: https://doi.org/10.1016/j.nima.2003.12.044

[26] M. Campbell, E. H. M. Heijne, G. Meddeler, E. Pernigotti, and W. Snoeys, "A readout chip for a 64x64 pixel matrix with 15-bit single photon counting," *IEEE Transactions on Nuclear Science*, vol. 45, no. 3, pp. 751–753, Jun. 1998. [Online]. Available: https://doi.org/10.1109/23.682629

[27] M. Campbell, "10 years of the Medipix2 Collaboration," *Nuclear Instruments and Methods in Physics Research Section A: Accelerators, Spectrometers, Detectors and Associated Equipment*, vol. 633, Supplement 1, no. 0, pp. S1–S10, May 2011. [Online]. Available: https://doi.org/10.1016/j.nima.2010.06.106

[28] R. Ballabriga, M. Campbell, and X. Llopart, "Asic developments for radiation imaging applications: The medipix and timepix family," *Nuclear Instruments and Methods in Physics Research Section A: Accelerators, Spectrometers, Detectors and Associated Equipment*, vol. 878, pp. 10–23, Jan. 2018. [Online]. Available: https://doi.org/10.1016/j.nima.2017.07.029

[29] X. Llopart and M. Campbell, "First test measurements of a 64k pixel readout chip working in single photon counting mode," *Nuclear Instruments and Methods in Physics Research Section A: Accelerators, Spectrometers, Detectors and Associated Equipment*, vol. 509, no. 1, pp. 157–163, Aug. 2003. [Online]. Available: https://doi.org/10.1016/S0168-9002(03)01565-1

[30] X. Llopart, R. Ballabriga, M. Campbell, L. Tlustos, and W. Wong, "Timepix, a 65k programmable pixel readout chip for arrival time, energy and/or photon counting measurements," *Nuclear Instruments and Methods in Physics Research Section A: Accelerators, Spectrometers, Detectors and Associated Equipment*, vol. 581, no. 1, pp. 485–494, Oct. 2007. [Online]. Available: https://doi.org/10.1016/j.nima.2007.08.079

[31] R. Ballabriga, M. Campbell, E. Heijne, X. Llopart, L. Tlustos, and W. Wong, "Medipix3: A 64k pixel detector readout chip working in single photon counting mode with improved spectrometric performance," *Nuclear Instruments and Methods in Physics Research Section A: Accelerators, Spectrometers, Detectors and Associated Equipment*, vol. 633, pp. S15–S18, May 2011. [Online]. Available: https://doi.org/10.1016/j.nima.2010.06.108

[32] T. Poikela, J. Plosila, T. Westerlund, M. Campbell, M. D. Gaspari, X. Llopart, V. Gromov, R. Kluit, M. v. Beuzekom, F Zappon, V. Zivkovic, C. Brezina, K. Desch, Y. Fu, and A. Kruth, "Timepix3: a 65K channel hybrid pixel readout chip with simultaneous ToA/ToT and sparse readout," *Journal of Instrumentation*, vol. 9, no. 05, p. C05013, 2014. [Online]. Available: https://doi.org/10.1088/1748-0221/9/05/C05013

[33] U. Wahl, A. Vantomme, J. De Wachter, R. Moons, G. Langouche, J. G. Marques, ISOLDE Collaboration, and J. G. Correia, "Direct Evidence for Tetrahedral Interstitial Er in Si," *Physical Review Letters*, vol. 79, no. 11, pp. 2069–2072, Sep. 1997. [Online]. Available: https://doi.org/10.1103/PhysRevLett.79.2069

[34] U. Wahl, A. Vantomme, G. Langouche, J. G. Correia, and ISOLDE Collaboration, "Lattice Location and Stability of Ion Implanted Cu in Si," *Physical Review Letters*, vol. 84, no. 7, pp. 1495–1498, Feb. 2000. [Online]. Available: https://doi.org/10.1103/PhysRevLett.84.1495

[35] U. Wahl, J. G. Correia, E. Rita, J. P. Araújo, J. C. Soares, and The ISOLDE Collaboration, "Lattice sites of implanted Fe in Si," *Physical Review B*, vol. 72, no. 1, p. 014115, Jul. 2005. [Online]. Available: https://doi.org/10.1103/PhysRevB.72.014115

[36] D. J. Silva, U. Wahl, J. G. Correia, and J. P. Araújo, "Influence of n+ and p+ doping on the lattice sites of implanted Fe in Si," *Journal of Applied Physics*, vol. 114, no. 10, p. 103503, Sep. 2013. [Online]. Available: https://doi.org/10.1063/1.4819210

[37] ISOLDE Collaboration, U. Wahl, E. Rita, J. G. Correia, A. C. Marques, E. Alves, and J. C. Soares, "Direct Evidence for As as a Zn-Site Impurity in ZnO," *Physical Review Letters*, vol. 95, no. 21, p. 215503, Nov. 2005. [Online]. Available: https://doi.org/10.1103/PhysRevLett.95.215503

[38] E. Rita, U. Wahl, J. G. Correia, E. Alves, and J. C. Soares, "Lattice location and thermal stability of implanted Fe in ZnO," *Applied Physics Letters*, vol. 85, no. 21, pp. 4899–4901, Nov. 2004. [Online]. Available: https://doi.org/10.1063/1.1825611

[39] L. M. C. Pereira, U. Wahl, J. G. Correia, L. M. Amorim, D. J. Silva, E. Bosne, S. Decoster, M. R. da Silva, K. Temst, and A. Vantomme, "Minority anion substitution by Ni in ZnO," *Applied Physics Letters*, vol. 103, no. 9, p. 091905, Aug. 2013. [Online]. Available: https://doi.org/10.1063/1.4820254

[40] S. Decoster, S. Cottenier, B. De Vries, H. Emmerich, U. Wahl, J. G. Correia, and A. Vantomme, "Transition Metal Impurities on the Bond-Centered Site in Germanium," *Physical Review Letters*, vol. 102, no. 6, p. 065502, Feb. 2009. [Online]. Available: https://doi.org/10.1103/PhysRevLett.102.065502

[41] S. Decoster, S. Cottenier, U. Wahl, J. G. Correia, L. M. C. Pereira, C. Lacasta, M. R. Da Silva, and A. Vantomme, "Diluted manganese on the bond-centered site in germanium," *Applied Physics Letters*, vol. 97, no. 15, p. 151914, Oct. 2010. [Online]. Available: https://doi.org/10.1063/1.3501123

[42] L. M. C. Pereira, U. Wahl, J. G. Correia, S. Decoster, L. M. Amorim, M. R. da Silva, J. P. Araújo, and A. Vantomme, "Evidence of N substitution by Mn in GaN," *Physical Review B*, vol. 86, no. 19, p. 195202, Nov. 2012. [Online]. Available: https://doi.org/10.1103/PhysRevB.86.195202

[43] U. Wahl, L. Amorim, V. Augustyns, A. Costa, E. David-Bosne, T. Lima, G. Lippertz, J. Correia, M. da Silva, M. Kappers, K. Temst, A. Vantomme, and L. Pereira, "Lattice Location of Mg in GaN: A Fresh Look at Doping Limitations," *Physical Review Letters*, vol. 118, no. 9, p. 095501, Mar. 2017. [Online]. Available: https://doi.org/10.1103/PhysRevLett.118.095501

[44] L. M. Pinto de Almeida Amorim, "Lattice site location of electrical dopant impurities in group-III nitrides," Ph.D. dissertation, Katholieke Universiteit Leuven, 2016. [Online]. Available: https://lirias.kuleuven.be/retrieve/424997

[45] E. David-Bosne, "Timepix and FitPix detection system for RBS/C materials analysis," Master's thesis, Universidade de Aveiro, 2013. [Online]. Available: https://ria.ua.pt/handle/10773/12087

[46] K. Johnston, J. Schell, J. G. Correia, M. Deicher, H. P. Gunnlaugsson, A. S. Fenta, E. David-Bosne, A. R. G. Costa, and D. C. Lupascu, "The solid state physics programme at ISOLDE: recent developments and perspectives," *Journal of Physics G: Nuclear and Particle Physics*, vol. 44, no. 10, p. 104001, 2017. [Online]. Available: https://doi.org/10.1088/1361-6471/aa81ac

[47] V. I. Mishin, V. N. Fedoseyev, H. J. Kluge, V. S. Letokhov, H. L. Ravn, F. Scheerer, Y. Shirakabe, S. Sundell, and O. Tengblad, "Chemically selective laser ion-source for the CERN-ISOLDE on-line mass separator facility," *Nuclear Instruments and Methods in Physics Research Section B: Beam Interactions with Materials and Atoms*, vol. 73, no. 4, pp. 550–560, Apr. 1993. [Online]. Available: https://doi.org/10.1016/0168-583X(93)95839-W

[48] V. Fedoseyev, G. Huber, U. Köster, J. Lettry, V. Mishin, H. Ravn, and V. Sebastian, "The ISOLDE laser ion source for exotic nuclei," *Hyperfine Interactions*, vol. 127, no. 1, pp. 409–416, Aug. 2000. [Online]. Available: https://doi.org/10.1023/A:1012609515865

[49] U. Köster, R. Catherall, V. Fedoseyev, S. Franchoo, U. Georg, M. Huyse, K. Kruglov, J. Lettry, V. Mishin, M. Oinonen, H. Ravn, M. Seliverstov, H. Simon, P. Van Duppen, J. Van Roosbroeck, and L. Weissman, "Isomer separation and measurement of nuclear moments with the ISOLDE RILIS," *Hyperfine Interactions*, vol. 127, no. 1, pp. 417–420, Aug. 2000. [Online]. Available: https://doi.org/10.1023/A:1012661532704

[50] V. N. Fedosseev, L. E. Berg, N. Lebas, O. J. Launila, M. Lindroos, R. Losito, B. A. Marsh, F. K. Österdahl, T. Pauchard, G. Tranströmer, and J. Vannesjö, "ISOLDE RILIS: New beams, new facilities," *Nuclear Instruments and Methods in Physics Research Section B: Beam Interactions with Materials and Atoms*, vol. 266, no. 19, pp. 4378–4382, Oct. 2008. [Online]. Available: https://doi.org/10.1016/j.nimb.2008.05.038

[51] J. F. Ziegler, M. D. Ziegler, and J. P. Biersack, "SRIM - The stopping and range of ions in matter (2010)," *Nuclear Instruments and Methods in Physics Research Section B: Beam Interactions with Materials and Atoms*, vol. 268, no. 11, pp. 1818–1823, Jun. 2010. [Online]. Available: https://doi.org/10.1016/j.nimb.2010.02.091

[52] P. H. Dederichs, *Dynamical diffraction theory*. Zentralbibliothek d. Kernforschungsanlage Jülich GmbH, 1971. [Online]. Available: http://juser.fz-juelich.de/record/136248/files/J%C2%A9%C6%A1l_0797_Dederichs.pdf

[53] A. Winkelmann, C. Trager-Cowan, F. Sweeney, A. P. Day, and P. Parbrook, "Many-beam dynamical simulation of electron backscatter diffraction patterns," *Ultramicroscopy*, vol. 107, no. 4, pp. 414–421, Apr. 2007. [Online]. Available: https://doi.org/10.1016/j.ultramic.2006.10.006

[54] A. Winkelmann, "Dynamical Simulation of Electron Backscatter Diffraction Patterns," in *Electron Backscatter Diffraction in Materials Science*, A. J. Schwartz, M. Kumar, B. L. Adams, and D. P. Field, Eds. Boston, MA: Springer US, 2009, pp. 21–33. [Online]. Available: https://doi.org/10.1007/978-0-387-88136-2_2

[55] A. Winkelmann, G. Nolze, M. Vos, F. Salvat-Pujol, and W. S. M. Werner, "Physics-based simulation models for EBSD: advances and challenges," *IOP Conference Series: Materials Science and Engineering*, vol. 109, p. 012018, Feb. 2016. [Online]. Available: https://doi.org/10.1088/1757-899X/109/1/012018

[56] S. Singh, F. Ram, and M. D. Graef, "EMsoft: open source software for electron diffraction/image simulations," *Microscopy and Microanalysis*, vol. 23, no. S1, pp. 212–213, Jul. 2017. [Online]. Available: https://doi.org/10.1017/S143192761700174X

[57] V. Kraus, M. Holik, J. Jakubek, M. Kroupa, P. Soukup, and Z. Vykydal, "FITPix — fast interface for Timepix pixel detectors," *Journal of Instrumentation*, vol. 6, no. 01, p. C01079, Jan. 2011. [Online]. Available: https://doi.org/10.1088/1748-0221/6/01/C01079

[58] J. Visser, M. v. Beuzekom, H. Boterenbrood, B. v. d. Heijden, J. I. Muñoz, S. Kulis, B. Munneke, and F. Schreuder, "SPIDR: a read-out system for Medipix3 & Timepix3," *Journal of Instrumentation*, vol. 10, no. 12, pp. C12 028–C12 028, Dec. 2015. [Online]. Available: https://doi.org/10.1088%2F1748-0221%2F10%2F12%2Fc12028

[59] B. v. d. Heijden, J. Visser, M. v. Beuzekom, H. Boterenbrood, S. Kulis, B. Munneke, and F. Schreuder, "SPIDR, a general-purpose readout system for pixel ASICs," *Journal of Instrumentation*, vol. 12, no. 02, pp. C02 040–C02 040, Feb. 2017. [Online]. Available: https://doi.org/10.1088%2F1748-0221%2F12%2F02%2Fc02040

[60] J. Jakubek, "Precise energy calibration of pixel detector working in time-over-threshold mode," *Nuclear Instruments and Methods in Physics Research Section A: Accelerators, Spectrometers, Detectors and Associated Equipment*, vol. 633, pp. S262–S266, May 2011. [Online]. Available: https://doi.org/10.1016/j.nima.2010.06.183

[61] M. Ester, H.-P. Kriegel, J. Sander, and X. Xu, "A density-based algorithm for discovering clusters in large spatial databases with noise," in *KDD*. AAAI Press, 1996, pp. 226–231.

[62] G. Cowan, *Statistical Data Analysis*, 1st ed. Oxford : New York: Clarendon Press, Jun. 1998.

[63] R. J. Barlow, *Statistics: A Guide to the Use of Statistical Methods in the Physical Sciences*. John Wiley & Sons, Dec. 1993.

[64] G. Bohm and G. Zech, "Introduction to Statistics and Data Analysis for Physicists," Verlag Deutsches Elektronen-Synchrotron, Tech. Rep. PUBDB-2017-08987, 2017. [Online]. Available: https://dx.doi.org/10.3204/PUBDB-2017-08987

[65] S. Agostinelli, J. Allison, K. Amako, J. Apostolakis, H. Araujo, P. Arce, M. Asai, D. Axen, S. Banerjee, G. Barrand, F. Behner, L. Bellagamba, J. Boudreau, L. Broglia, A. Brunengo, H. Burkhardt, S. Chauvie, J. Chuma, R. Chytracek, G. Cooperman, G. Cosmo, P. Degtyarenko, A. Dell'Acqua, G. Depaola, D. Dietrich, R. Enami, A. Feliciello, C. Ferguson, H. Fesefeldt, G. Folger, F. Foppiano, A. Forti, S. Garelli, S. Giani, R. Giannitrapani, D. Gibin, J. J. Gómez Cadenas, I. González, G. Gracia Abril, G. Greeniaus, W. Greiner, V. Grichine, A. Grossheim, S. Guatelli, P. Gumplinger, R. Hamatsu, K. Hashimoto, H. Hasui, A. Heikkinen, A. Howard, V. Ivanchenko, A. Johnson, F. W. Jones, J. Kallenbach, N. Kanaya, M. Kawabata, Y. Kawabata, M. Kawaguti, S. Kelner, P. Kent, A. Kimura, T. Kodama, R. Kokoulin, M. Kossov, H. Kurashige, E. Lamanna, T. Lampén, V. Lara, V. Lefebure, F. Lei, M. Liendl, W. Lockman, F. Longo, S. Magni, M. Maire, E. Medernach, K. Minamimoto, P. Mora de Freitas, Y. Morita, K. Murakami, M. Nagamatu, R. Nartallo, P. Nieminen, T. Nishimura, K. Ohtsubo, M. Okamura, S. O'Neale, Y. Oohata, K. Paech, J. Perl, A. Pfeiffer, M. G. Pia, F. Ranjard, A. Rybin, S. Sadilov, E. Di Salvo, G. Santin, T. Sasaki, N. Savvas, Y. Sawada, S. Scherer, S. Sei, V. Sirotenko, D. Smith, N. Starkov, H. Stoecker, J. Sulkimo, M. Takahata, S. Tanaka, E. Tcherniaev, E. Safai Tehrani, M. Tropeano, P. Truscott, H. Uno, L. Urban, P. Urban, M. Verderi, A. Walkden, W. Wander, H. Weber, J. P. Wellisch, T. Wenaus, D. C. Williams, D. Wright, T. Yamada, H. Yoshida, and D. Zschiesche, "Geant4—a simulation toolkit," *Nuclear Instruments and Methods in Physics Research Section A: Accelerators, Spectrometers, Detectors and Associated Equipment*, vol. 506, no. 3, pp. 250–303, Jul. 2003. [Online]. Available: https://doi.org/10.1016/S0168-9002(03)01368-8

[66] B. De Vries, U. Wahl, S. Ruffenach, O. Briot, and A. Vantomme, "Influence of crystal mosaicity on axial channeling effects and lattice site determination of impurities," *Applied Physics Letters*, vol. 103, no. 17, p. 172108, Oct. 2013. [Online]. Available: https://doi.org/10.1063/1.4826705

[67] B. De Vries, "Lattice site location of impurities in group III nitrides using emission channeling." Ph.D. dissertation, Katholieke Universiteit Leuven, 2006. [Online]. Available: https://lirias.kuleuven.be/bitstream/1979/202/2/Thesis-BartDeVries-A4.pdf

[68] J. Idarraga, "MAFalda framework," Oct. 2018. [Online]. Available: https://github.com/idarraga/mafalda

[69] I. Antcheva, M. Ballintijn, B. Bellenot, M. Biskup, R. Brun, N. Buncic, P. Canal, D. Casadei, O. Couet, V. Fine, L. Franco, G. Ganis, A. Gheata, D. G. Maline, M. Goto, J. Iwaszkiewicz, A. Kreshuk, D. M. Segura, R. Maunder, L. Moneta, A. Naumann, E. Offermann, V. Onuchin, S. Panacek, F. Rademakers, P. Russo, and M. Tadel, "ROOT — A C++ framework for petabyte data storage, statistical analysis and visualization," *Computer Physics Communications*, vol. 180, no. 12, pp. 2499–2512, Dec. 2009. [Online]. Available: https://doi.org/10.1016/j.cpc.2009.08.005

[70] E. David-Bosne, U. Wahl, J. G. Correia, T. A. L. Lima, A. Vantomme, and L. M. C. Pereira, "A generalized fitting tool for analysis of two-dimensional channeling patterns," *Nuclear Instruments and Methods in Physics Research Section B: Beam Interactions with Materials and Atoms*, vol. 462, pp. 102–113, Jan. 2020. [Online]. Available: https://doi.org/10.1016/j.nimb.2019.10.029

[71] E. David-Bosne, “PyFDD: v0.7.0,” Jun. 2019. [Online]. Available: https://doi.org/10.5281/zenodo.3247499

[72] R. H. Byrd, P. Lu, J. Nocedal, and C. Zhu, “A Limited Memory Algorithm for Bound Constrained Optimization,” *SIAM Journal on Scientific Computing*, vol. 16, no. 5, pp. 1190–1208, Sep. 1995. [Online]. Available: https://doi.org/10.1137/0916069

[73] P. Virtanen, R. Gommers, T. E. Oliphant, M. Haberland, T. Reddy, D. Cournapeau, E. Burovski, P. Peterson, W. Weckesser, J. Bright, S. J. van der Walt, M. Brett, J. Wilson, K. J. Millman, N. Mayorov, A. R. J. Nelson, E. Jones, R. Kern, E. Larson, C. J. Carey, I. Polat, Y. Feng, E. W. Moore, J. VanderPlas, D. Laxalde, J. Perktold, R. Cimrman, I. Henriksen, E. A. Quintero, C. R. Harris, A. M. Archibald, A. H. Ribeiro, F. Pedregosa, P. van Mulbregt, and SciPy 1 0 Contributors, “SciPy 1.0–Fundamental Algorithms for Scientific Computing in Python,” *arXiv:1907.10121 [physics]*, Jul. 2019, arXiv: 1907.10121. [Online]. Available: http://arxiv.org/abs/1907.10121

[74] F. James and M. Roos, “Minuit – a system for function minimization and analysis of the parameter errors and correlations,” *Computer Physics Communications*, vol. 10, pp. 343–367, Dec. 1975. [Online]. Available: https://doi.org/10.1016/0010-4655(75)90039-9

[75] iminuit team, “iminuit - A Python interface to Minuit,” Feb. 2020. [Online]. Available: https://github.com/scikit-hep/iminuit

[76] W. McKinney, “Data Structures for Statistical Computing in Python,” in *Proceedings of the 9th Python in Science Conference*, S. v. d. Walt and J. Millman, Eds., 2010, pp. 51 – 56.

[77] U. Wahl, E. David-Bosne, L. M. Amorim, A. R. G. Costa, B. D. Vries, J. G. Correia, M. R. d. Silva, L. M. C. Pereira, and A. Vantomme, “Lattice sites of implanted Na in GaN and AlN in comparison to other light alkalis and alkaline earths,” *Journal of Applied Physics*, vol. 128, no. 4, p. 045703, Jan. 2020. [Online]. Available: https://doi.org/10.1063/5.0009653

[78] X. Xiong and S. C. Moss, “X-ray studies of defects and thermal vibrations in an organometallic vapor phase epitaxy grown GaN thin film,” *Journal of Applied Physics*, vol. 82, no. 5, pp. 2308–2311, Sep. 1997. [Online]. Available: https://doi.org/10.1063/1.366038

[79] B. De Vries, A. Vantomme, U. Wahl, J. G. Correia, J. P. Araújo, W. Lojkowski, and D. Kolesnikov, “Lattice site location and annealing behavior of implanted Ca and Sr in GaN,” *Journal of Applied Physics*, vol. 100, no. 2, p. 023531, Jul. 2006. [Online]. Available: https://doi.org/10.1063/1.2215091

[80] J. Neugebauer and C. G. Van de Walle, “Chemical trends for acceptor impurities in GaN,” *Journal of Applied Physics*, vol. 85, no. 5, pp. 3003–3005, Feb. 1999. [Online]. Available: https://doi.org/10.1063/1.369619

[81] C. Ronning, M. Dalmer, M. Uhrmacher, M. Restle, U. Vetter, L. Ziegeler, H. Hofsäss, T. Gehrke, K. Järrendahl, and R. F. Davis, “Ion implanted dopants in GaN and AlN: Lattice sites, annealing behavior, and defect recovery,” *Journal of Applied Physics*, vol. 87, no. 5, pp. 2149–2157, Feb. 2000. [Online]. Available: https://doi.org/10.1063/1.372154